NASA Reference Publication 1366

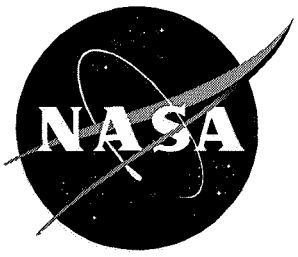

Cloud Properties Derived From GOES-7 for Spring 1994 ARM Intensive Observing Period Using Version 1.0.0 of ARM Satellite Data Analysis Program

Patrick Minnis, William L. Smith, Jr., Donald P. Garber, J. Kirk Ayers, and David R. Doelling

August 1995

NASA Reference Publication 1366

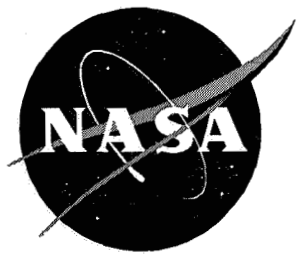

Cloud Properties Derived From GOES-7 for Spring 1994 ARM Intensive Observing Period Using Version 1.0.0 of ARM Satellite Data Analysis Program

Patrick Minnis
Langley Research Center • Hampton, Virginia

William L. Smith, Jr., Donald P. Garber, J. Kirk Ayers, and David R. Doelling
Lockheed Engineering & Sciences Company • Hampton, Virginia

National Aeronautics and Space Administration
Langley Research Center • Hampton, Virginia 23681-0001

August 1995

Acknowledgments

The data from Whiteman, Vance, and Tinker Air Force Bases were supplied by Captain Carolyn Vadnais, United States Air Force, and compiled by Theresa Hedgepeth of the Science Applications International Corporation. Patrick Heck and David F. Young of Lockheed Engineering & Sciences Company, Hampton, VA, provided assistance in the development of the analysis software and data verification. This research is supported by the Department of Energy Interagency Transfer Agreement ITF#214216AQ1 through Pacific Northwest Labs and monitored by Peter Minnett of Brookhaven National Laboratory.

Available electronically at the following URL address: http://techreports.larc.nasa.gov/ltrs/ltrs.html

Printed copies available from the following:

NASA Center for AeroSpace Information
800 Elkridge Landing Road
Linthicum Heights, MD 21090-2934
(301) 621-0390

National Technical Information Service (NTIS)
5285 Port Royal Road
Springfield, VA 22161-2171
(703) 487-4650

Summary

This document describes the initial formulation (Version 1.0.0) of the Atmospheric Radiation Measurement (ARM) Program satellite data analysis procedures. Techniques are presented for calibrating geostationary satellite data with Sun synchronous satellite radiances and for converting narrowband radiances to top-of-the-atmosphere fluxes and albedos. A methodology is documented for combining geostationary visible and infrared radiances with surface-based temperature observations to derive cloud amount, optical depth, height, thickness, temperature, and albedo. The analysis is limited to two grids centered over the ARM Southern Great Plains Central Facility in northcentral Oklahoma. Daytime data taken April 5 to May 1, 1994 were analyzed on the 0.3° and 0.5° latitude-longitude grids that cover areas of $0.9° \times 0.9°$ and $10° \times 14°$, respectively. A variety of cloud conditions ranging from scattered low cumulus to thin cirrus and thick cumulonimbus occurred during the study period. Detailed comparisons with hourly surface observations indicate that the mean cloudiness is within a few percent of the surface-derived sky cover. Formats of the results are also provided. The data can be accessed on the Internet via the World Wide Web at the following uniform resource locator:

`http://albedo.larc.nasa.gov:1123/arm.html`

Introduction

The Atmospheric Radiation Measurement (ARM) Program is a long-term measurement and modeling project designed to improve the understanding of atmospheric radiation and its interaction with the atmosphere and surface (Stokes and Schwartz 1994). The program concentrates on determining the influence of clouds and their radiative feedback effects on climate. The primary objectives are (1) to relate observed radiative fluxes in the atmosphere to the atmospheric temperature, composition (particularly water vapor and clouds), and surface radiative properties and (2) to develop and test parameterizations of atmospheric water (clouds and vapor) and the surface characteristics affecting atmospheric radiation. The parameterizations are intended for use in prognostic mesoscale and general circulation models (GCM). The models and measurements produced by ARM will be extremely valuable resources for advancing our understanding of the role of clouds in climate change.

The ARM observational program focuses on continuous long-term measurements taken from a variety of sensors at several locales representing various climatic regimes. More specifically, a complete suite of surface instruments is situated at a central facility in a given locale. Other sites surround the central facility at distances sufficient to monitor portions of an area equivalent to a GCM grid box. These extended facilities operate with a reduced complement of sensors. The locale and the regions around it are also monitored by Sun synchronous and geostationary meteorological satellites. The operational surface and satellite measurement system is occasionally enhanced by aircraft and additional surface-based instrumentation during special intensive observing periods (IOP). The first ARM site located in northcentral Oklahoma, called the Southern Great Plains (SGP) locale, will be followed by other sites in areas such as the tropical western Pacific and Alaska. The long-term ARM measurement systems are evolving at each locale as new instruments are deployed and the latest analysis techniques are implemented. The ARM surface-based sensors and the products derived from these techniques have been described in several reports (e.g., Schneider, Lamb, and Sisterson 1993).

The ARM satellite measurements complement the surface and atmosphere observations. Measurements of radiative fluxes at the top of the atmosphere and the surface can be used to determine the energy budget of the atmosphere. Many ARM surface instruments provide continuous, high-resolution measurements of various properties over a small area within the extended locale. The satellite can yield contiguous, low-resolution data over the entire locale and its surroundings. Ideally, the satellite data can be used to extend the information gained by the surface instruments by relating the surface-observed quantities to those deduced from the satellite radiances. The resulting relationships can be applied at other locations observed only by the satellite to infer quantities that are normally measured from surface instruments. To be useful for such applications, the radiances measured by the satellites must be analyzed to derive values for parameters that are relevant to cloud and radiation processes.

This report documents the initial analysis procedures that will be applied to the ARM satellite datasets; these procedures are collectively designated Version 1.0.0. Examples of the initial products are also included with preliminary validation. The ARM satellite data analysis program will ultimately be applied on an operational basis to geostationary and Sun synchronous datasets at all hours of the day. To reach this objective, the coverage and complexity of the analysis algorithms will be incrementally increased. Daytime analyses of geostationary satellite data for limited periods will be followed by continuous daytime analysis. The first digit in the Version 1.0.0 designator refers to the use of a visible-infrared bispectral method applied only during daytime. This first digit will denote changes such as the inclusion of new channels or nighttime data. The second digit in the designator will denote changes in the bispectral algorithm, and

the final digit will indicate changes in the calibrations applied to the satellite data. Additional procedures for analyzing daylight Sun synchronous data will be implemented in the future to include cloud effective particle size. Nighttime datasets will be analyzed on a periodic basis until a complete package of both daytime and nighttime procedures is obtained. The first step in this process is described here together with a summary of the results derived specifically for the Spring 1994 ARM IOP conducted over the SGP locale.

Nomenclature

ARM	Atmospheric Radiation Measurement Program
AU	astronomical unit
AVHRR	Advanced Very High Resolution Radiometer
a, b, c	regression coefficients
B	Planck function
C	satellite-derived cloud fraction
C_{sfc}	surface-observed cloud cover
CLD, CLR	cloudy and clear, respectively
CS	cirrostratus model cloud
D	digital brightness counts, 0 to 255
d_{sl}	days since launch
ERBE	Earth Radiation Budget Experiment
ERBS	Earth Radiation Budget Satellite
f_D	forward scattering truncation factor
GCM	general circulation model
GOES	Geostationary Operational Environmental Satellite
g	visible sensor gain
h	local time, hr
HBTM	hybrid bispectral threshold method
IOP	intensive observing period
IR	infrared, 10.5 to 12.5 μm
ISCCP	International Satellite Cloud Climatology Project
L	radiance, W/m^2-sr
LBTM	layer bispectral threshold method
LT	local time
LW	longwave, 5.0 to 50.0 μm
M_{ir}, M_{lw}	infrared and longwave fluxes, W-m^{-2}
McIDAS	Man-computer Interactive Data Analysis System
p	pressure, hPa
P_m, P_h, P_p	temperature-reflectance pairs corresponding to clouds at 2 km, 6 km, and tropopause, respectively
R	linear correlation coefficient
RH	relative humidity, percent
SCF	SGP Central Facility
SE	standard error of estimate, percent
SGP	Southern Great Plains
SW	shortwave, 0.2 to 5.0 μm
t_{a1}	transmittance of ozone above cloud
$t_c\downarrow, t_c\uparrow$	downward and upward cloud transmittance, respectively
T	equivalent blackbody temperature
T_a, T_c, T_t	air, cloud-center, and cloud-top temperature, respectively, K
T_{cs}, T_s	clear-sky and surface shelter temperature, respectively, K
$T_{lim}, T_{lim1}, T_{lim2}$	clear-sky temperature limits, K
T_m, T_h, T_p	temperature at 2 km, 6 km, and tropopause, respectively, K
TAFB	Tinker Air Force Base
TOA	top of atmosphere
UTC	Universal Coordinated Time, hr × 100
VAFB	Vance Air Force Base
VIS	visible, 0.55 to 0.75 μm
VISSR	Visible Infrared Spin Scan Radiometer
WAFB	Whiteman Air Force Base
z	altitude, km
z_c, z_s, z_t	cloud-center, surface, and cloud-top altitude, respectively, km
α	albedo
α_c, α_{cd}	cloud and diffuse cloud albedo, respectively
α_{cs}, α_{sd}	clear-sky and diffuse clear albedo, respectively
α_{R1}	albedo of Rayleigh layer above cloud
α_{sw}, α_v	shortwave and visible albedo, respectively
α_{swce}	effective shortwave cloud albedo
γ_{ir}	IR limb-darkening function
δ	Earth-Sun distance correction factor
ΔD	clear-sky count tolerance

ΔT_{scs}	greatest expected difference between T_{cs} and T_s, K
Δz	cloud thickness, km
ε, ε_t	cloud-center and cloud-top effective emissivities, respectively
ζ	reflectance parameterization normalization factor
θ	viewing zenith angle
θ_o	solar zenith angle
μ	cosine viewing zenith angle
μ_o	cosine solar zenith angle
ρ	reflectance
ρ_{c1}	combined reflectance of cloud and overlying Rayleigh layer
ρ_{R2}	direct reflectance of Rayleigh layer below cloud
σ	standard deviation
τ	cloud visible optical depth
τ_{O_3}, τ_{R1}	ozone and Rayleigh optical depth above cloud, respectively
χ	anisotropic reflectance correction factor
ϕ	relative azimuth angle

Subscripts:

A	AVHRR
c	clouds
cs	clear sky
G	GOES
ir	infrared

Data

The ARM Spring 1994 IOP operated for 21 days during April at the SGP Central Facility (SCF). Satellite data are analyzed for a 27-day period from April 5 to May 1, 1994. Other satellite data taken during April 1985 are used to develop relationships for computing broadband fluxes from narrowband radiances for the IOP dataset. Two grids are used for the ARM analyses. A 0.5° latitude-longitude grid, designated the mesoscale grid, extending from 32°N to 42°N and from 91°W to 105°W was selected to center the domain on the SGP, to include several GCM-scale grid boxes, and to minimize the difficulties involved in analyzing data over mountain snow fields. A much smaller fine-scale domain, extending from 36.16°N to 37.06°N and from 97.04°W to 97.94°W is divided into nine 0.3° grid boxes. This small-scale domain is centered on the SCF at 36.61°N, 97.49°W (fig. 1). The fine-scale grid is designed for direct intercomparison between satellite and surface observations. The 0.3° grid box is the minimum size needed for accurate cloud property retrievals. The mean surface elevation z_s was computed in kilometers above mean sea level for each grid box with the surface elevations given in the 10′ resolution U.S. Navy Surface Elevation Map (available from the National Center for Atmospheric Research in Boulder, Colorado). The average elevations (fig. 1) range from a few hundred meters in the southeast to nearly 2.4 km on the western edge of the domain. The SCF is located at an elevation of ≈0.3 km.

GOES-6

Regional two-dimensional histograms were formed from April 1985, hourly 8-km visible (VIS) 8-bit digital brightness counts D_6 and infrared (IR) equivalent blackbody temperatures. The digital brightness counts and blackbody temperatures were measured by the GOES-6 (Geostationary Operational Environmental Satellite) located over the equator at ≈108°W. Each region corresponds to one of the 2.5° latitude-longitude grid boxes between 32.5°N and 42.5°N and from 95°W to 105°W. Minnis, Harrison, and Young (1991) computed hourly cloud amount for each region from the individual radiances with the hybrid bispectral threshold method (HBTM). (See Minnis, Harrison, and Gibson 1987). The mean equivalent blackbody temperature T was computed from the IR radiances for each region and hour only for April 1 to 20 to eliminate a period of large calibration uncertainty that occurred during the last third of the month (Minnis, Harrison, and Young 1991). The narrowband reflectance ρ_6 was computed with the calibration coefficients reported by Whitlock, LeCroy, and Wheeler (1994). Visible data were used for the entire month.

For April 1985, the GOES-6 narrowband reflectance is as follows:

$$\rho_6 = (0.0085 D_6^2 - 8.0) / 526.2 \mu_o \delta \qquad (1)$$

where $\mu_o = \cos\theta_o$, θ_o is the solar zenith angle, and δ is the Earth-Sun distance correction factor. The narrowband albedo is

$$\alpha_6 = (1 - C)\chi_{cs}(\theta_o, \theta, \phi)\rho_{cs} + C\chi_c(\theta_o, \theta, \phi)\rho_6 \qquad (2)$$

where C is the total cloud amount, χ_{cs} and χ_c are the anisotropic reflectance correction factors for clear sky and clouds, respectively, from Minnis and Harrison (1984b). The mean clear-sky and cloud reflectances for the given scene are ρ_{cs} and ρ_c, respectively. The respective viewing zenith and relative azimuth angles are θ and ϕ.

GOES-7

During April 1994, GOES-7 was located in nearly the same position as GOES-6 had been during April 1985. The 4-km VIS and IR data were combined into regional two-dimensional histograms for the 0.3° and 0.5° grids described previously. The histograms were developed from data taken every half hour between 1330 and 2330 UTC. The GOES-7 VIS counts D_7 were converted to reflectance by using the following equation:

$$\rho_7 = (0.0126D_7^2 - 4.0)/526.2\mu_o\delta \qquad (3)$$

The calibration coefficients are based on an intercalibration between GOES-7 VIS and the NOAA-11 Advanced Very High Resolution Radiometer (AVHRR) channel 1. The procedure, described in appendix A, assumes that the AVHRR is calibrated. The equivalent blackbody temperatures were determined with the standard GOES calibration.

ERBS

The Earth Radiation Budget Satellite (ERBS) measured broadband regional shortwave (SW) and longwave (LW) radiances with a cross-track scanner having a nominal $\approx 31 \times 47$ km^2 field of view at nadir (Barkstrom and Smith 1986) as part of the Earth Radiation Budget Experiment (ERBE). The ERBS is in a 56° inclined orbit, which allows its equator-crossing time to precess all hours of the day in 36 days. The radiances were converted to SW and LW fluxes with the methods of Smith et al. (1986) and Wielicki and Green (1989) and the anisotropic models of Suttles et al. (1988, 1989) for clear, partly cloudy, mostly cloudy, and overcast pixels. Longwave fluxes within a given 2.5° latitude-longitude region, averaged to obtain the mean longwave flux M_{lw} for each ERBS overpass, are assumed to correspond to the local half hour at the center of the region. The SW albedo α_{sw} was computed from the SW flux and adjusted to the local half hour with the techniques of Brooks et al. (1986). The regional broadband quantities taken during April 1985 over the GOES-6 grid are used here.

Atmospheric Profiles and Surface Data

Vertical profiles of air temperature $T_a(p)$ and humidity from the National Meteorological Center gridded analyses at standard pressure p levels (surface; 925, 850, 700, 500, 400, 300, 250, 200, 150, and 100 hPa; and tropopause) were used to analyze the April 1985 dataset. National Weather Service 12-hourly temperature and humidity soundings taken at standard levels during April 1994 were interpolated to the mesoscale grid with a fast Barnes interpolation method (Hibbard and Wylie, 1985), as implemented by the University of Wisconsin Man-computer Interactive Data Analysis System (McIDAS). The interpolation technique uses all available soundings within the domain and the closest soundings outside the domain to eliminate edge effects. Hourly surface air temperatures T_s from all reporting stations within the domain are interpolated to provide a default surface temperature for each grid box.

Methodology

The remote sensing of cloud properties involves the use of an idealized conceptual model of clouds to interpret the radiances emanating from real scenes. The conceptual model relies on the following assumptions. All clouds are plane-parallel entities that only occur within the boundaries of a satellite field of view or pixel. The clouds completely fill the pixels in which they occur and have a uniform distribution of particle sizes within the pixel. Each cloudy pixel contains a cloud at only one altitude and has a thickness prescribed by empirical formulae. The satellite sensor is correctly calibrated and the anisotropy of the clear-sky conditions is completely described with the assigned bidirectional reflectance model. The anisotropy of the cloud is completely described by the cloud bidirectional reflectance models used by ERBE for the SW data and by Minnis and Harrison (1984b) for the VIS data. The limb darkening of the IR radiances and LW fluxes follows the models developed by Minnis and Harrison (1984b) and the ERBE models, respectively. The details of the applied methodology are given in this section. Some shortcomings due to these assumptions are mentioned in the "Discussion" section.

Cloud Properties

The methodology used here is designated the layer bispectral threshold method (LBTM). Cloud fraction C_i, cloud-center temperature T_{ci}, cloud-top temperature T_{ti}, cloud optical depth τ_i, cloud-top altitude z_{ti}, and cloud-center altitude z_{ci} were computed for the following three height intervals: low ($z_c \le 2$ km), middle ($2 < z_c \le 6$ km), and high ($z_c > 6$ km). These computations were performed with the procedures described by Minnis, Heck, and Young (1993). The subscript $i = 1, 2, 3$ refers to the low, middle, and high layers, respectively. The total cloud amount C is the simple sum of the three layer amounts with no overlap, and the total cloud optical depth τ, temperatures T_t and T_c, and altitudes z_t and z_c are weighted averages with C_i serving as the weights. The brightness temperature averages are performed with the equivalent radiance evaluated at 11.5 μm. The cloud-center temperature is defined as the equivalent radiating temperature of the cloud. For optically thin clouds, the cloud-center temperature generally corresponds to some temperature between the physical center and top of the

cloud. The cloud-center altitude $z(T_c)$ is determined from a sounding. The cloud-center temperature approaches the cloud-top temperature as the cloud becomes optically thick. Thus, for optically thick clouds, $T_c = T_t$ and $z_c = z_t$. A summary of the cloud analysis technique is given as follows.

Clear-sky reflectance ρ_{cs} is determined at each hour for a given region with a minimum reflectance method (Minnis and Harrison, 1984a). These reflectances are assumed to be valid throughout the month; however, they may be adjusted for specific cases as in Minnis, Harrison, and Gibson (1987). During daylight hours, clear-sky temperature T_{cs} corresponds to the mean IR radiance for all pixels having VIS counts $D < D_{cs} + \Delta D$ and temperatures $T > T_{lim}$, where D_{cs} corresponds to ρ_{cs} and $\Delta D = 10.4 + 1.4 \ln(\mu_o)$. The term T_{lim} is the climatological minimum limit imposed on the clear-sky temperature (e.g., Minnis, Harrison, and Gibson 1987) to ensure that T_{cs} is not unrealistically low. The clear-sky temperature is tested and altered as follows. The parameter T_{lim} is set equal to the smaller of the two values $T_s - 5$ K or T_{lim1} where $T_{lim1} = T_s - \Delta T_{scs}$ and ΔT_{scs} is the mean hourly regional difference $T_{cs} - T_s$ minus two standard deviations of that difference for a given local hour. Figure 2 gives the mean values of T_{cs} and T_s for all scenes in the mesoscale domain having $C < 0.05$. The domain mean clear-sky temperature peaks near 1300 LT, while T_s has a broad maximum approximately 2 hours later. Figure 3 shows the differences between the mean values of T_{cs} and T_s minus two standard deviations of the difference $(T_{cs} - T_s)$ at a particular local time. The regression fit to the data shown in figure 3 is

$$\Delta T_{scs} = -19.5 + 3.2h - 0.144h^2 \qquad (4)$$

where h is the local time (LT) in hours and is referenced to 98°W. A second limit $T_{lim2} = T_s - 10$ K is also used to constrain T_{cs}. When a value of T_{cs} is derived from the data, it is reset to equal T_{lim} if $T_{cs} < T_{lim1}$. If no value of T_{cs} can be determined (i.e., overcast conditions) and no temperatures are greater than T_{lim2} or no VIS counts are lower than $D_{cs} + \Delta D$, then T_s is substituted for T_{cs}. If no value for T_{cs} can be determined, but VIS counts are less than $D_{cs} + \Delta D$ and observed temperatures are greater than T_{lim2}, then $T_{cs} = T_{lim1}$.

The cloudy pixels are identified with a simple threshold approach that is based on the division of the VIS-IR histogram into clear and cloudy layers. (See fig. 4.) A pixel is cloudy when $T < T_{cs} - 5$ K or $D > D_{cs} + \Delta D$. Cloudy pixels are grouped into low, middle, and high categories with model calculations of temperature and reflectance variations for clouds at 2 and 6 km. The calculations determine the $\rho - T$ pairs that constitute the boundaries of each layer. These boundaries are denoted by the curves labeled P_m, P_h, and P_p, which are shown in figure 4. The low-middle boundary P_m is determined with a cloud composed of water droplets having an effective radius of 10 μm at the temperature T_m. The middle-high boundary P_h is computed with a theoretical cirrostratus (CS) cloud at the temperature T_h. The CS cloud comprises randomly oriented hexagonal ice columns having a range of sizes (Takano and Liou 1989). To constrain the interpretations, an upper boundary P_p that corresponds to a CS cloud at the tropopause temperature T_p is also computed. Pixels that are cold and darker than the P_p boundary are defined as dark pixels.

The model used to determine the boundaries and to interpret the reflectances for cloud optical depth is

$$\rho = \sum \rho_i / (1 - \zeta) \qquad i = 1, 5 \qquad (5)$$

where ζ is a regression normalization factor, and ρ_i are parameterizations of the multiple scattering and absorption by the atmosphere, scattering by the cloud, and reflection by the surface (Minnis, Liou, and Takano 1993). The reflectance parameterization is described briefly as follows.

The visible-channel reflectance contributed by the cloud and the atmosphere above it is

$$\rho_1 = t_{a1}\rho_{c1} = t_{a1}\rho_{c1}(\tau, \tau_{R1}) \qquad (6a)$$

where ρ_{c1} is the combined reflectance of the cloud and the Rayleigh scattering layer above it. The transmittance,

$$t_{a1} = \exp[-\tau_{O_3}(1/\mu_o + 1/\mu)]$$

where $\mu = \cos\theta$, the Rayleigh optical depth above the cloud is τ_{R1}, and the ozone absorption optical depth for the VIS channel is τ_{O_3}. For this analysis, τ_{O_3} is fixed at 0.022, a value that corresponds to an ozone path length of 0.32 cm-STP. The beam reflectance by the surface is

$$\rho_2 = t_c \downarrow t_c \uparrow \rho_s \qquad (6b)$$

where the downward and upward cloud transmittances are

$$t_c \downarrow = \exp[-(1 - f_D)\tau/\mu_o]$$

and

$$t_c \uparrow = \exp[-(1 - f_D)\tau/\mu]$$

and f_D is the fraction of the beam scattered in the forward direction because of diffraction and direct transmission through the droplet or crystal. The value of f_D is generally greater than or equal to 0.5 at visible wavelengths. The fraction of radiation scattered from the forward direction, reflected by the surface, and transmitted

diffusely back through the cloud to space is approximated as

$$\rho_3 = \alpha_{sd}(1-\alpha_{cd})(1-t_c\uparrow-\alpha_c) \qquad (6c)$$

where $\alpha_c(\tau, \mu_o)$ is the cloud albedo and α_{cd} is the diffuse cloud albedo. The fourth term

$$\rho_4 = \left[\rho_{R2}\left(1-\alpha_c^{0.5}\right)-\alpha_{R1}\alpha_c^2\right](1-\alpha_{cd}) \qquad (6d)$$

accounts for the relative thickness of the Rayleigh layers above and below the cloud. The effects of the two Rayleigh layers are included by using the direct Rayleigh reflectance term for the bottom layer ρ_{R2} and the Rayleigh albedo for the top layer α_{R1}. The fifth term

$$\rho_5 = a_0 + a_1\left(\frac{\tau}{1+\tau^2}\right)^2\mu_o^2\alpha_{cs} + a_2\alpha_{sd} \qquad (6e)$$

accounts for an overestimate in the surface contribution to the reflectance by ρ_2 for small cloud optical depths. The coefficients a_i depend on the microphysical model, α_{cs} is the clear-sky albedo, and α_{sd} is the diffuse clear-sky albedo. The denominator in equation (5) uses the following parameter:

$$\zeta = b_0 + b_1\ln(\tau) + b_2\alpha_{sd}\ln(\tau) + b_3\alpha_{sd} \qquad (7)$$

to minimize biases in the parameterization. The coefficients b_i also vary with the microphysical model.

Cloud radiating temperature is assumed to be

$$B(T) = (1-\varepsilon)B(T_{cs}) + \varepsilon B(T_c) \qquad (8)$$

where B is the Planck function evaluated at 11.5 μm. The effective emissivity is

$$\varepsilon = 1-\exp\left[a(\tau/\mu)^b\right] \qquad (9)$$

The coefficients a and b depend on the cloud microphysics (see Minnis, Liou, and Takano 1993).

The optical depth for the cloudy pixels is obtained by matching the observed reflectance to the reflectance parameterization through an iterative process. Optical depth cannot be computed for pixels as dark or darker than the clear scene, so they are averaged with brighter pixels until an optical depth can be computed. Cloud temperatures are computed using equations (8) and (9) with the observed IR temperature T_{cs} and the derived value of τ. If the value of $T_c < T_p - 2$ K and $\tau/\mu < 5$, then T_c is reset to equal T_p and the emissivity and optical depth are recomputed. Further details of these parameterizations, the models used in them, and their application are found in Minnis, Heck, and Young (1993) and Minnis, Liou, and Takano (1993).

Cloud-top temperature is computed with the cloud-top emissivity parameter. For optically thick clouds ($\tau > 6$), the cloud radiating center and physical top are assumed to be the same. Thus, the cloud-top emissivity $\varepsilon_t = \varepsilon$. For optically thin clouds, ε_t depends on T_c. If $T_c < 245$ K, then

$$\varepsilon_t = (-0.00914T_c + 2.966)\,\varepsilon \qquad (10)$$

(See Minnis, Harrison, and Heck 1990). If $T_c > 280$ K, then $\varepsilon_t = 0.99\varepsilon$ is assumed. For 245 K $< T_c \le 280$ K, linear interpolation between the warm and cold cases, the following equation is used to determine the cloud-top emissivity:

$$\varepsilon_t = (0.00753T_c + 1.12)\,\varepsilon \qquad (11)$$

For clouds having moderate optical depths ($2 < \tau < 6$), simple linear interpolation between the thick and thin estimates is used. The cloud-top temperature is

$$T_t = B^{-1}\{[B(T) - (1-\varepsilon_t)B(T_{cs})]/\varepsilon_t\} \qquad (12)$$

where B^{-1} is the inverse Planck function. If $T_t < T_p$, then T_t is reset to equal T_p. Cloud-top altitude is taken from the sounding as $z_t = z(T_t)$.

Cloud thickness was computed for clouds having $T_c \le 245$ K as

$$\Delta z = 7.2 - 0.024T_c + 0.95\ln(\tau) \qquad (13)$$

(Smith et al. 1993) and for clouds with $T_c > 275$ K as

$$\Delta z = 0.085\tau^{1/2} \qquad (14)$$

(Minnis, Heck, et al. 1992). For cloud temperatures between 245 and 275 K, linear interpolation between equations (13) and (14) is used to compute Δz. Several criteria are used to ensure that the cloud thickness is reasonable. If $\Delta z < 0.1$ km, then Δz is reset to equal 0.1 km. If $z_t - \Delta z < z_s$, then the cloud thickness is reset to $\Delta z = z_t - z_s + 0.1$ km. If $z_t - \Delta z > z_c$, then the cloud-top temperature is reset in the following manner: $z_t = z_c + \Delta z - 0.1$ km. These steps are repeated if necessary.

Radiation Properties

The SW albedos and top-of-the-atmosphere (TOA) LW fluxes for the ARM IOP are computed from the VIS albedos and IR equivalent blackbody temperatures, respectively, by using relationships based on regression analyses applied to the April 1985 GOES-6 and ERBS datasets. The ERBS data are matched to GOES-6 data

taken at the nearest UTC hour. The SW albedo is determined as

$$\alpha_{sw} = \alpha_{sw}(\mathrm{CLR})\,(1-C) + \alpha_{sw}(\mathrm{CLD})\,C \qquad (15)$$

where the clear-sky SW albedo is

$$\alpha_{sw}(\mathrm{CLR}) = a_0 + a_1\alpha_v(\mathrm{CLR}) + a_2 \ln(1/\mu_o) \qquad (16)$$

and the cloudy sky albedo is

$$\alpha_{sw}(\mathrm{CLD}) = b_0 + b_1\alpha_v(\mathrm{CLD}) + b_2\alpha_v(\mathrm{CLD})^2 + b_3 \ln(1/\mu_o) \qquad (17)$$

where α_v (CLR) and α_v (CLD) are the clear and cloudy VIS albedos, respectively, and a_i and b_i are the regression coefficients. The VIS albedos are restricted to values between 0 and 1. If $\alpha_v > 1$, then its value is reset to 1 before applying equation (17). The regression formula is unable to compute SW albedo greater than unity. These formulations yield approximately the same accuracy as the ray-matching techniques of Minnis and Harrison (1984b) because of the increased number of samples (Doelling et al. 1990). They also permit the determination of regionally dependent coefficients.

Preliminary studies of the regression analyses revealed that the clear-sky SW albedo can be more accurately determined if the regressions are performed by using matched clear-sky data and all data separately. Clear-sky data for the 2.5° regions are defined as those having $C < 0.15$ from the HBTM and a clear-sky identification by the ERBE analysis. For the clear-sky case (eq. (16)), the quadratic term is not used because of the narrow range of data. Figure 5 shows the VIS-SW regression analyses for April 1985 with the clear-sky (fig. 5(a)) and all (fig. 5(b)) matched data with $\theta_o < 78°$. For figure 5(a), the multiple correlation coefficient $R^2 = 0.87$ and the standard error of the estimate (SE) is 5.8 percent for data with $\theta < 70°$. The fit to the total dataset yields $R^2 = 0.91$ and $SE = 11.7$ percent. The derived values for the clear-sky coefficients are $a_0 = 0.0893$, $a_1 = 0.5775$, and $a_2 = 0.0709$. For the total dataset, only ERBS data taken for $\theta < 45°$ were used to prevent the smearing effects of the larger ERBS fields of view at higher viewing angles.[1] The resulting coefficients are $b_0 = 0.0588$, $b_1 = 0.8623$, $b_2 = -0.1190$, and $b_3 = 0.0624$. Although the clear-sky curves are relatively flat, significant dependence on θ_o is indicated by the separation of the plotted curves in both figures 5(a) and 5(b). The relationship derived with only the ARM mesoscale region dataset (fig. 5(b)) is close to that determined with all land regions in the GOES field of view. Combining the two fits as in equation (15) yields an overall uncertainty of 10.9 percent.

The TOA LW flux is

$$M_{lw} = c_0 + c_1 M_{ir} + c_2 M_{ir}^2 + c_3 M_{ir} \ln(RH) \qquad (18)$$

where RH is the mean relative humidity for all layers above the altitude $z(T_a)$ corresponding to T, as reported by Minnis, Harrison, and Young (1991). The narrowband flux is

$$M_{ir} = 2L_{ir}(0°)\int_0^{2\pi}\int_0^{\pi/2}\gamma_{ir}\sin\theta\,\cos\theta\,d\theta d\phi = 6.18L_{ir}(0°) \qquad (19)$$

where the factor of 2 (in μm) is used to account for the bandwidth (10.2 to 12.2 μm) of the GOES sensor. The IR radiances

$$L_{ir} = B(T) \qquad (20)$$

are adjusted to the nadir view by

$$L_{ir}(0°) = \gamma_{ir}L_{ir}(\theta) \qquad (21)$$

where the limb-darkening function is

$$\gamma_{ir} = 1, \text{ if } \theta < 11°$$

else

$$\gamma_{ir} = 1.00067 + 0.03247 \ln(\mu) \qquad (22)$$

This formula approximates the IR limb-darkening function used by Minnis and Harrison (1984a). Calibration of the instrument accounts for the response function of the IR filter.[2] Thus, a flat sensor response is assumed when the equivalent blackbody temperatures are used. Equation (12) is an approximation of the narrowband flux developed to obtain the longwave flux from the calibrated narrowband radiances. It was not intended to serve as a standard for comparison with calculations of window flux. The radiance corresponding to the equivalent blackbody temperature at the band center is probably a better standard for comparison. According to a personal communication with Menzel, the equivalent blackbody temperature was determined by using the band center to invert the measured radiance within ±0.1K of the mean temperature based on the radiance integrated over the entire band.

[1]Paper entitled "Reconstruction of Earth's Radiation Field from Earth Radiation Budget Experiment (ERBE) Measurements" by Rajeeb Hazra, G. Louis Smith, and Stephen K. Park (pending publication).

[2]Reference work on Prelaunch Study of VAS-D Performance that was performed by P. Menzel under contract NAS5-21965.

Figure 6 shows the matched IR-LW data and the resultant regression curves for various relative humidities. These results are similar to those found for all land areas viewed by GOES during April 1985 (Minnis, Harrison, and Young 1991). The *SE* is 4 percent and R_2 is 0.91 for the 1320 samples used in the correlation. Values for the coefficients are $c_0 = 64.39$ W-m^{-2}, $c_1 = 6.57$, $c_2 = -0.0275$ m^2-W^{-1}, and $c_3 = -0.322$. These coefficients were used in equation (18) to compute the LW fluxes from the April 1994 ARM IOP GOES-7 data.

Results

The methodology described in the preceding section was applied to the April 1994 GOES-7 data. The results have been archived for public distribution. Appendix B describes the format of the archived dataset and the means to access the data via the World Wide Web.

Instantaneous Results

To demonstrate the resolution of the cloud products, an example of the 1930 UTC, April 14, 1994 VIS imagery in figure 7 is overlaid with the derived values of τ for a portion of the mesoscale grid. Its IR counterpart is shown in figure 8 overlaid with the cloud fraction in each region. These images contain fields of scattered thin cirrus that are faint in some regions and thicker cirrus in the northwest and southeast corners of the image. Optical depths range from 0.1 to 8.7 in figure 7. The larger optical depths are generally associated with the heaviest cloud cover (fig. 8). Figure 9 shows the entire mesoscale domain outlined in a VIS and IR image pair taken at 1800 UTC, April 25, 1994. The primary feature includes several lines of thunderstorms passing northward through west central Oklahoma into Kansas. This squall line is preceded on the eastern side by a large mass of densely packed, low-level cumulus clouds and followed by thin wispy cirrus clouds in northwestern Texas. The thin cirrus are evident in the IR image but barely discernible in the VIS photograph.

The cloud properties derived from the images in figure 9 are shown in figures 10 to 15. Total cloud amount (fig. 10) is nearly 100 percent over most of the domain. The clearer areas southwest and northeast of the thunderstorms are interspersed with thin midlevel and high clouds. The cirrus clouds in the Texas Panhandle were found primarily between 5 and 7 km. The lowest clouds are found in abundance over Arkansas and southwestern Missouri. These locations are consistent with the VIS imagery, which suggests that the cumulus clouds in those areas were dimmer and probably less developed vertically than the surrounding clouds. The surrounding clouds were placed in the midlevel category. Small fractions of low cloudiness are also observed along the periphery of the main high and midlevel cloud fields. Some small low-cloud amounts may result from pixels that are partially filled with midlevel or high clouds. Most midlevel cloud tops in the eastern region are located at ≈3 km.

Cloud optical depths (fig. 11) are generally very high over the domain, especially for the high clouds over Oklahoma and central Colorado. The mean cloud-center and cloud-top heights are shown in figure 12. The highest clouds are found over the thunderstorms. The differences between z_t and z_c are typically only 0.3 to 0.5 km. As expected, the thickest clouds (fig. 13) are found over Oklahoma and Colorado because of the cumulonimbus systems. Cloud thickness is estimated to be as great as 6.5 km in some storms. All low clouds appear to be less than 1-km thick. Some of the densest midlevel clouds found between the high clouds are up to 3.5-km thick. The VIS and SW clear-sky and total albedos are shown in figure 14. The clear-sky VIS albedo varies from 0.10 in central Arkansas to 0.18 in eastern New Mexico. Shortwave clear-sky albedos vary from less than 0.15 to over 0.20 in a pattern like that seen for the VIS albedo. The 1800-UTC clear-sky albedo near the central facility is ≈0.170. VIS total albedos are greater than the SW albedos except for the relatively clear regions. The total albedo variability is very similar to that for optical depth (fig. 11). Clear-sky IR and total temperatures are plotted with the corresponding LW fluxes in figure 15. The greatest values of T_{cs} and M_{lwcs} are found in the clearest regions of the domain. Coldest cloud-tops with $T_c < 220$ K are seen over the squalls in central Oklahoma. The LW fluxes vary from 120 to 305 W-m^{-2}.

Average Cloud Properties

The mean total and three-layer cloud amounts and optical depths averaged for a 2.5° region centered over the SCF are plotted in figures 16 and 17, respectively. In these figures, the results are shown for the 0.5° region including the SCF and the middle 0.3° box centered on the SCF. High cloudiness peaks during the late morning and late afternoon in the 2.5° box, while the midlevel clouds are relatively constant during the morning and diminish during the afternoon. Low clouds peak during the midafternoon and gradually diminish toward the evening. Total cloud cover has a broad maximum centered near 1330 LT. High clouds appear to have the greatest influence on the total cloud variability. In the 0.3° box, the total cloudiness has a stronger early afternoon maximum. The high clouds show a broad maximum from midmorning to late afternoon, while the midlevel clouds peak near 1300 LT. The low-cloud variation is similar to that of the larger region but much noisier. Except for the noise in the 0.3° data, the cloud amounts for the two regions are similar. This similarity

suggests that the surface measurements of clouds taken at the SCF may represent a GCM-scale gridbox for this area over the time scale of 1 month.

Total optical depth (fig. 17) appears to be dominated by the high clouds at both scales. It peaks near 1330 LT then decreases rapidly an hour later, which suggests that the deepest daytime convection ends shortly after local noon. After the midday maximum in τ, the high clouds comprise more thin cirrus blowoff than cumulonimbus tops. The midlevel clouds follow the mean total optical depths, and the low-level clouds are generally thinner than the higher clouds. An exception is the extremely high value at 1200 LT for the 0.3° region where the mean low-cloud optical depth reaches 34. This anomalous value resulted from a slight increase in the cloud-top temperature for a short time at midday during April 11 so that a few pixels were entered into the low-cloud category. A raining middle cloud layer with large optical depths covered the region at an altitude slightly higher than 2 km for most of the day. The hour-to-hour variability in the small region is absent in the 2.5° results.

Figure 18 shows the mean half-hourly IOP total cloud amounts, heights, and optical depths averaged for the 2.5° and 0.3° regions in figure 17. The same quantities are also shown for the 0.5° region that includes the SCF. The diurnal variations in the total parameters are similar in phase at all scales but differ in magnitude for the three regions. Hour-to-hour variability diminishes as the regional scale is decreased. The diurnal range in cloud height is ≈2 km in the smallest region; it drops to less than 1.5 km for the 0.5° region and less than 1.0 km for the 2.5° box. Similar decreases are evident in the mean total cloud optical depth and amounts.

Figure 19 shows the distribution of observed cloud-top heights for the 0.5° region including the SCF. Clouds were observed most frequently between 2 and 5 km and between 9 and 13 km over the SCF. Few clouds were observed between 7 and 9 km. The corresponding cloud thickness distributions in figure 20 show that most of the low clouds were relatively thin with the mode thickness near 0.15 km. Midlevel clouds had a mode thickness of ≈0.20 km but had a much greater range than the low clouds. The high-cloud mode thickness is 0.5 km, but the range in thickness is about double that for the midlevel clouds. These results are similar to those for the 0.3° region centered on the SCF.

The April IOP mean cloud properties for the SGP domain are shown in figures 21 to 24. Total cloud amount (fig. 21) varies from less than 40 percent in the southwestern corner to more than 70 percent in Louisiana, Colorado, and Nebraska. Low clouds appear to be a significant component only over western Oklahoma and the southeastern quadrant of the domain. Midlevel and high clouds dominate elsewhere, especially in the northern half of the grid. The cloud optical depth patterns (fig. 22) reveal the main centers of low-level convergence. Low, midlevel, and high cloud optical depths all reach maximum levels in southern Kansas and central Missouri. During this time period, convective storms such as those in figure 9 apparently form most often in the vicinity of the SCF and move northwestward through Kansas and Missouri. High clouds passing over the southwestern quadrant are primarily optically thin cirrus. Mean total cloud-center heights (fig. 23) range from ≈4 km along the southern and southeastern edges of the domain to almost 7 km over the Rocky Mountains. Other relative height maxima occur in a southwest-to-northeast line from the Texas Panhandle through the SCF and into Missouri.

The mean low-cloud tops vary from 1.5 to more than 2 km, while mean midlevel clouds are found between 3.5 and 4.5 km. Although low clouds are only supposed to be found at altitudes below 2 km, some resetting of the cloud heights occurs after the initial analysis is performed. For example, the surface elevation (fig. 1) in some regions exceeds 2 km. Cloud height is determined with interpolated soundings. Thus, some interpolated values result in low-cloud altitudes over some of the higher elevations. When the cloud base (top-thickness) for a given cloud layer falls below the surface elevation, both cloud base and top are adjusted to levels at least 0.1 km above the surface. Cloud height increases from southeast to northwest for low and midlevel clouds. Mean high-cloud heights, however, decrease from nearly 11 km in the south to 8.5 km in the northern part of the grid. Figure 24 shows the variation in cloud-amount-weighted mean cloud thickness. Because of the heavy reliance of Δz on optical depth, the patterns in figure 24 are similar to those in figure 22. The thickest clouds occur in southern Kansas and central Missouri along the apparent mean path of the heavier thunderstorms. Mean mid-cloud thickness ranges from slightly less than 0.6 km in the south to almost 2 km over the Colorado Rockies. Mean low-cloud thickness varies from ≈0.25 km to 0.35 km.

Average Radiation Parameters

Figure 25 shows the mean diurnal variation in the clear-sky, total, and effective cloud VIS and SW albedos for the 2.5° and 0.3° regions centered on the SCF. The mean SW effective cloud albedo is

$$\alpha_{swce} = [\alpha_{sw}(\mathrm{LT}) - \alpha_{sw}(\mathrm{CLR, LT})\ (1-C)]/C \quad (23)$$

Both VIS and SW clear-sky albedos increase with solar zenith angle (time from local noon). The slight divergence between the SW and VIS clear albedos during the

early morning and late afternoon arises from the dependence of equation (16) on the solar zenith angle. The total albedos increase only slightly with θ_o. Relative minima in the 0.3° data at 1030 and 1530 LT roughly correspond to the dips in the mean optical depth (fig. 18). Total VIS albedo is greater than the SW albedo around midday and less than the SW albedo at other times as a result of the θ_o dependence in equation (17). The effective cloud albedo is generally higher during the morning than during the afternoon. For example, at 0900 LT α_{swce} is 0.48 compared with 0.45 at 1500 LT for the same solar zenith angle. However, in figure 17, the mean optical depth at 1500 LT is greater than or equal to its 0900 LT counterpart. This apparent discrepancy results from the occurrence of two cumulonimbus events during the month at 1500 LT that produced $\tau > 90$. A comparison of the daily optical depths and effective cloud albedos at these two hours indicates that $\tau < 3$ for almost half the IOP days at 1500 LT compared with less than 25 percent of the days at 0900 LT. During most days, τ (1500) < τ (0900). Thus, the two thunderstorms increased the mean optical depth to values comparable to that at 0900 LT. However, the thunderstorms had a much smaller impact on the mean albedo because of the nonlinear relationship between albedo and optical depth.

The mean clear LW fluxes and IR temperatures in figure 26 vary by 14 W-m^{-2} and 8 K, respectively, during the daylight period for both small and large regions centered on the SCF. Maximum clear-sky LW flux occurs between 1300 and 1330 LT. The maximum mean total IR temperatures and LW fluxes occur at 1530 LT when the mean middle and total cloud amounts diminish (fig. 16). The minimum at 0730 LT is driven by the clear-sky values, while the broad relative minimum between 1100 and 1430 LT in the 0.3° region results from the maxima in high, middle, and total cloudiness. Much of this diurnal structure in the LW flux is smoothed out in the larger region.

The mean domain clear-sky and total albedos in figure 27 reflect the patterns of vegetation and the combinations of cloud amount, optical depth, and latitude, respectively. The clear-sky narrowband albedos for heavily forested areas are generally less than 0.13 with greater values in the north. Mixed forest, farmland, and tall-grass prairie areas have VIS clear-sky albedos between 0.13 and 0.15, and α_v (CLR) for mixed prairie and wheat-growing areas varies between 0.15 and 0.17. Clear-sky VIS albedo is greater than 0.17 for the high plains' desert ($z_s > 1.2$ km in fig. 1) and steppe regions. The clear-sky albedo also increases slightly with latitude because of increasing θ_o. In figure 27, the clear-sky albedos are generally greater than their counterparts in figure 14 because the latter were measured near local noon. Shortwave clear-sky albedos are greater than their VIS counterparts in figure 27 by 0.02 to 0.05. The values of α_{sw}, which vary from 0.17 to 0.22, are consistent with the theoretical models presented by Briegleb et al. (1986). This range in values exceeds the ERBE range of 0.15 to 0.21 (see fig. A2) by 0.01. Total albedo is at a maximum near 39°N and in central Nebraska because of (1) maxima in total cloud amount (fig. 21), (2) the relatively high optical depths ($\tau > 9$), and (3) the greater solar zenith angles. More cloudiness was observed in the southeastern corner, but $\tau < 9$ in those regions. The lowest total albedos are found in the southwest. The SW albedos are greater or less than the VIS albedos for α_v less or greater than ≈0.30 as expected from the VIS-to-SW conversion formula (fig. 5).

Figure 28 shows the mean IR temperatures and LW fluxes for the domain. Clear-sky temperatures range from 281 K near the Rockies to 300 K in the southwest. The clear-sky LW flux follows a similar pattern varying from ≈257 to 285 W-m^{-2}. These values result from an average taken over all daylight hours and are much less than those shown in figure 15 for observations taken near local noon. The lowest values of mean total temperature and LW flux coincide with maxima in the high-cloud amounts (fig. 21). The clearest, warmest areas in the southwest have maximum fluxes of ≈270 W-m^{-2}. Inclusion of nighttime fluxes and temperatures would considerably reduce the values in figure 28.

Discussion

The assumptions used to interpret the data leave much room for uncertainty in the derived products. Quantification of all uncertainties is not possible. However, the sources of uncertainty are discussed here and estimates of their impact on a particular cloud property are noted when possible.

Cloud Amount

Clouds typically do not completely fill all pixels, and clear pixels are not always entirely free of clouds. The VIS and IR thresholds are set to some value above the expected clear-sky values. Thus, some pixels with small amounts of cloudiness are classified as clear and some pixels with clear portions are designated as cloudy. These pixels hopefully offset each other to yield the proper cloud amount for the entire area. Whenever only a few scattered clouds, very thin clouds, or a few clear holes are in a scene, probably no compensatory effects will occur due to the threshold selection. Wielicki and Parker (1992) performed a study of effects of pixel resolution on cloud amount using several different analysis algorithms. Although different thresholds and pixel averaging techniques are used, the LBTM is most similar to the ISCCP method highlighted in the Wielicki and Parker

(1992) study. For the 24 Landsat scenes examined by Wielicki and Parker (1992), the ISCCP method using 4-km resolution data overestimated cloud cover for various broken water-cloud scenes by 0.025 and underestimated cirrus by 0.08. Similar values may be expected for the LBTM in like conditions. The Landsat study was specifically focused on broken and scattered cloud fields and very thin cirrus clouds. It was also restricted to the Landsat's near-nadir viewing angle. Over the course of a month, both thin and thick stratiform and cumuliform clouds will pass over a given area reducing the influence of broken cloud scene errors. The GOES viewing angle to the SGP locale is ≈44°. Thus, the overall effect of uncertainties due to resolution and pixel-filling are still undetermined. Evaluation of higher resolution data and comparisons with other observations are needed to assess the errors in cloud amount.

Comparisons were performed with visual observations from Whiteman Air Force Base (WAFB) at 38.73°N, 93.55°W and Tinker Air Force Base (TAFB) at 35.42°N, 97.38°W to examine the uncertainties in total cloud cover. These datasets were used because they included total sky cover estimates and comments about sky conditions. The hourly surface observations (taken in tenths of sky cover converted to percentages) C_{sfc} were compared with values of C from the 0.5° region centered at 38.75°N, 93.75°W, from a 1.0° region centered on WAFB, and from the 1.0° region (average of two 0.5° regions: 0.5° longitude by 0.5° latitude) immediately surrounding TAFB. From the surface, the viewing radius for high clouds is ≈40 km and much smaller for low clouds. Figure 29 shows the mean LBTM cloud amounts found for each tenth of sky cover. The number of observations in each tenth is shown at the top of each plot. The LBTM data were linearly interpolated to fill in a few missing hours. Nearly complete agreement was obtained for all clear and overcast skies, as shown from the surface. Over WAFB (fig. 29(a)), two cases occurred for which the surface reported clear and the LBTM retrieved a few percent low clouds. These clouds are evident in the northwest corner of the box in the imagery and could not have been viewed by an observer at the center of the box. Although many cases occurred for which the surface reported less than 100-percent cloudiness and the satellite based cloudiness was 100 percent, no cases occurred for the opposite. Thus, the LBTM as formulated here generally will not produce cloud observations when there are no clouds and will not produce clear spots when none exists. Exceptions may arise over snow surfaces or in shadows.

Figure 29(a) clearly shows that the LBTM tends to overestimate cloud fraction relative to sky cover for larger cloud amounts and underestimate for smaller fractions of sky cover. Surface observers record a minimum of 10-percent sky cover if any clouds are observed and a maximum of 90 percent if the clouds have any holes. Thus, some relative under or overestimation by the satellite is expected for the 10- and 90-percent sky cover categories. However, the underestimation of sky cover for the range where 10 percent < C_{sfc} < 60 percent is primarily the result of missing thin cirrus or some scattered small, low cumulus clouds. A detailed examination of the data over WAFB revealed that on some occasions these clouds did not produce a signal large enough to be detected in either the VIS or IR channels. In several cases, even extreme contrast enhancement failed to reveal the clouds in the satellite data. Detection of such clouds with an automated scheme involves a greater risk of false cloud identifications. The overall impact of missing these extremely tenuous clouds on the total cloud fraction or on other aspects of the water or radiative balance is minimal because of their relatively small optical depth, areal coverage, and water content. More cloud cover was found in the 1.0° region than in the 0.5° region. Sometimes the clouds viewed by the surface observer occurred to the east of WAFB so that they were missed in the 0.5° region. This difference is evident in the relative number of partly cloudy (10 to 40 percent) surface reports that were determined as clear by the LBTM. For the partly cloudy surface reports, no clouds were found in 41 and 16 percent of the satellite retrievals for the 0.5° and 1.0° regions, respectively. Thus, the comparison with the 1.0° region is probably a better guide to the relative accuracy of the LBTM.

Much better agreement exists between the LBTM and the TAFB data (fig. 29(b)). Although the trends are similar to the WAFB results, the differences for C_{sfc} < 60 percent are much smaller. Fewer overcast and clear cases and 15 percent more broken and scattered cloud conditions occurred at TAFB than at WAFB. Whether the differences in the two satellite-surface comparisons are due to the particular observers at the two locations, the clouds, or the angular conditions is uncertain. Considerable evidence and logic exists for expecting some systematic differences between surface-observed and satellite-derived cloudiness. Henderson-Sellers and McGuffie (1990) explored this idea with all-sky camera photographs to simulate sky cover and Earth cover (satellite viewed cloudiness). They derived a relationship in oktas that converts to

$$C = 0.0459 + 0.0694C_{sfc} + 0.0219C_{sfc}^2 - 0.000125C_{sfc}^3 \quad (24)$$

when C is expressed in percent. Equation (24) was used to compute the expected satellite-observed cloudiness and compared to the averaged decile cloud amounts from

WAFB and TAFB (fig. 30). Except for the disagreements at 40 and 80 percent, the empirical model is consistent with the LBTM-surface comparison. Thus, viewing perspective may explain much of the difference between the surface and satellite observations.

Figure 31 presents the mean hourly cloud amounts for all times when there are observations for both the satellite and surface sites. Except for the first three morning hours, the mean LBTM cloudiness for the 1.0° region is within ±2 percent of the WAFB averages (fig. 31(a)). The differences in the mean morning cloud amounts are due to the thin cirrus problem noted earlier. The agreement with the 0.5° region is not quite as good with 8-percent differences at 1600 and 2300 UTC. Some differences between the surface and 0.5° region are due to the mismatched fields of view as noted earlier. All three curves are well matched during most of the afternoon. Overall, the satellite estimates for the 0.5° and 1.0° regions are 2.9 and 1.9 percent less than the WAFB sky cover, respectively. The hourly means have rms differences of 4.3 and 2.9 percent, respectively. The average difference for the 1.0° region is less than half the mean difference found between International Satellite Cloud Climatology Project (ISCCP) daytime land cloudiness and surface observations (Rossow, Walker, and Garder 1993). Slightly better correspondence exists between the TAFB observations and the LBTM results for the surrounding $1.0° \times 0.5°$ region in figure 31(b). Here, the LBTM mean cloudiness is only 0.5 percent less than the surface. The hourly mean rms difference is 2.3 percent.

Figure 32 shows the mean hourly, surface-observed cloudiness for the SCF compared with the averaged 0.3° domain LBTM results (fig. 32(a)) and for Vance Air Force Base (VAFB) at 36.33°N, 97.92°W compared with two 0.5° grid boxes straddling VAFB (fig. 32(b)). VAFB is only ≈31 km from the SCF. Although the LBTM mean cloudiness exceeds the SCF data by 3.1 percent, it is 0.9 percent less than the VAFB results. The hourly mean rms differences are 4.6 and 4.1 percent, respectively. The VAFB results are consistent with the other Air Force comparisons. The overestimate of the satellite cloud amount compared with the SCF may be due to differences in the surface observer's reporting. The SCF observers report fractional cloudiness for each sky quadrant. These quantities were then averaged to obtain the total sky coverage. Also, the Air Force observers may have been trained differently than the SCF observers. The SCF mean cloud amount is 8.6 percent less than the VAFB, which is almost twice the difference between the corresponding LBTM results. Overall, the mean LBTM cloudiness is 1.1 percent less than the mean for the three Air Force bases. Inclusion of the SCF results yields an average difference of –0.1 between the LBTM and surface results. The corresponding hourly mean rms differences are 3.2 and 3.6 percent, respectively.

Given the assumption that the surface observer cannot determine cloud amount to better than ±15 percent for a given observation in scattered or broken cloud conditions, the uncertainty in the hourly mean for the 27-day period would be ≈3 percent. Thus, the LBTM hourly means would be within the uncertainty of the surface-observed hourly averages. However, the uncertainty in the surface-observed cloud fraction is probably less than 15 percent because of the frequent occurrence of overcast and clear skies, which are generally accurately observed. Perfect agreement with surface observations is also not expected because of both the subjective nature of the surface data and the cloudbase-height-dependent surface area that corresponds to the sky cover reports.

Although the comparisons with the surface observations are encouraging, they represent only four regions in the domain. Other factors such as snow cover, which occurred over some regions during the month, are misinterpreted as clouds. If the snow is thick, it may be mistaken for an optically dense cloud. The brighter surface in the western part of the domain may exacerbate the identification of thin cirrus clouds because of diminished contrast over barren surfaces. Until more effective measures are developed for identifying snow and thin clouds, users of these data products must take such limitations into account.

Cloud Height and Layering

Cloud-center height errors for the LBTM were examined by Minnis, Heck, and Young (1993) for cirrus clouds over Wisconsin. The cirrus heights were within ±1.3 km of the values derived from lidar images. With uncertainties in the lidar-derived altitudes taken into account, the uncertainty in the cirrus altitudes for clouds having $\tau < 5$ is about ±1.0 km. Similar results were found by Minnis, Young, et al. (1992) and Smith et al. (1993). All clouds having $T_c > 253$ K are assumed to consist of water droplets. If the cloud is thin and consists of ice crystals, the altitude is underestimated by a factor that depends on the angles and optical depth. For thicker clouds, the errors in z_c and z_t are much smaller because the observed temperature of the cloud is close to the actual temperature. Thus, the vertical placement of the cloud will be somewhat dependent on the accuracy of the temperature profile. For single-layer clouds, the typical retrieved cloud-top or center height is estimated to be accurate to less than 1 km and 0.5 km for thin and thick clouds, respectively. For thick clouds over thick clouds, the errors are the same for the single-layer case. If a thin cloud overlays a thick cloud, the cloud-top altitude is underestimated because the algorithm interprets the VIS

data as an optically thick cloud. Thus, the derived altitude falls between the lower cloud and upper cloud. The error depends on the height difference between the two clouds, the upper cloud optical depth, and the viewing angle. Some validation of the cloud heights may be possible by using the surface data taken during the April IOP.

The WAFB observations are useful for examining how the layering of the clouds differs depending on the viewpoint. Three levels of cloudiness were recorded as scattered, broken, or overcast for the first three layers observable from the surface. Estimates of cloudbase height were used to assign the clouds to a layer comparable to the LBTM estimates. Cloud fraction at each level was assigned a value of 0, 33, 67, and 100 percent depending on its cloudiness categories. Using only the synoptic hours 1500, 1800, and 2100 UTC, multilayer and single-layer clouds were observed 42 and 36 percent of the time, respectively. Although the satellite detected clouds at more than one level 58 percent of the time, single-layer clouds comprised only 23 percent of the satellite results. Low, middle, and high cloud amounts from the surface were 31.2, 23.1, and 35.1 percent, respectively. The corresponding LBTM estimates for the 1.0° region (e.g., fig. 30) are 5.9, 24.8, and 31.3 percent. The low-cloud differences are primarily due to upperlevel clouds obscuring the low clouds from the satellite perspective. The greater frequency of multilayer clouds in the satellite results arise from several factors. Variable high-cloud emissivity over a lower level cloud will yield a variable cloud height because the data are interpreted as being optically thick. The layering of the clouds above low overcast cannot be determined from the surface but can be estimated from the satellite. When a cloud's altitude overlaps two different levels, two cloud layers are identified. Some partially high-cloud-filled pixels may be interpreted as lower clouds. These various factors make precise determination of cloud layering from either perspective difficult.

To examine some differences in viewing perspective, all cases containing low clouds were removed when one of the upper layers was reported as overcast or when rain was noted (assumes the clouds are thick enough to extend into the higher layers). The low-cloud fraction from the remaining surface observations reduces to 8.1 percent, a value close to the satellite result. Middle clouds are eliminated when the highest level is reported as overcast. The middle-cloud amount is only given half weight when the low or middle levels are overcast and a thunderstorm is reported. If low overcast occurs with rain, the middle clouds are assumed to be overcast. This correction yields an estimate of 24-percent midlevel clouds from the satellite. Finally, the observed high-cloud fraction is altered by assuming that 50 percent of the sky is covered by high clouds when a thunderstorm is reported and lower clouds obscure the high clouds. The result is a net increase in high-cloud amount to 38 percent. The sum of these "adjusted" cloud amounts is 70 percent, a value slightly greater than the mean sky cover. Such a correction is subject to a number of errors because of the assumptions made in the formulation. Nonetheless, the results are consistent with the satellite-derived cloud amounts in each layer. As previously noted, the greater amount of high cloudiness estimated from the surface data is probably due mostly to the thin cirrus clouds missed by the satellite analysis. While this comparison provides a somewhat quantitative verification of the layer cloud analyses, it clearly demonstrates the limitations in understanding the cloud field when only one view is available.

Cloud Optical Depth and Thickness

Cloud optical depth uncertainties are more difficult to evaluate. Some errors are expected to occur from the use of a parameterization instead of a fully detailed radiative transfer model. The parameterization errors are given by Minnis, Liou, and Takano (1993) and are less than 10 percent for the types of backgrounds in the SGP domain and for the angles observed in this dataset. The three-dimensional characteristics of real clouds also affect the optical depths retrieved with the plane-parallel model. The magnitude of this error is unknown. Minnis, Heck, and Young (1993) compared values of τ derived by using simultaneous GOES and AVHRR data taken over inhomogeneous cirrus clouds from different angles. They found that the mean optical depths derived from the AVHRR angles were 9 percent greater than those derived from the GOES angles with the CS model. The rms difference is 45 percent. That comparison provides an overall estimate of the uncertainty in τ for single-layer cirrus clouds. A similar study for water droplet clouds has not been conducted yet. The errors for broken water clouds are probably close to those found for the cirrus clouds because the cirrus clouds in the Minnis, Heck, and Young (1993) study were generally very inhomogeneous. The errors are likely to be smaller over thicker stratiform clouds. If an ice cloud has $T_c > 253$ K, its optical depth is usually overestimated because of the water-droplet model used in the analysis for midlevel clouds. An examination of the ISCCP data for April 1984–1991 indicated that cloud optical depth in the SGP locale is highly variable interannually. The optical depths in figure 18 for the 2.5 region are within one standard deviation of the mean April 1984–1991 values for the closest ISCCP region.

Cloud thickness is a remote-sensing product that has received minimal attention. The formulae used to compute cloud thickness are limited in scope and have not

yet been tested with independent datasets. The rms regression errors for equations (12) and (13) are ±0.92 and 0.06 km, respectively, and were found using only single-layer cloud systems. It is not known if these errors apply to the data analyzed here. The impact of cloud overlap is also uncertain. Correlative measurements from instruments such as radar are needed to evaluate the derived cloud depths.

The distributions of middle- and high-cloud thicknesses in figure 20 are somewhat similar to those reported by Carswell et al. (1995) for lidar observations taken at Toronto, Canada. Although the Carswell et al. (1995) data were taken in a different area and period and only represent relatively thin clouds, the data provide an example of true thickness variability. The Toronto midlevel clouds have a thickness frequency that peaks between 0.27 and 0.50 km and decreases with increasing thickness to values greater than 3.0 km. The Toronto high clouds have a broad maximum in thickness between 0.20 and 1.50 km with decreasing occurrences up to 3.0 km. Those distributions are similar to the histograms in figure 20 without the thickest clouds. The tops of thicker clouds, however, could not be detected with the lidar. Maximum low-cloud thicknesses over Toronto occurred between 0.4 and 0.6 km. Those maximum values are more than twice the values found in figure 20 for low clouds. Some difference may be caused by the viewing perspective. Surface-observers determine low cloudiness from the base altitude, while the satellite uses the top altitude. Thus, some low clouds over Toronto could be designated as middle clouds by the satellite. More likely, the formula for estimating low-cloud thickness may underestimate cloud thickness over land because it is based on measurements of marine stratocumulus clouds. The comparison with the Toronto results does not verify the thicknesses derived in this study. It indicates, however, that satellite-derived values for the midlevel and high clouds are realistic and that a different approach may be needed for the lower clouds. Radar data taken during ARM IOP's and other experiments will be useful for improving cloud thickness estimates.

Radiation Properties

Some clouds can act as plane-parallel sheets, especially stratiform and optically thick clouds with small vertical aspect ratios (thickness/width). Cumuliform clouds and many cirrus clouds have complex shapes and may have relatively large (>0.5) aspect ratios. Thus, the radiances reflected by these latter cloud types may differ substantially from those by plane-parallel clouds. This effect is readily seen for cumulonimbus clouds and the edges of thick stratus clouds when the Sun is off the zenith and illuminates the sides of the clouds. The cloud appears brighter than normal when viewed from the solar side and darker than normal when viewed from the shaded side. An extreme example was observed at 2130 UTC, April 10 in the 0.3° region centered over the central facility. The edge of a large cloud was illuminated, which resulted in a VIS albedo of 1.03. This value is unrealistic, especially since some visible radiation is absorbed by ozone. Such effects can be minimized by averaging over larger scales that include the tops as well as the sides of the clouds. Because the geostationary satellite always views a given area at a constant angle, accounting for shading is not always possible, especially in extratropical latitudes where the relative azimuth angles are usually greater than 90°. The anisotropic reflectance models are based on observations and implicitly account for some nonplane-parallel effects. However, the models cannot account for the extreme variations from the mean that are observed in some cases.

The anisotropic corrections for clear land are also general empirical models that may not be totally applicable to the particular surfaces and clear atmospheres in this dataset. However, the results indicate that the corrections are relatively accurate. Figure A3 (see appendix A) shows that the clear-sky reflectance is lower in the morning than during the afternoon. Except for cases of frost, dew, or haze that are diurnally dependent, the clear-sky albedo is expected to vary only with the solar zenith angle. Thus, the albedo should be symmetrical about local noon. Also, the surface and clear-sky albedos typically increase with solar zenith angle, which results in higher values in the morning and evening and a minimum value near noon. The VIS clear-sky albedos in figure 25 are almost symmetrical about the minimum at local noon. (The symmetry is evaluated in the next paragraph.) These albedos are based on clear-sky reflectances that are very similar to those in figure A3. Thus, the correction factors have at least resulted in albedos that are consistent with the typical behavior. Simultaneous views from other satellites or from aircraft are needed to quantitatively assess anisotropic correction uncertainties for both cloudy and clear conditions.

Errors in the LW fluxes and SW albedos due to the conversion process from narrowband-to-broadband fluxes are represented by the standard errors of the estimate given previously. Further comparisons with ERBE data, however, are needed to evaluate the data after the conversion formulae are applied. Clear-sky albedos derived from April 1985 ERBS data over the regions straddling the SCF are plotted as a function of μ_o in figure 33 with the mean 1994 SW clear-sky albedos for the same area derived from the GOES-7 data. ERBS data were used only when more than 50 percent of the ERBS pixels were identified as clear. This comparison shows that the GOES-derived albedos agree well with the

earlier ERBE observations at low solar zenith angles but diverge from the ERBE values at higher angles (lower μ_o). Both the GOES and the ERBE results can be fitted with a quadratic curve. The respective regression fits for the observed range of μ_o are

$$\alpha_{sw}(\text{ERBE}) = 0.341 - 0.358\mu_o + 0.201\mu_o^2$$

and

$$\alpha_{sw}(\text{GOES}) = 0.363 - 0.356\mu_o + 0.161\mu_o^2$$

The rms differences in the mean clear-sky albedos integrated over the observed solar zenith angle range is 5.6 percent. Given that the 1-σ interannual variability in clear-sky albedo is 5 percent over the domain (see appendix A), some difference may be due to interannual variability. Some difference is probably due to errors in the anisotropic correction. Note also that the sampling of the ERBE data is relatively sparse possibly as a result of the ERBE scene selection scheme (Wielicki and Green 1989), which rejects albedos greater than the preordained values.

Uncertainties in the VIS channel calibration further influence the derived broadband albedos. Although the VIS calibration was shown to be reasonable, the accuracy can be improved by using other methods to calibrate the GOES VIS channel. A bias in the albedos is likely to result from a calibration error. Indirect techniques such as those used by Whitlock, LeCroy, and Wheeler (1994) or direct methods that align well-calibrated, airborne, small field-of-view radiometers with the satellite view yield more reliable calibrations and a more accurate assessment of the uncertainties in the observed radiances than the approach used here. The IR-LW conversion is applied with the assumption that the GOES IR calibrations in April 1985 and 1994 are identical. Any difference in the thermal channel calibrations will cause a bias in the derived LW fluxes.

Concluding Remarks

Version 1.0.0 of the Atmospheric Radiation Measurement (ARM) satellite data analysis program has been described and applied to Geostationary Operational Environmental Satellite (GOES) data taken during April 1994. This initial step in the development of a comprehensive analysis program yields reasonably accurate cloud properties given the limitations of field of view and spectral coverage of the satellite instrument. A technique for calibrating the GOES VIS (visible) channel has also been described and validated with clear-scene reflectances. This cloud retrieval program is the first to take advantage of the extensive array of surface and sounding observations because it has been developed on the Man-computer Interactive Data Analysis System (McIDAS). The McIDAS has an extensive, near-real-time set of meteorological data. The availability of coincident surface observations over much of the domain permits the application of more accurate constraints on the clear-cloud thresholds than previously possible. The results of this analysis provide the highest resolution satellite-derived cloud product available for ARM studies and fill a gap between surface measurements and general circulation models (GCM). These data can be accessed on the Internet via the World Wide Web at the following uniform resource locator:

`http://albedo.larc.nasa.gov:1123/arm.html`

Future versions of this analysis technique will diminish some shortcomings of the present version by incorporating additional spectral channels and provide a greater array of cloud products. New methods for incorporating more surface observations will also be explored.

NASA Langley Research Center
Hampton, VA 23681-0001
July 7, 1995

Appendix A

Calibration of GOES-7 Visible Channel Using NOAA-11 AVHRR

The GOES VISSR (Geostationary Operational Environmental Satellite Visible Infrared Spin Scan Radiometer) visible channel comprises eight sensors that have a nominal resolution of 1 km at nadir. The 4-km and 8-km resolutions used in the cloud and radiation analyses are obtained by computing the root mean square of the digital counts for sets of 4×4 or 8×8 line-element arrays of contiguous data. The gain of each sensor may be periodically adjusted to account for degradation, striping, and seasonal variations in the insolation at the top of the atmosphere. Thus, the overall calibration gain of the visible data is subject to considerable variability. The infrared (IR) sensor is nominally an elongated field of view with a nominal resolution of 4 km in the scanning (east-west) direction and 8 km in the line (north-south) direction. The 4-km and 8-km resolutions are obtained by duplicating scan lines or averaging scan elements, respectively. An onboard thermal blackbody, which is used to monitor the IR channel gain, keeps the IR sensor calibrated. Except for the eclipse periods near the equinoxes, the VISSR IR channel yields relatively stable values of equivalent blackbody temperature. Therefore, the visible channel has the most acute need for calibration.

The most recent calibration of the GOES-7 visible channel was performed during December 1991 by Whitlock, LeCroy, and Wheeler (1994) using a surface-based indirect method. Given the variability of the GOES-7 gain, simply using the 1991 value is not feasible. To achieve a more applicable gain for April 1994, the NOAA-11 Advanced Very High Resolution Radiometer (AVHRR) is used to perform an intercalibration with GOES-7. The NOAA-11 is in a Sun synchronous orbit with an equatorial crossing time of ≈0400 and 1600 LT during April 1994. Its visible sensor (channel 1) is not adjusted; however, its response may degrade with time. The NOAA-11 AVHRR channel 1 was calibrated several times by various methods between September 1988 and December 1991. This time series of calibrations (Whitlock, LeCroy, and Wheeler 1994) was used to compute a correction for the sensor degradation that is assumed to have continued at the same rate until its failure during September 1994. The AVHRR gain is

$$g_A = 0.567 + 0.0000352 d_{sl} \qquad \text{(A1)}.$$

where d_{sl} is the number of days since launch on September 24, 1988. The reflectance in percent for the Sun at 1 AU is

$$\rho_A = \frac{g_A}{5.13}(D_A - 40.0) \qquad \text{(A2)}$$

where D_A is the 10-bit AVHRR visible count. The GOES-equivalent radiance is

$$L_A = 5.269 \rho_A \delta \qquad \text{(A3)}$$

The value of L_A is then adjusted to correspond to a GOES view by correcting for the differences in the viewing and illumination angles as follows:

$$L_G = \frac{\chi(\theta_o, \theta, \psi)_G \, \mu_{oG}}{\chi(\theta_o, \theta, \psi)_A \, \mu_{oA}} L_A \qquad \text{(A4)}$$

where χ is the mean anisotropic reflectance correction factor and the subscripts A and G refer to the GOES and AVHRR, respectively. The values of χ are determined by weighting the clear-sky and cloudy factors by the clear and cloudy portions of the scene as determined from the GOES data.

The April 1994 GOES-7 and NOAA-11 AVHRR data were matched on the 0.5° grid for the Atmospheric Radiation Measurement (ARM) mesoscale regime. Values for L_G were computed with equation (A4) and the average AVHRR channel-1 10-bit counts. These data were regressed against the root mean square GOES counts for the same regions taken within 15 min of the AVHRR overpass. The initial, unconstrained regression that was obtained by using all the data produced the dotted line in figure A1. The initial fit has $R^2 = 0.93$ and intercepts the X-axis at 417. During April 1994, the GOES visible offset count (4.7) was determined by viewing space with the satellite. Thus, the regression fit should cross the X-axis at 22. The data were regressed again forcing the offset to the observed value. The results are shown in figure A1 with the dashed line. Relatively poor sampling and considerable scatter occurred in the data for $D^2 > 10000$. The brighter points, however, have a significant effect on the regression line. The anisotropic correction for the clear land is expected to be more reliable than the correction for clouds (brighter scenes), which will result in less scatter for the darker scenes. To minimize the effects of the unbalanced sampling and cloud anisotropy, only those data having $D_G < 100$ were

used in the regression. The resulting formula, shown as the solid line in figure A1, is

$$L_G = 0.0127D_G^2 - 0.2804 \qquad \text{(A5)}$$

This relationship, based on 300 matched data points, is used for the April 1994 ARM intensive observing period (IOP).

To ensure that this approach is reasonably accurate, the resulting narrowband VIS clear-sky reflectances were compared with those determined over the same area during April 1985. Over any given land area, except in variable snow conditions, the clear-sky albedo should remain relatively constant from 1 year to the next. This interannual consistency is evident in the April clear-sky SW albedos computed from the ERBE data over the ARM Southern Great Plains (SGP) domain for 1985 to 1989. Figure A2 shows a scatterplot of the annual clear-sky SW albedos with the April 1985 to 1989 means for the 2.5° regions within the SGP domain. The smaller albedos ($\alpha_{sw} < 0.19$) primarily correspond to the regions east of the central facility, and the others are west of the site. The variability in α_{sw} is greater for the western regions presumably because of interannual differences in snow cover, soil moisture, and vegetation growth. The surface albedos in the eastern areas are probably less sensitive to soil moisture because of greater forest coverage. The overall interannual variability for the domain is ±0.011 or ≈5 percent as measured at the two standard deviation σ levels. Because the VIS albedo is directly proportional to the shortwave (SW) albedo, the interannual variability in α_{sw} should be approximately the same for the visible (VIS) data. Thus, the clear-sky reflectance or albedo should not differ from 1 year to the next by more than 10 percent (2-σ level is 5 percent).

Two datasets, the April 1985 GOES-6 data analyzed with the hybrid bispectral threshold method (HBTM) and by the International Satellite Cloud Climatology Project (ISCCP) by Rossow and Schiffer (1991) are used to evaluate the April 1994 results. The ISCCP methodology (Rossow and Garder 1993) differs from the HBTM in several respects. It uses 3-hourly, 8-km data sampled every 32 km and has slightly different criteria for selecting clear scenes. However, both techniques should yield similar clear-sky reflectances. Reflectances are used instead of albedos because the ISCCP assumes Lambertian reflectance for all land surfaces. The monthly mean hourly clear-sky reflectances are plotted in figure A3 for the four 2.5° regions near the corners of the SGP large-scale domain. The 1994 values closely track the 1985 HBTM results except during midmorning. The 1994 albedos in the upper right corner are slightly greater than those observed in 1985. The ISCCP results are consistent with the 1985 HBTM values except for the lower right quadrant. The ISCCP values are probably in error for this region because the morning values in the other regions are less than the afternoon values. This diurnal pattern is unlikely to change for the lower right region.

Overall, the mean difference between the hourly 1985 HBTM and 1994 ARM reflectances is –0.006 with an rms difference of ±0.013 or 9 percent. The rms difference between the regional means (integrated over the diurnal cycle), 0.0036 or 2.5 percent, is well within the ERBE interannual differences. If the dashed lines in figure A1 were used instead of equation (A5), the mean difference would have been 7 percent, or almost twice the mean value obtained with equation (A5). The rms differences between the hourly 1985 HBTM and ISCCP albedos are 8.6 percent or 7.6 percent if the lower right quadrant is excluded. Similarly, the 1994 LBTM and 1985 ISCCP rms albedo differences are 11.1 percent and 7.9 percent if the lower right region is excluded. The monthly rms differences between the daily mean 1994 and ISCCP albedos is 7.8 percent. The same quantity computed for the ISCCP and HBTM albedos is 6.9 percent. From the consistency between the 1985 HBTM and 1994 LBTM clear-sky albedos and for most ISCCP data, it is concluded that the GOES calibration procedure used for the 1994 data will produce reasonably accurate VIS albedos.

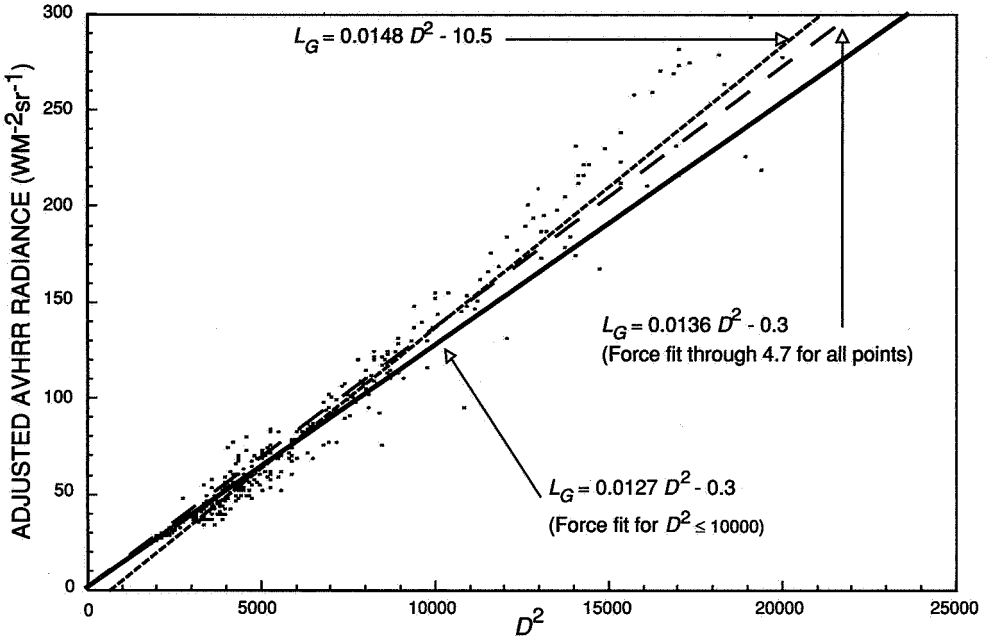

Figure A1. Intercalibration of April 1994 NOAA-11 AVHRR VIS radiances corrected to GOES angles and squared GOES-7 VIS counts; original regression fit shown by small dashed lines; final fit only used points for $D^2 < 10000$.

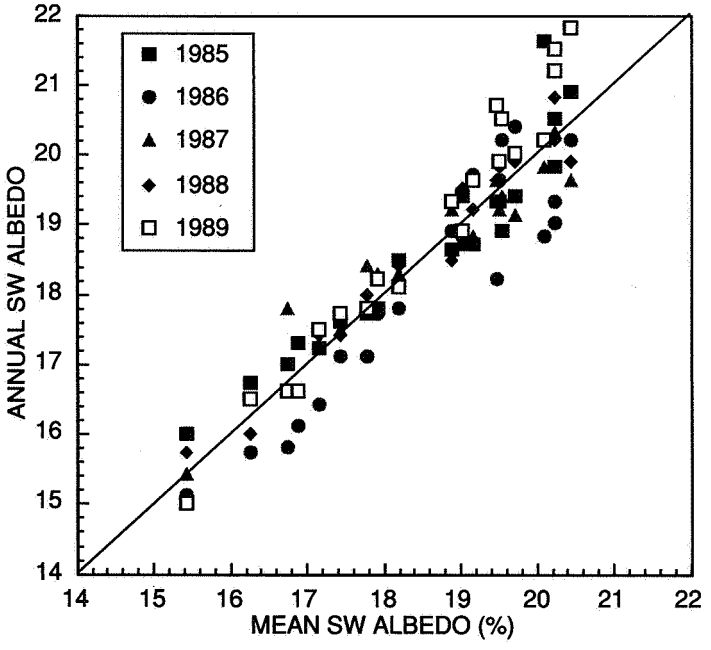

Figure A2. Mean April 1985–1989 and annual ERBE SW clear-sky albedos for 2.5° regions between 32.5°N and 42.5°N and between 92.5°W and 105°W.

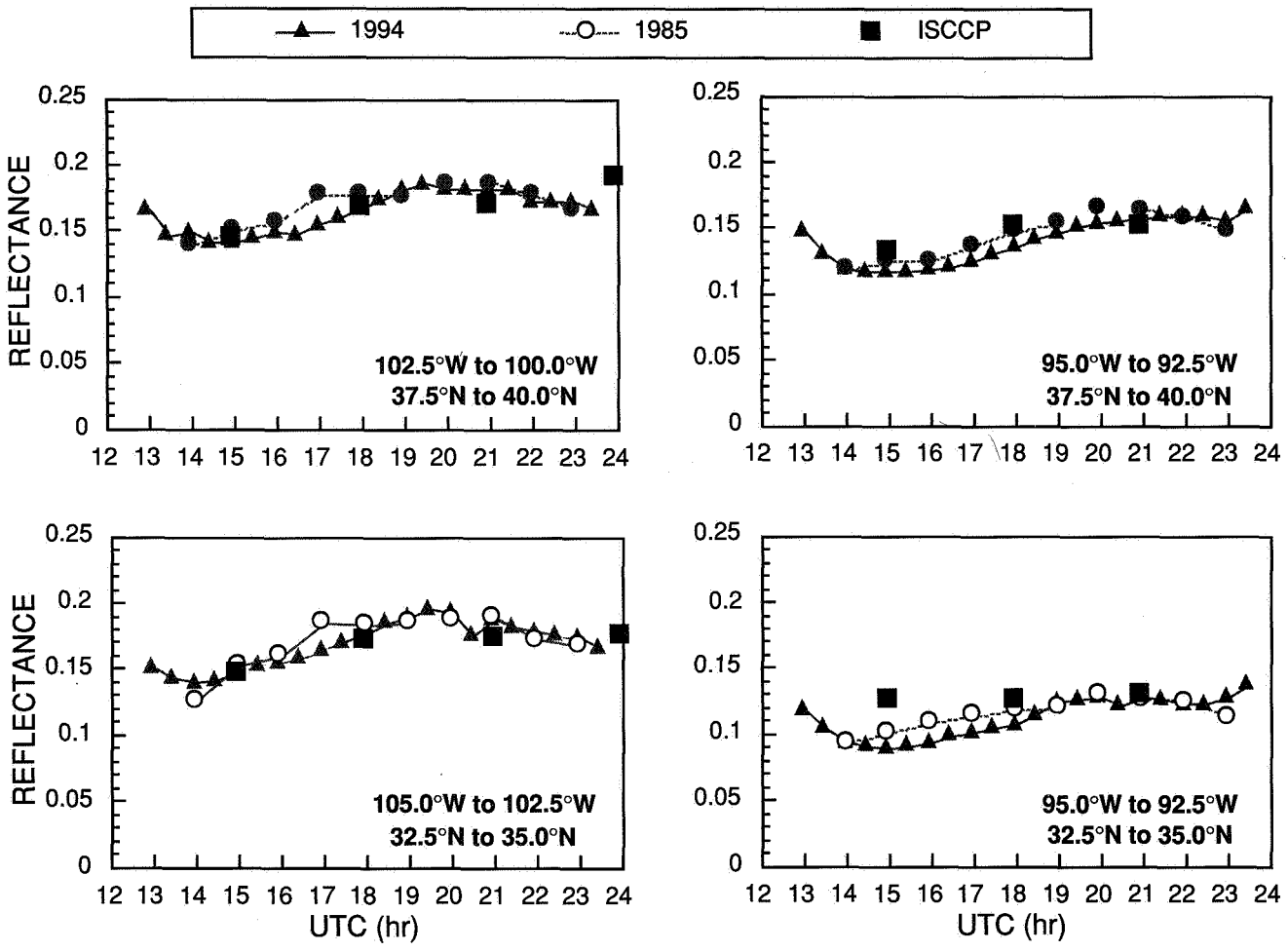

Figure A3. Mean narrowband visible clear-sky albedos for 2.5° regions at corners of SGP large-scale domain.

Appendix B

Format of Archived ARM Satellite-Derived Cloud Properties

The derived cloud properties are archived at NASA Langley Research Center. The Atmospheric Radiation Measurement (ARM) satellite-derived cloud dataset can be accessed on the Internet via the World Wide Web at the following uniform resource locator:

```
http://albedo.larc.nasa.gov:1123/arm.html
```

The archived data are formatted in Network Common Data Form (netCDF) with version 2.3.2 of the netCDF software obtained from the Unidata Program Center. NetCDF interface software includes system callable utilities and input/output functions callable from C or FORTRAN. The system utility `'ncdump'` can be used to generate a netCDF Common Data form Language (CDL) file that describes the format of data stored in a netCDF data file with or without including the variable data contained in the data file. This appendix contains a CDL file generated with the following commands for `ncdump`:

```
ncdump -v base_time,time_offset,latitude,
   longitude,level,view
sgpgoes7minnisX1.c1.940405.133000
```

This sample file is a netCDF data file, `sgpgoes7minnisX1.c1.940405.133000`, containing cloud products from 5 April 1994 over the Southern Great Plains ARM region:

```
netcdf sgpgoes7minnisX1.c1.940405.133000 {
dimensions:
      latitude = 20 ;
      longitude = 28 ;
      level = 4 ;
      view = 2 ;
      time = UNLIMITED ; // (20 currently)
variables:
      long base_time ;
            base_time:string = "0:00:00 GMT 05 April 1994       " ;
            base_time:long_name = "base time in epoch" ;
            base_time:units = "seconds since 0:00:00 GMT 01 January 1970" ;
      double time_offset(time) ;
            time_offset:long_name = "time offset from base time" ;
            time_offset:units = "seconds" ;
      float latitude(latitude) ;
            latitude:valid_range = -90.f, 90.f ;
            latitude:long_name = "north latitude" ;
            latitude:units = "degrees" ;
      float longitude(longitude) ;
            longitude:valid_range = -180.f, 180.f ;
            longitude:long_name = "east longitude" ;
            longitude:units = "degrees" ;
      float level(level) ;
            level:valid_range = 1.f, 4.f ;
            level:long_name = "cloud level" ;
            level:units = "unitless" ;
            level:value_1 = "A value of 1. corresponds to low clouds." ;
            level:value_2 = "A value of 2. corresponds to mid clouds." ;
            level:value_3 = "A value of 3. corresponds to high clouds." ;
            level:value_4 = "A value of 4. corresponds to all clouds." ;
      float view(view) ;
            view:valid_range = 1.f, 2.f ;
            view:long_name = "scene description" ;
            view:units = "unitless" ;
```

```
      view:value_1 = "A value of 1. corresponds to a clear scene." ;
      view:value_2 = "A value of 2. corresponds to the total scene." ;
float Cloud_Amount(time, level, latitude, longitude) ;
      Cloud_Amount:valid_range = 0.f, 100.f ;
      Cloud_Amount:_FillValue = -888.f ;
      Cloud_Amount:missing_value = -999.f ;
      Cloud_Amount:long_name = "cloud amount" ;
      Cloud_Amount:units = "percent cloudy" ;
float Visible_Optical_Depth(time, level, latitude, longitude) ;
      Visible_Optical_Depth:valid_range = 0.f, 200.f ;
      Visible_Optical_Depth:_FillValue = -888.f ;
      Visible_Optical_Depth:missing_value = -999.f ;
      Visible_Optical_Depth:long_name = "visible cloud optical depth" ;
      Visible_Optical_Depth:units = "unitless" ;
float IR_Optical_Depth(time, level, latitude, longitude) ;
      IR_Optical_Depth:valid_range = 0.f, 100.f ;
      IR_Optical_Depth:_FillValue = -888.f ;
      IR_Optical_Depth:missing_value = -999.f ;
      IR_Optical_Depth:long_name = "IR cloud optical depth" ;
      IR_Optical_Depth:units = "unitless" ;
float Emissivity(time, level, latitude, longitude) ;
      Emissivity:valid_range = 0.f, 1.f ;
      Emissivity:_FillValue = -888.f ;
      Emissivity:missing_value = -999.f ;
      Emissivity:long_name = "IR beam cloud emissivity" ;
      Emissivity:units = "unitless" ;
float Cloud_Center_Height(time, level, latitude, longitude) ;
      Cloud_Center_Height:valid_range = 0.f, 20.f ;
      Cloud_Center_Height:_FillValue = -888.f ;
      Cloud_Center_Height:missing_value = -999.f ;
      Cloud_Center_Height:long_name = "cloud center height" ;
      Cloud_Center_Height:units = "kilometers" ;
float Cloud_Top_Height(time, level, latitude, longitude) ;
      Cloud_Top_Height:valid_range = 0.f, 20.f ;
      Cloud_Top_Height:_FillValue = -888.f ;
      Cloud_Top_Height:missing_value = -999.f ;
      Cloud_Top_Height:long_name = "cloud top height" ;
      Cloud_Top_Height:units = "kilometers" ;
float Cloud_Temperature(time, level, latitude, longitude) ;
      Cloud_Temperature:valid_range = 160.f, 330.f ;
      Cloud_Temperature:_FillValue = -888.f ;
      Cloud_Temperature:missing_value = -999.f ;
      Cloud_Temperature:long_name = "uncorrected cloud temperature" ;
      Cloud_Temperature:units = "Kelvin" ;
float Cloud_Thickness(time, level, latitude, longitude) ;
      Cloud_Thickness:valid_range = 0.f, 20.f ;
      Cloud_Thickness:_FillValue = -888.f ;
      Cloud_Thickness:missing_value = -999.f ;
      Cloud_Thickness:long_name = "cloud thickness estimate" ;
      Cloud_Thickness:units = "kilometers" ;
float Reflectance(time, level, latitude, longitude) ;
      Reflectance:valid_range = 0.f, 1.5f ;
      Reflectance:_FillValue = -888.f ;
      Reflectance:missing_value = -999.f ;
      Reflectance:long_name = "cloud narrowband reflectance at TOA" ;
```

```
            Reflectance:units = "unitless" ;
      float Albedo(time, level, latitude, longitude) ;
            Albedo:valid_range = 0.f, 1.f ;
            Albedo:_FillValue = -888.f ;
            Albedo:missing_value = -999.f ;
            Albedo:long_name = "cloud narrowband albedo" ;
            Albedo:units = "unitless" ;
      float Cloud_Center_Temperature(time, level, latitude, longitude) ;
            Cloud_Center_Temperature:valid_range = 160.f, 330.f ;
            Cloud_Center_Temperature:_FillValue = -888.f ;
            Cloud_Center_Temperature:missing_value = -999.f ;
            Cloud_Center_Temperature:long_name = "cloud center temperature" ;
            Cloud_Center_Temperature:units = "Kelvin" ;
      float Cloud_Top_Temperature(time, level, latitude, longitude) ;
            Cloud_Top_Temperature:valid_range = 160.f, 330.f ;
            Cloud_Top_Temperature:_FillValue = -888.f ;
            Cloud_Top_Temperature:missing_value = -999.f ;
            Cloud_Top_Temperature:long_name = "cloud top temperature" ;
            Cloud_Top_Temperature:units = "Kelvin" ;
      float Visible_Optical_Depth_SD(time, level, latitude, longitude) ;
            Visible_Optical_Depth_SD:valid_range = 0.f, 100.f ;
            Visible_Optical_Depth_SD:_FillValue = -888.f ;
            Visible_Optical_Depth_SD:missing_value = -999.f ;
            Visible_Optical_Depth_SD:long_name = "visible optical depth standard
deviation" ;
            Visible_Optical_Depth_SD:units = "unitless" ;
      float Cloud_Center_Temperature_SD(time, level, latitude, longitude) ;
            Cloud_Center_Temperature_SD:valid_range = 0.f, 200.f ;
            Cloud_Center_Temperature_SD:_FillValue = -888.f ;
            Cloud_Center_Temperature_SD:missing_value = -999.f ;
            Cloud_Center_Temperature_SD:long_name = "cloud center temperature
standard deviation" ;
            Cloud_Center_Temperature_SD:units = "Kelvin" ;
      float Broadband_LW_Flux(time, view, latitude, longitude) ;
            Broadband_LW_Flux:valid_range = 0.f, 400.f ;
            Broadband_LW_Flux:_FillValue = -888.f ;
            Broadband_LW_Flux:missing_value = -999.f ;
            Broadband_LW_Flux:long_name = "broadband LW flux for clear and total
scene" ;
            Broadband_LW_Flux:units = "watts per square meter" ;
      float Narrowband_IR_Flux(time, view, latitude, longitude) ;
            Narrowband_IR_Flux:valid_range = 0.f, 100.f ;
            Narrowband_IR_Flux:_FillValue = -888.f ;
            Narrowband_IR_Flux:missing_value = -999.f ;
            Narrowband_IR_Flux:long_name = "narrowband IR flux for clear and
total scene" ;
            Narrowband_IR_Flux:units = "watts per square meter" ;
      float Broadband_SW_Albedo(time, view, latitude, longitude) ;
            Broadband_SW_Albedo:valid_range = 0.f, 1.f ;
            Broadband_SW_Albedo:_FillValue = -888.f ;
            Broadband_SW_Albedo:missing_value = -999.f ;
            Broadband_SW_Albedo:long_name = "broadband SW albedo for clear and
total scene" ;
            Broadband_SW_Albedo:units = "unitless" ;
```

```
      float Narrowband_VIS_Albedo(time, view, latitude, longitude) ;
            Narrowband_VIS_Albedo:valid_range = 0.f, 1.f ;
            Narrowband_VIS_Albedo:_FillValue = -888.f ;
            Narrowband_VIS_Albedo:missing_value = -999.f ;
            Narrowband_VIS_Albedo:long_name = "narrowband VIS albedo for clear
and total scene" ;
            Narrowband_VIS_Albedo:units = "unitless" ;
      float Clear_Temperature(time, latitude, longitude) ;
            Clear_Temperature:valid_range = 160.f, 330.f ;
            Clear_Temperature:_FillValue = -888.f ;
            Clear_Temperature:missing_value = -999.f ;
            Clear_Temperature:long_name = "clear IR temperature" ;
            Clear_Temperature:units = "Kelvin" ;
      float Clear_Temperature_SD(time, latitude, longitude) ;
            Clear_Temperature_SD:valid_range = 0.f, 200.f ;
            Clear_Temperature_SD:_FillValue = -888.f ;
            Clear_Temperature_SD:missing_value = -999.f ;
            Clear_Temperature_SD:long_name = "clear IR temperature standard
deviation" ;
            Clear_Temperature_SD:units = "Kelvin" ;
      float Narrowband_VIS_Albedo_SD(time, latitude, longitude) ;
            Narrowband_VIS_Albedo_SD:valid_range = 0.f, 1.f ;
            Narrowband_VIS_Albedo_SD:_FillValue = -888.f ;
            Narrowband_VIS_Albedo_SD:missing_value = -999.f ;
            Narrowband_VIS_Albedo_SD:long_name = "clear narrowband VIS albedo
standard deviation" ;
            Narrowband_VIS_Albedo_SD:units = "unitless" ;
      float Clear_VIS_Reflectance(time, latitude, longitude) ;
            Clear_VIS_Reflectance:valid_range = 0.f, 1.f ;
            Clear_VIS_Reflectance:_FillValue = -888.f ;
            Clear_VIS_Reflectance:missing_value = -999.f ;
            Clear_VIS_Reflectance:long_name = "clear narrowband VIS reflectance" ;
            Clear_VIS_Reflectance:units = "unitless" ;
      float Average_Total_Temperature(time, latitude, longitude) ;
            Average_Total_Temperature:valid_range = 160.f, 330.f ;
            Average_Total_Temperature:_FillValue = -888.f ;
            Average_Total_Temperature:missing_value = -999.f ;
            Average_Total_Temperature:long_name = "total scene average
temperature" ;
            Average_Total_Temperature:units = "Kelvin" ;
      float Solar_Zenith_Angle(time, latitude, longitude) ;
            Solar_Zenith_Angle:valid_range = 0.f, 90.f ;
            Solar_Zenith_Angle:_FillValue = -888.f ;
            Solar_Zenith_Angle:missing_value = -999.f ;
            Solar_Zenith_Angle:long_name = "solar zenith angle" ;
            Solar_Zenith_Angle:units = "degrees" ;
      float Viewing_Zenith_Angle(time, latitude, longitude) ;
            Viewing_Zenith_Angle:valid_range = 0.f, 90.f ;
            Viewing_Zenith_Angle:_FillValue = -888.f ;
            Viewing_Zenith_Angle:missing_value = -999.f ;
            Viewing_Zenith_Angle:long_name = "viewing zenith angle" ;
            Viewing_Zenith_Angle:units = "degrees" ;
      float Relative_Azimuth_Angle(time, latitude, longitude) ;
            Relative_Azimuth_Angle:valid_range = 0.f, 180.f ;
            Relative_Azimuth_Angle:_FillValue = -888.f ;
```

```
            Relative_Azimuth_Angle:missing_value = -999.f ;
            Relative_Azimuth_Angle:long_name = "relative azimuth angle" ;
            Relative_Azimuth_Angle:units = "degrees" ;
      float alt ;
            alt:long_name = "Dummy altitude for Zeb" ;
            alt:units = "unitless" ;
      float lat ;
            lat:long_name = "Northernmost north latitude for Zeb" ;
            lat:units = "degrees" ;
      float lon ;
            lon:long_name = "Westernmost west longitude for Zeb" ;
            lon:units = "degrees" ;

// global attributes:
            :title = "0.5 degree LBTM cloud products derived from GOES for ARM
Great Plains" ;
            :source = "NASA Langley Research Center" ;
            :version = "LBTM ARM 1.0.0" ;
            :netCDF = "netCDF 2.3.2" ;
            :reference = "Minnis, P., Heck, P. W., and Young, D. F., 1993: Infer-
ence of Cirrus Cloud Properties Using Satellite-observed Visible and Infrared
Radiances. Part II: Verification of Theoretical Cirrus Radiative Properties. J.
Atmos. Sci., 50, 1305-1322." ;
            :visible_calibration = "The visible radiance was calculated according
to R = a * D * D + b, where R is the visible radiance, D is eight bit counts,
a = 0.0127, and b=-.28." ;
            :infrared_calibration = "The nominal GOES calibration was used for
infrared." ;
            :shortwave_NB/BB_correlation = "The shortwave narrowband/broadband
correlation is given by Ab = Abclr * ( 1 - X ) + Abcld * X, with Abclr = a + b *
Anclr + c * ln( 1 / uo ) and Abcld = d + e * Ancld + f * Ancld * Ancld + g * ln(
1 / uo ), where Ab is broadband albedo, Abclr is clear sky broadband albedo,
Abcld is cloudy sky broadband albedo, X is cloudy sky scene fraction, Anclr is
clear sky narrowband albedo, Ancld is cloudy sky narrowband albedo, uo is the
cosine of the solar zenith angle, a = 0.1218, b = 0.3842, c = 0.0605, d = 0.0588,
e = 0.8623, f = -.1190, and g = 0.0624." ;
            :shortwave_NB/BB_reference = "Doelling, D. R., Young, D. F., Arduini,
R. F., Minnis, P., Harrison, E. F., and Suttles, J. T., 1990: On the Role of Sat-
ellite-measured Narrowband Radiances for Computing the Earth\'s Radiation Bal-
ance. Proc. Seventh Conference on Atmospheric Radiation, San Francisco, CA, July,
155-160." ;
            :longwave_NB/BB_correlation = "The longwave narrowband/broadband cor-
relation is given by Mb = a + b * Mn + c * Mn * Mn + d * Mn * ln( h ), where Mb
is broadband flux, Mn is narrowband flux, h is the average relative humidity, in
percent, above the GOES level, a = 63.6, b = 6.628, c = -.0278, and d = -.332." ;
            :longwave_NB/BB_reference = "Minnis, P., Young, D. F., and Harrison,
E. F., 1991: Examination of the Relationship between Outgoing Infrared Window and
Total Longwave Fluxes Using Satellite Data. J. Climate, 4, 1114-1133." ;

data:

base_time = 765504000 ;

time_offset = 48600, 50400, 52200, 54000, 55800, 57600, 61200, 63000, 64800,
    66600, 68400, 70200, 72000, 73800, 75600, 77400, 79200, 81000, 82800,
    84600 ;
```

```
latitude = 41.75 , 41.25 , 40.75 , 40.25 , 39.75 , 39.25 , 38.75 , 38.25 ,
    37.75 , 37.25 , 36.75 , 36.25 , 35.75 , 35.25 , 34.75 , 34.25 , 33.75 ,
    33.25 , 32.75 , 32.25  ;

longitude = -104.75 , -104.25 , -103.75 , -103.25 , -102.75 , -102.25 ,
    -101.75 , -101.25 , -100.75 , -100.25 , -99.75 , -99.25 , -98.75 ,
    -98.25 , -97.75 , -97.25 , -96.75 , -96.25 , -95.75 , -95.25 , -94.75 ,
    -94.25 , -93.75 , -93.25 , -92.75 , -92.25 , -91.75 , -91.25  ;

level = 1 , 2 , 3 , 4  ;

view = 1 , 2  ;}
```

References

Barkstrom, Bruce R.; and Smith, G. Louis 1986: The Earth Radiation Budget Experiment: Science and Implementation. *Reviews Geophys.*, vol. 24, no. 2, pp. 379–390.

Briegleb, B. P.; Minnis, P.; Ramanathan, V.; and Harrison, E. 1986: Comparison of Regional Clear-Sky Albedos Inferred From Satellite Observations and Model Computations. *J. Climate & Appl. Meteorol.*, vol. 25, no. 2, pp. 214–226.

Brooks, David R.; Harrison, Edwin F.; Minnis, Patrick; Suttles, John T.; and Kandel, Robert S. 1986: Development of Algorithms for Understanding the Temporal and Spatial Variability of the Earth's Radiation Balance. *Reviews Geophys.*, vol. 24, no. 2, pp. 422–438.

Carswell, A. I.; Fong, A.; Pal, S. R.; and Pribluda, I. 1995: Lidar-Derived Distribution of Cloud Vertical Location and Extent. *J. Appl. Meteorol.*, vol. 34, no. 1, pp. 107–120.

Doelling, David R.; Young, David F.; Arduini, Robert F.; Minnis, Patrick; Harrison, Edwin F.; and Suttles, J. T. 1990: On the Role of Satellite-Measured Narrowband Radiances for Computing the Earth's Radiation Balance. *7th Conference on Atmospheric Radiation*, AMS, pp. 155–160.

Henderson-Sellers, A.; and McGuffie, K. 1990: Are Cloud Amounts Estimated From Satellite Sensor and Conventional Surface-Based Observations Related? *Int. J. Remote Sens.*, vol. 11, pp. 543–550.

Hibbard, William L.; and Wylie, Donald P. 1985: Efficient Method of Interpolating Observations to Uniformly Spaced Grids. *International Conference on Interactive Information and Processing Systems for Meteorology, Oceanography, and Hydrology*, AMS, pp. 144–147.

Minnis, Patrick; and Harrison, Edwin F. 1984a: Diurnal Variability of Regional Cloud and Clear-Sky Radiative Parameters Derived From GOES Data. Part I: Analysis Method. *J. Climate & Appl. Meteorol.*, vol. 23, no. 7, pp. 993–1011.

Minnis, Patrick; and Harrison, Edwin F. 1984b: Diurnal Variability of Regional Cloud and Clear-Sky Radiative Parameters Derived From GOES Data. Part III: November 1978 Radiative Parameters. *J. Climate & Appl. Meteorol.*, vol. 23, no. 7, pp. 1032–1051.

Minnis, Patrick; Harrison, Edwin F.; and Gibson, Gary G. 1987: Cloud Cover Over the Equatorial Eastern Pacific Derived From July 1983 International Satellite Cloud Climatology Project Data Using a Hybrid Bispectral Threshold Method. *J. Geophys. Res.*, vol. 92, pp. 4051–4073.

Minnis, Patrick; Harrison, Edwin F.; and Heck, Patrick W. 1990: The 27–28 October 1986 FIRE IFO Cirrus Case Study—Cloud Parameter Fields Derived From Satellite Data. *Mon. Weather Rev.*, vol. 118, pp. 2426–2446.

Minnis, Patrick; Harrison, Edwin F.; and Young, David F. 1991: Examination of the Relationship Between Outgoing Infrared Window and Total Longwave Fluxes Using Satellite Data. *J. Climat.*, vol. 4, pp. 1114–1133.

Minnis, Patrick; Heck, Patrick W.; and Young, David F. 1993: Inference of Cirrus Cloud Properties Using Satellite-Observed Visible and Infrared Radiances. II—Verification of Theoretical Cirrus Radiative Properties. *J. Atmos. Sci.*, vol. 50, no. 9, pp. 1305–1322.

Minnis, Patrick; Heck, Patrick W.; Young, David F.; Fairall, C. W.; and Snider, J. B. 1992: Stratocumulus Cloud Properties Derived From Simultaneous Satellite and Island-Based Instrumentation During FIRE. *J. Appl. Meteorol.*, vol. 31, pp. 317–339.

Minnis, Patrick; Liou, Kuo-Nan; and Takano, Yoshihide 1993: Inference of Cirrus Cloud Properties Using Satellite-Observed Visible and Infrared Radiances. I—Parameterization of Radiance Fields. *J. Atmos. Sci.*, vol. 50, no. 9, pp. 1279–1304.

Minnis, Patrick; Young, David F.; Heck, Patrick W.; Liou, Kuo-Nan; and Takano, Yoshihide 1992: Satellite Analyses of Cirrus Cloud Properties During the Fire Phase-II Cirrus Intensive Field Observations Over Kansas. *Proceedings of the 11th International Conference on Clouds and Precipitation*, Int. Comm. on Clouds and Precip., Int. Assoc. of Meteorol. and Atmos. Phys., pp. 480–483.

Rossow, William B.; and Garder, Leonid C. 1993: Cloud Detection Using Satellite Measurements of Invisible and Visible Radiances for ISCCP. *J. Climat.*, vol. 6, no. 12, pp. 2341–2369.

Rossow, William B.; and Schiffer, Robert A. 1991: ISCCP Cloud Data Products. *Bull. Am. Meteorol. Soc.*, vol. 72, no. 1, pp. 2–20.

Rossow, William B.; Walker, Alison W.; and Garder, Leonid C. 1993: Comparison of ISCCP and Other Cloud Amounts. *J. Climat.*, vol. 6, no. 12, pp. 2394–2418.

Schneider, J. M.; Lamb, P. J.; and Sisterson, D. L. 1993: *Site Scientific Mission Plan for the Southern Great Plains CART Site, January–June 1994*. ARM-94-001.

Smith, G. Louis; Green, Richard N.; Raschke, Ehrhard; Avis, Lee M.; Suttles, John T.; Wielicki, Bruce A.; and Davies, Roger 1986: Inversion Methods for Satellite Studies of the Earth's Radiation Budget: Development of Algorithms for the ERBE Mission. *Rev. Geophys.*, vol. 24, no. 2, pp. 407–421.

Smith, William L., Jr.; Minnis, Patrick; Alvarex, Joseph M.; Uttal, Tanell; Interieri, Janet M.; Ackerman, Thomas P.; and Clothiaux, Eugene 1993: Development of Methods for Inferring Cloud Thickness and Cloud-Base Height From Satellite Radiance Data. *The Fire Cirrus Science Results 1993*, David S. McDougal, ed., NSF, NOAA, DOE, and ONR, pp. 32–35.

Stokes, Gerald M.; and Schwartz, Stephen E. 1994: The Atmospheric Radiation Measurement (ARM) Program: Programmatic Background and Design of the Cloud and Radiation Test Bed. *Bull. Am. Meteorol. Soc.*, vol. 75, no. 7, pp. 1201–1221.

Suttles, J. T.; Green, R. N.; Minnis, P.; Smith, G. L.; Staylor, W. F.; Wielicki, B. A.; Walker, I. J.; Young, D. F.; Taylor, V. R.; and Stowe, L. L. 1988: *Angular Radiation Models for Earth-Atmosphere System. Volume I—Shortwave Radiation.* NASA RP-1184, Vol. I.

Suttles, J. T.; Green, R. N.; Smith, G. L.; Wielicki, B. A.; Walker, I. J.; Taylor, V. R.; and Stowe, L. L. 1989: *Angular Radiation Models for Earth-Atmosphere System. Volume II—Longwave Radiation.* NASA RP-1184, Vol. II.

Takano, Yoshihide; and Liou, Kuo-Nan 1989: Solar Radiative Transfer in Cirrus Clouds. I—Single-Scattering and Optical Properties of Hexagonal Ice Crystals. II—Theory and Computations of Multiple Scattering in an Anisotropic Medium. *J. Atmos. Sci.*, vol. 46, pp. 3–36.

Whitlock, Charles H.; LeCroy, S. R.; and Wheeler, R. J. 1994: SRB/FIRE Satellite Calibration Results and Their Impact on ISCCP. *Proceedings of the Eighth Conference on Atmospheric Radiation Satellite Meteorology and Oceanography*, AMS, pp. 52–54.

Wielicki, Bruce A.; and Green, Richard N. 1989: Cloud Indentification for ERBE Radiative Flux Retrieval. *J. Appl. Meteorol.*, vol. 28, no. 11, pp. 1133–1146.

Wielicki, Bruce A.; and Parker, Lindsay 1992: On the Determination of Cloud Cover From Satellite Sensors—The Effect of Sensor Spatial Resolution. *J. Geophys. Res.*, vol. 97, no. D12, pp. 12799–12823.

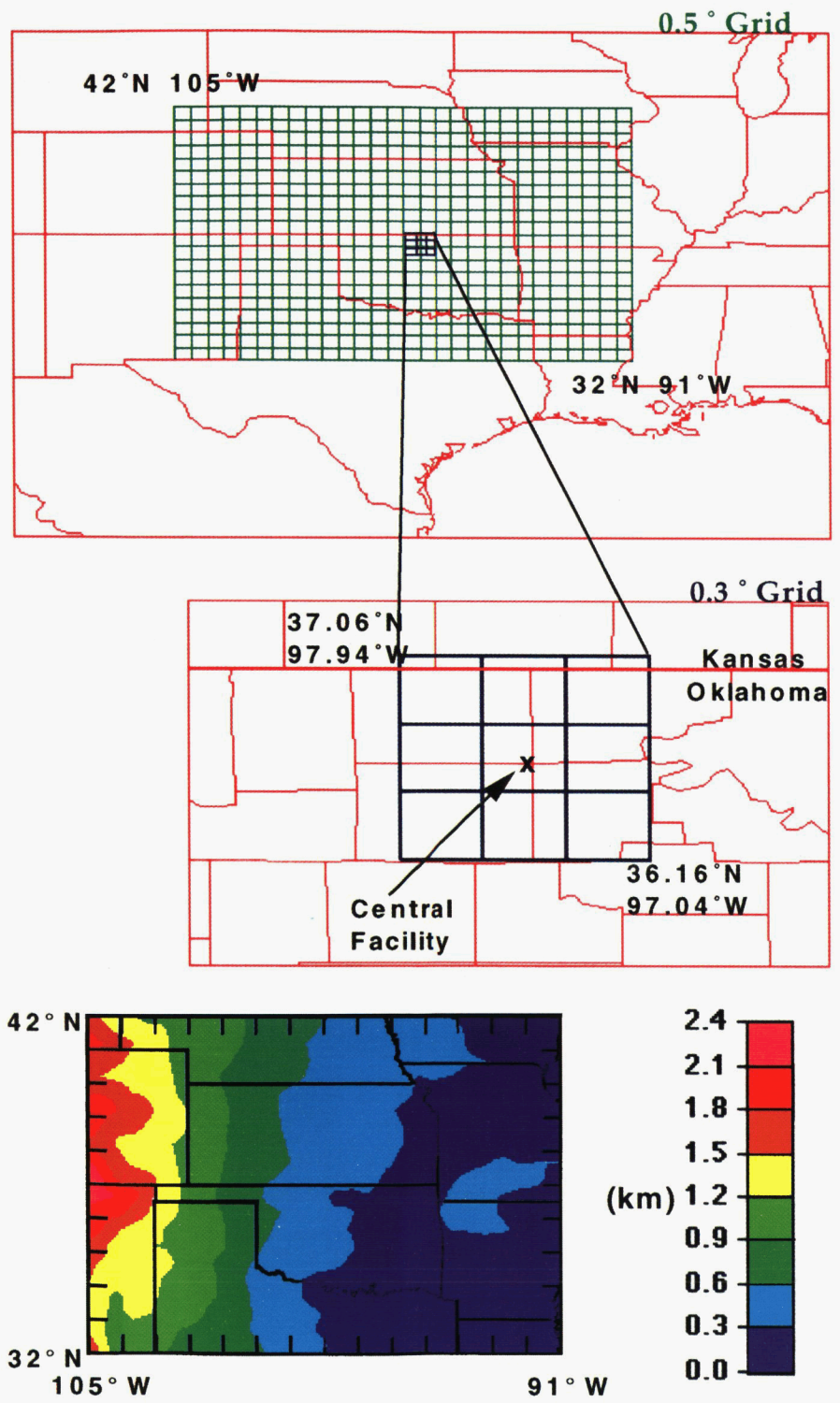

Figure 1. Satellite data analysis grids and surface elevation map for ARM Southern Great Plains locale.

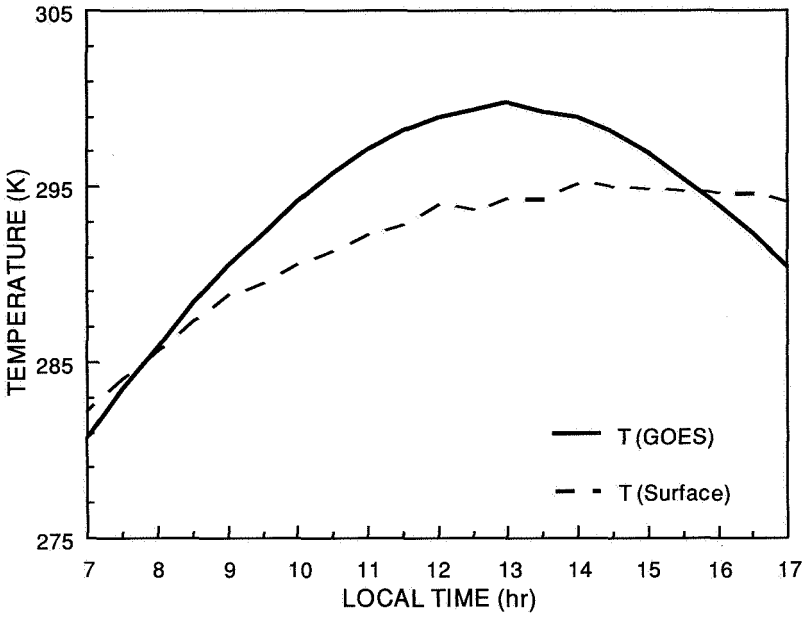

Figure 2. Mean hourly surface shelter and GOES-derived clear-sky temperatures for April 1994 over ARM SGP mesoscale domain.

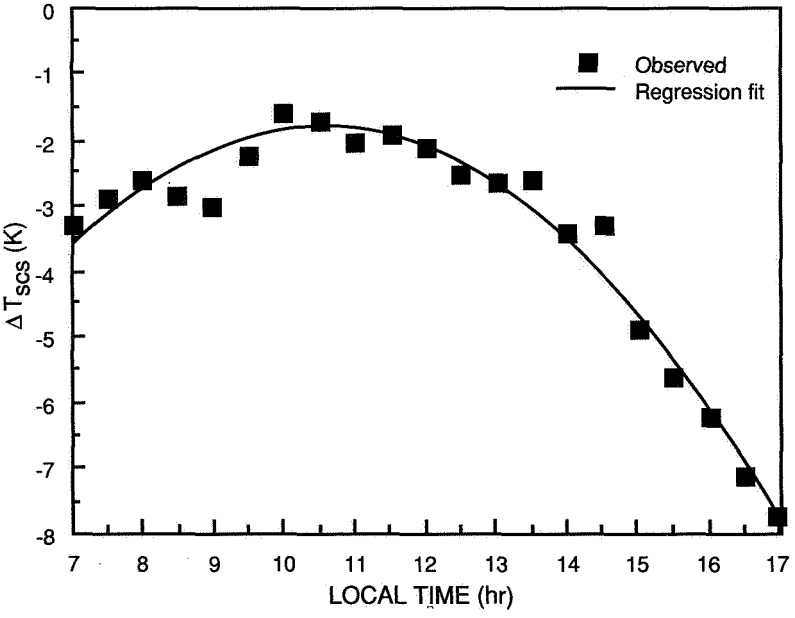

Figure 3. Observed and regression fit of ΔT_{scs} for April 1994 over ARM SGP mesoscale domain.

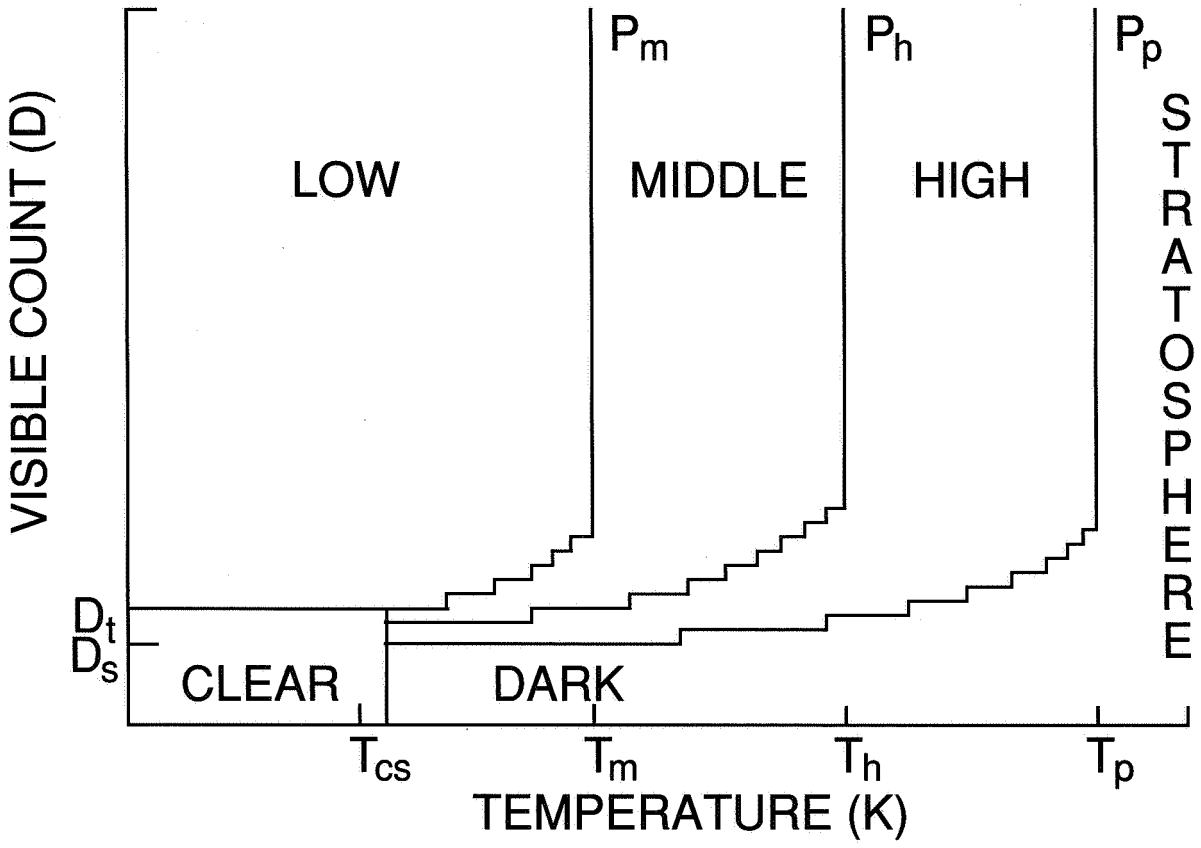

Figure 4. VIS-IR boundaries for clear and cloud-layer classifications in LBTM.

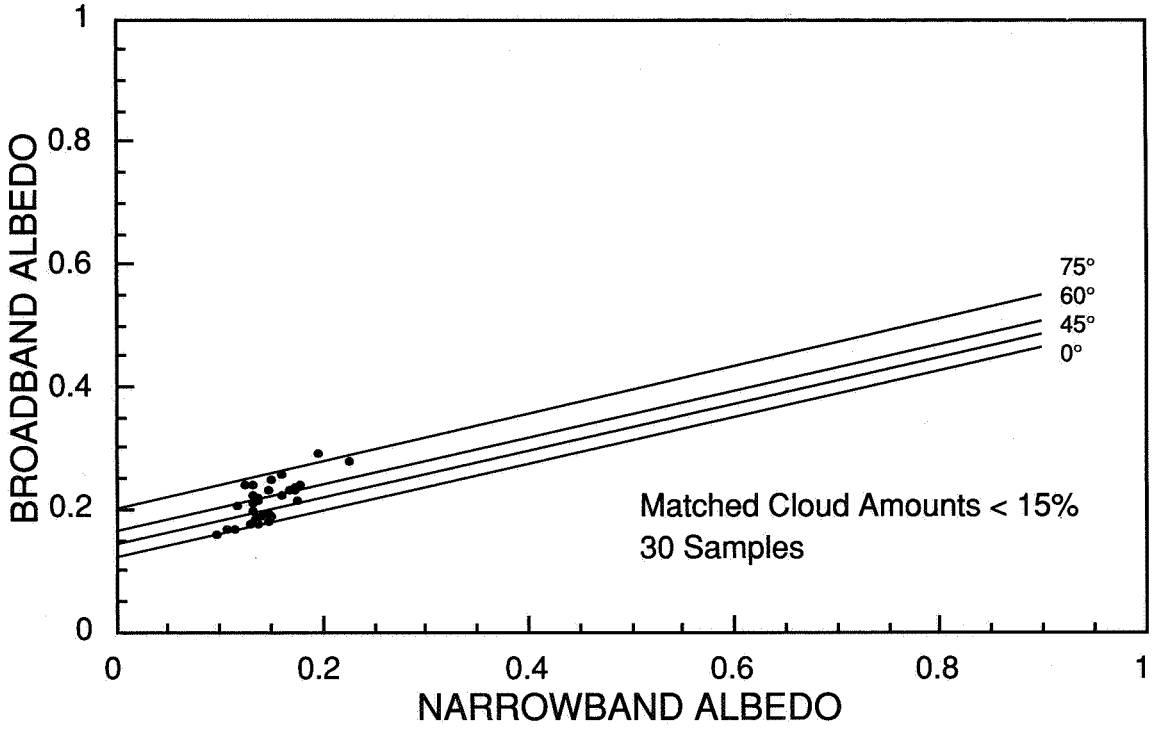

(a) Clear-sky data.

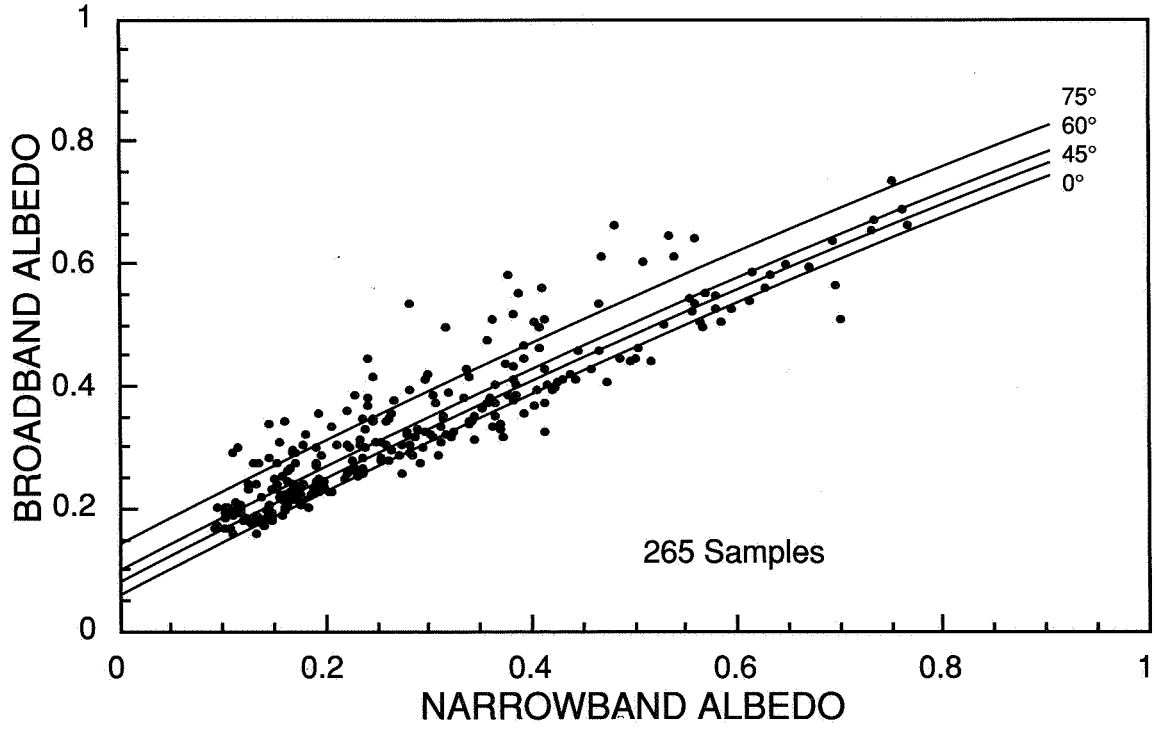

(b) All data.

Figure 5. Correlations of ERBS SW and GOES VIS albedos for April 1985; curves indicate regression fits at particular solar zenith angles.

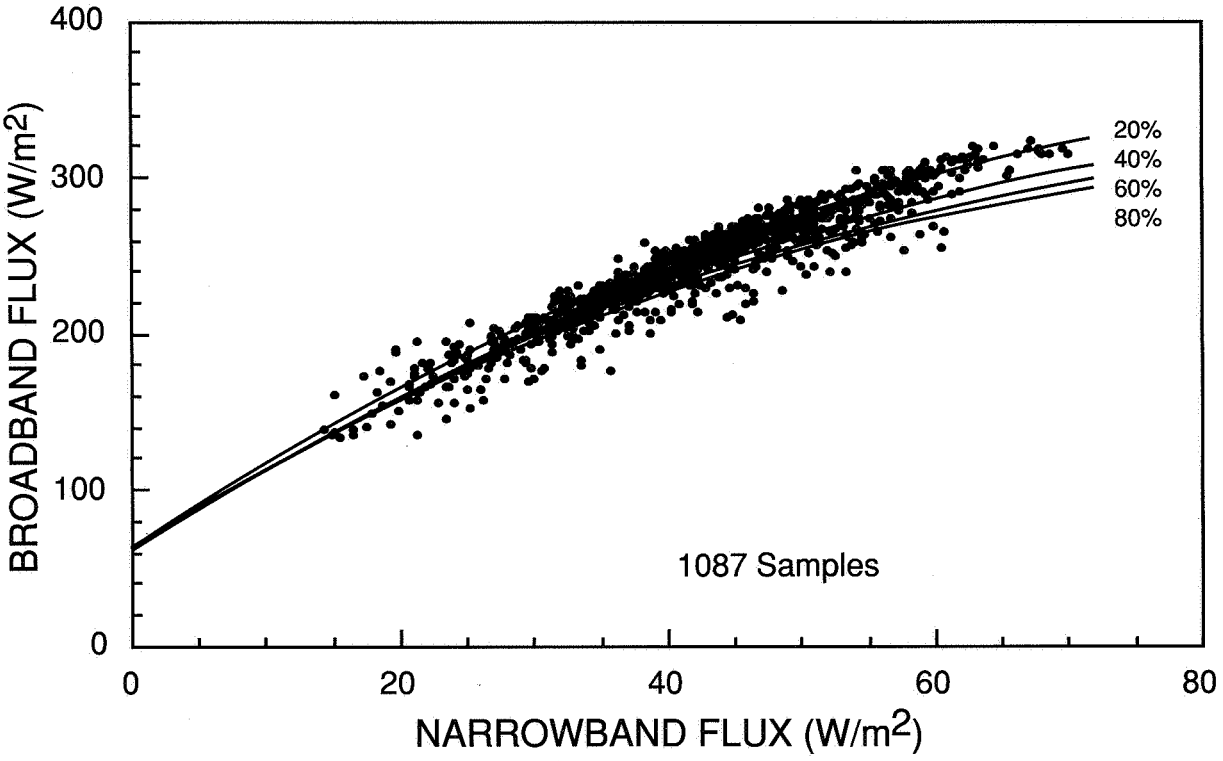

Figure 6. Correlations of ERBS LW and GOES IR fluxes for April 1985; curves indicate regression fits at particular relative humidities.

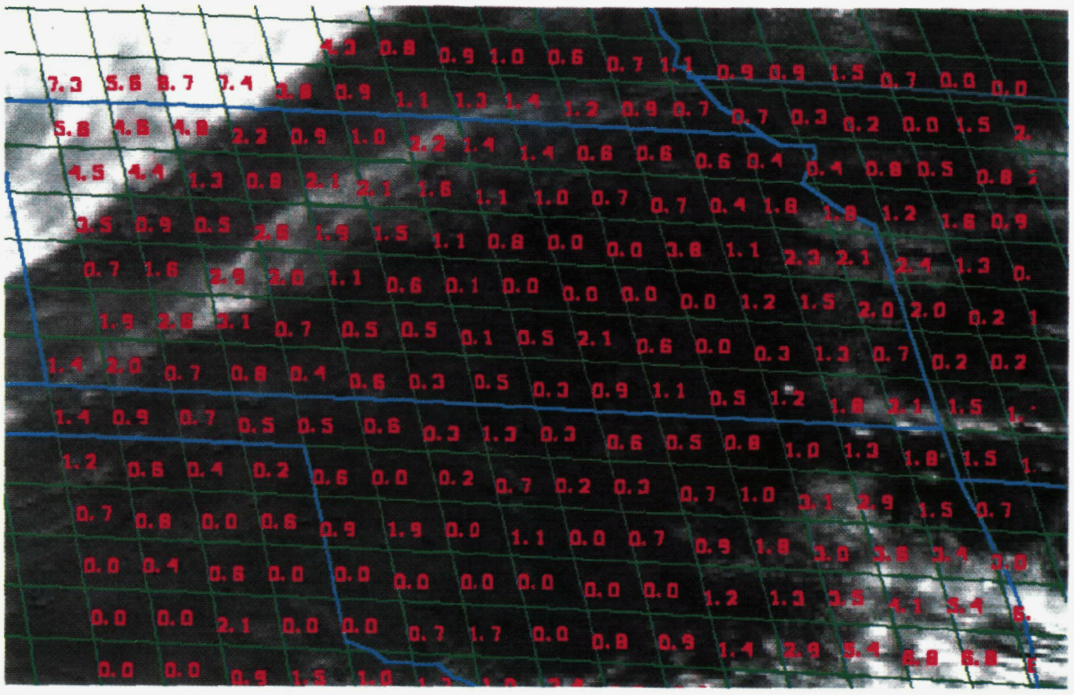

Figure 7. Cloud optical depths overlaid on GOES VIS image for 1930 UTC, April 14, 1994.

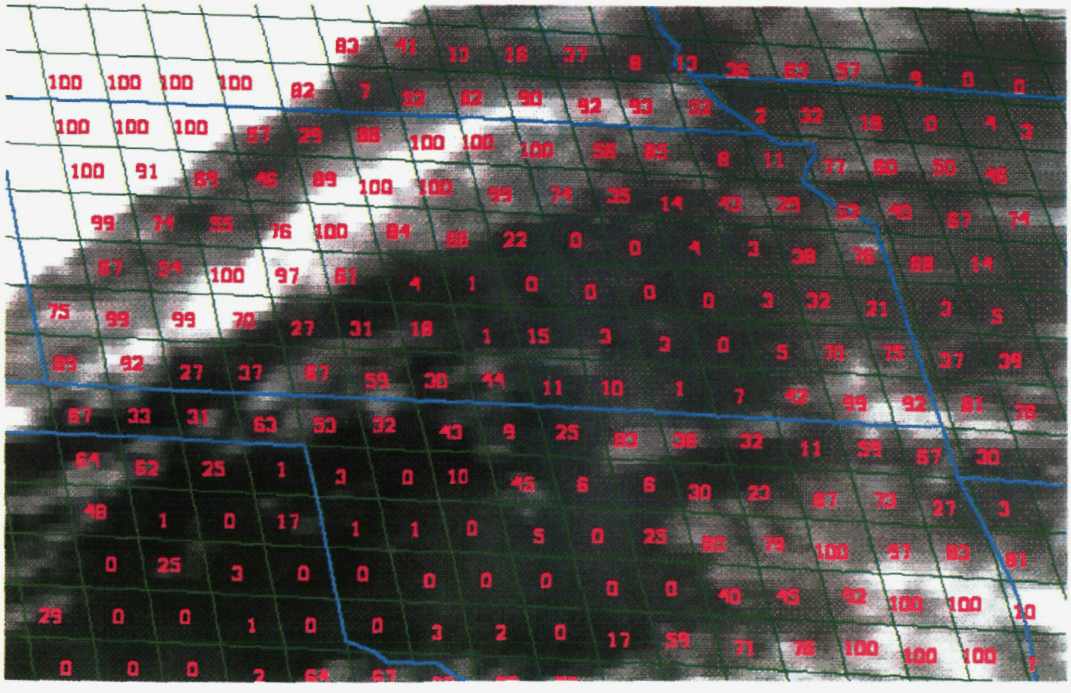

Figure 8. Total cloud amounts overlaid on GOES IR image for 1930 UTC, April 14, 1994.

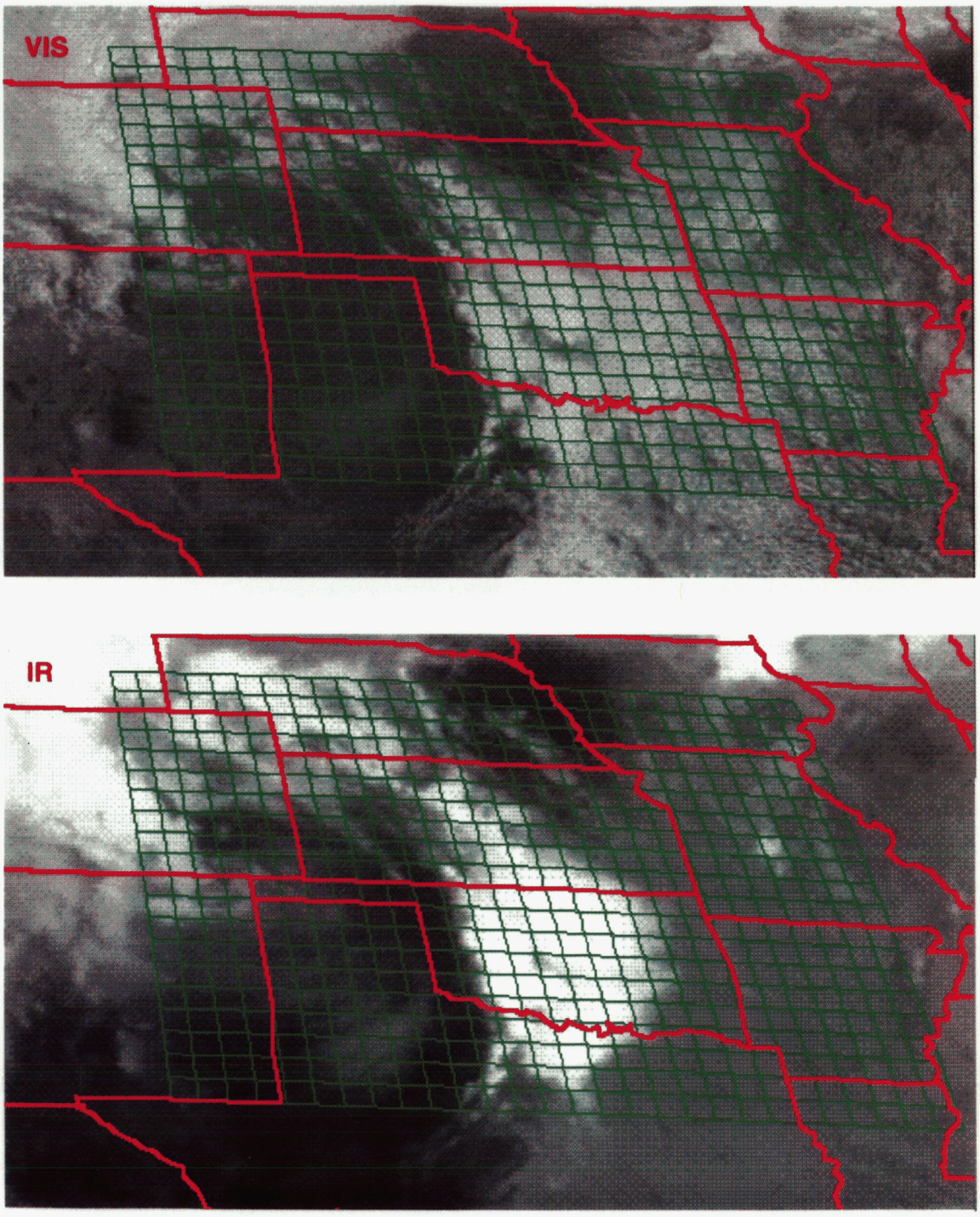

Figure 9. GOES VIS and IR images overlaid with ARM SGP mesoscale domain for 1800 UTC, April 25, 1994.

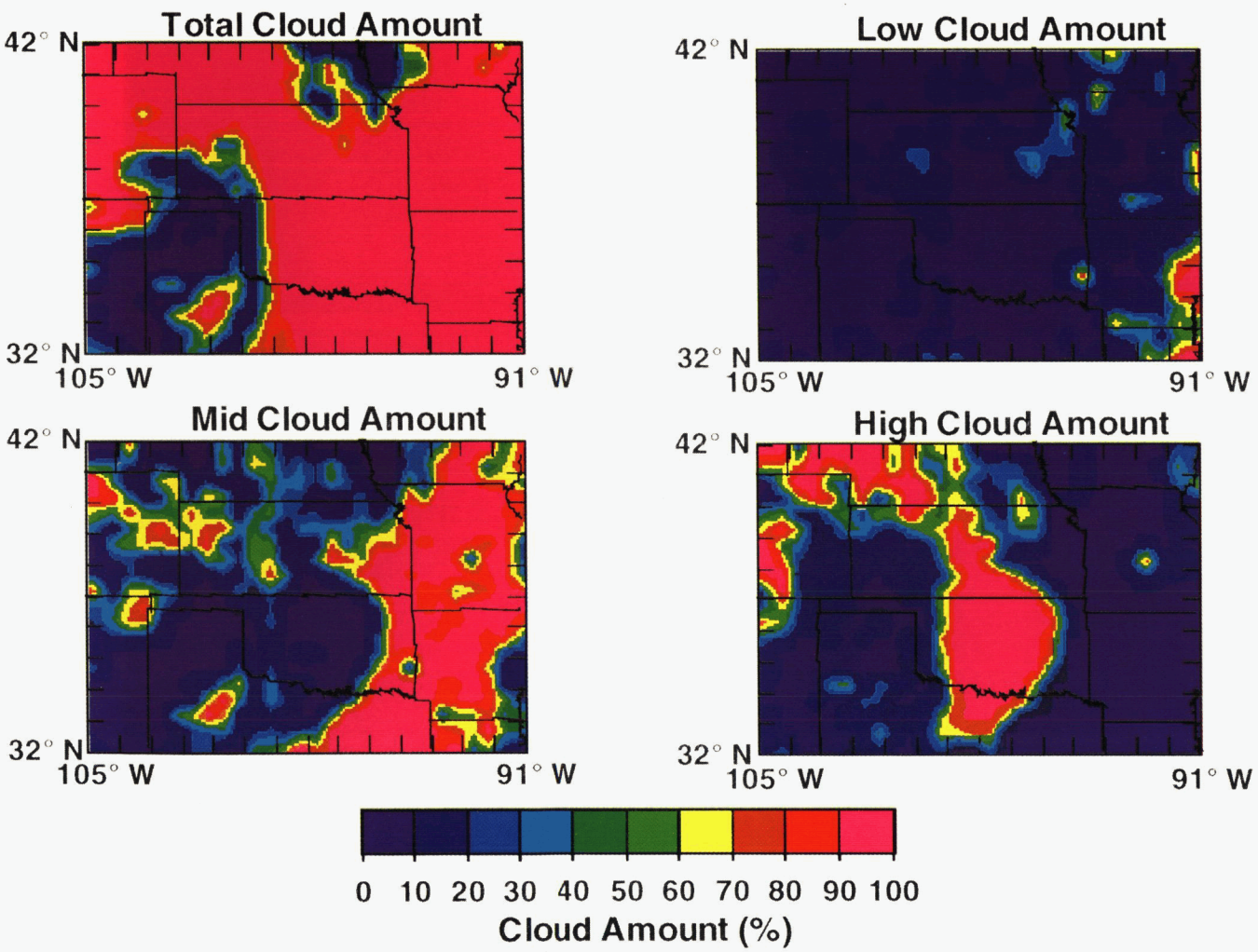

Figure 10. Cloud amounts for 1800 UTC, April 25, 1994.

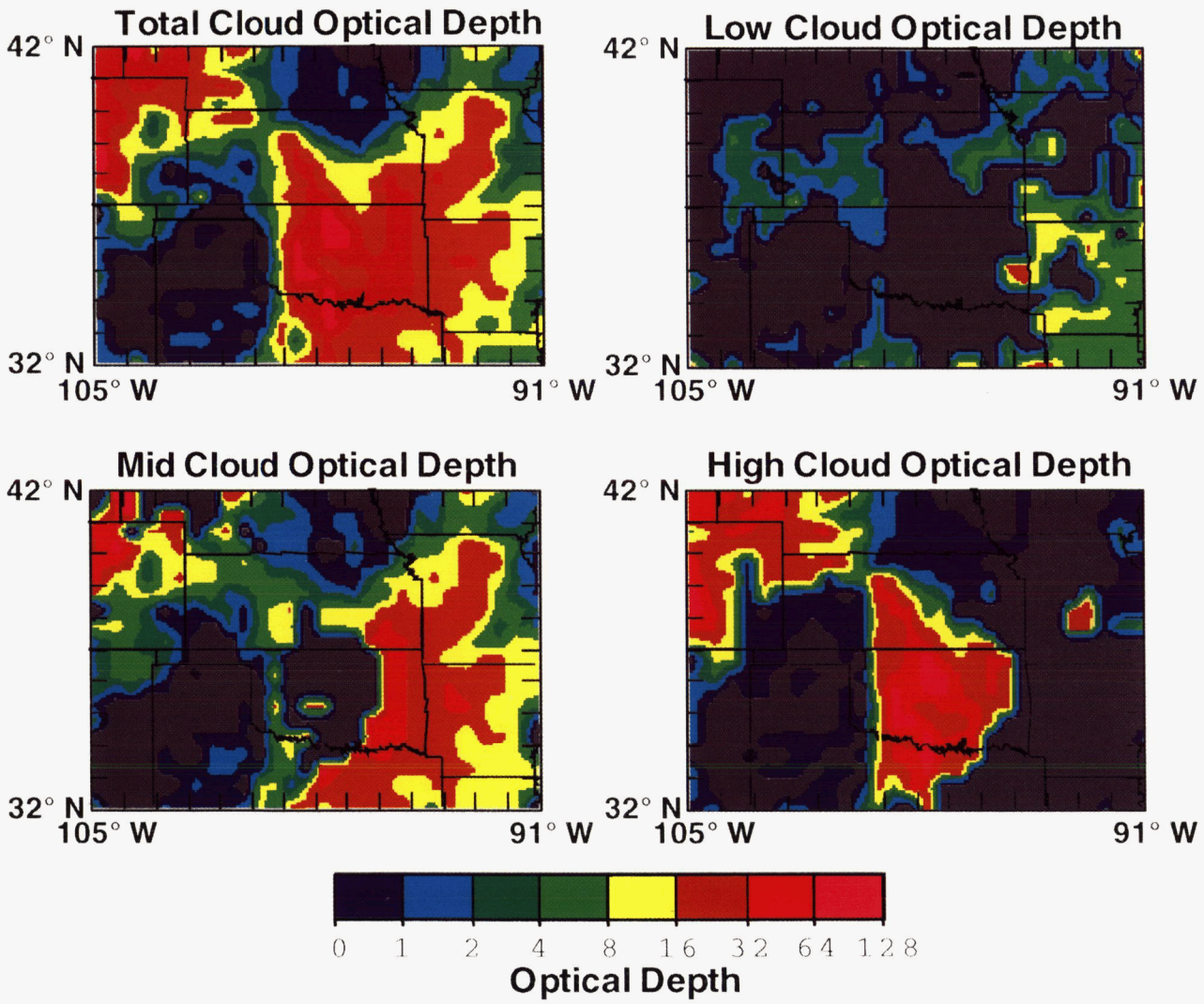

Figure 11. Cloud optical depths for 1800 UTC, April 25, 1994.

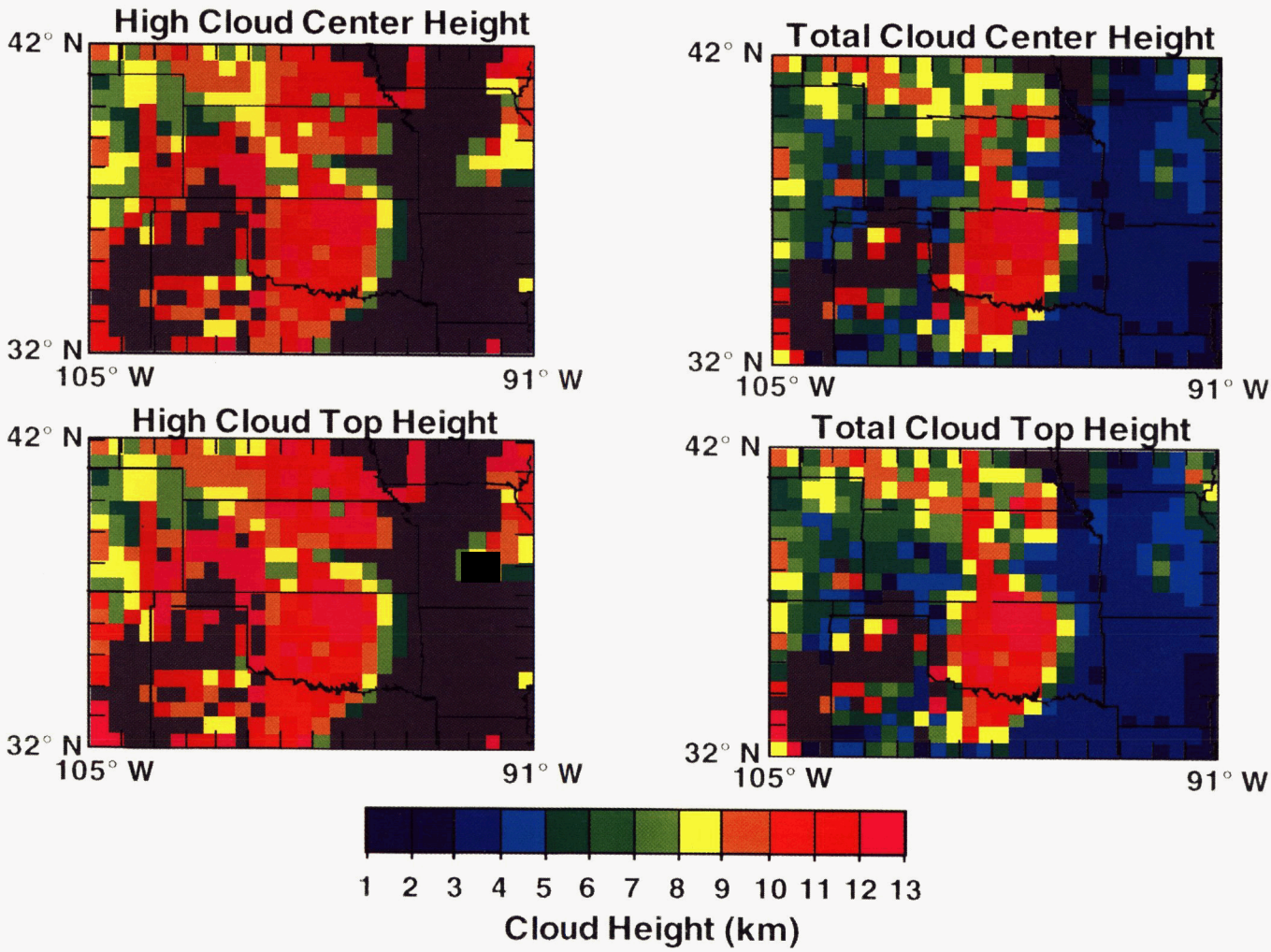

Figure 12. High and total cloud center and top heights for 1800 UTC, April 25, 1994.

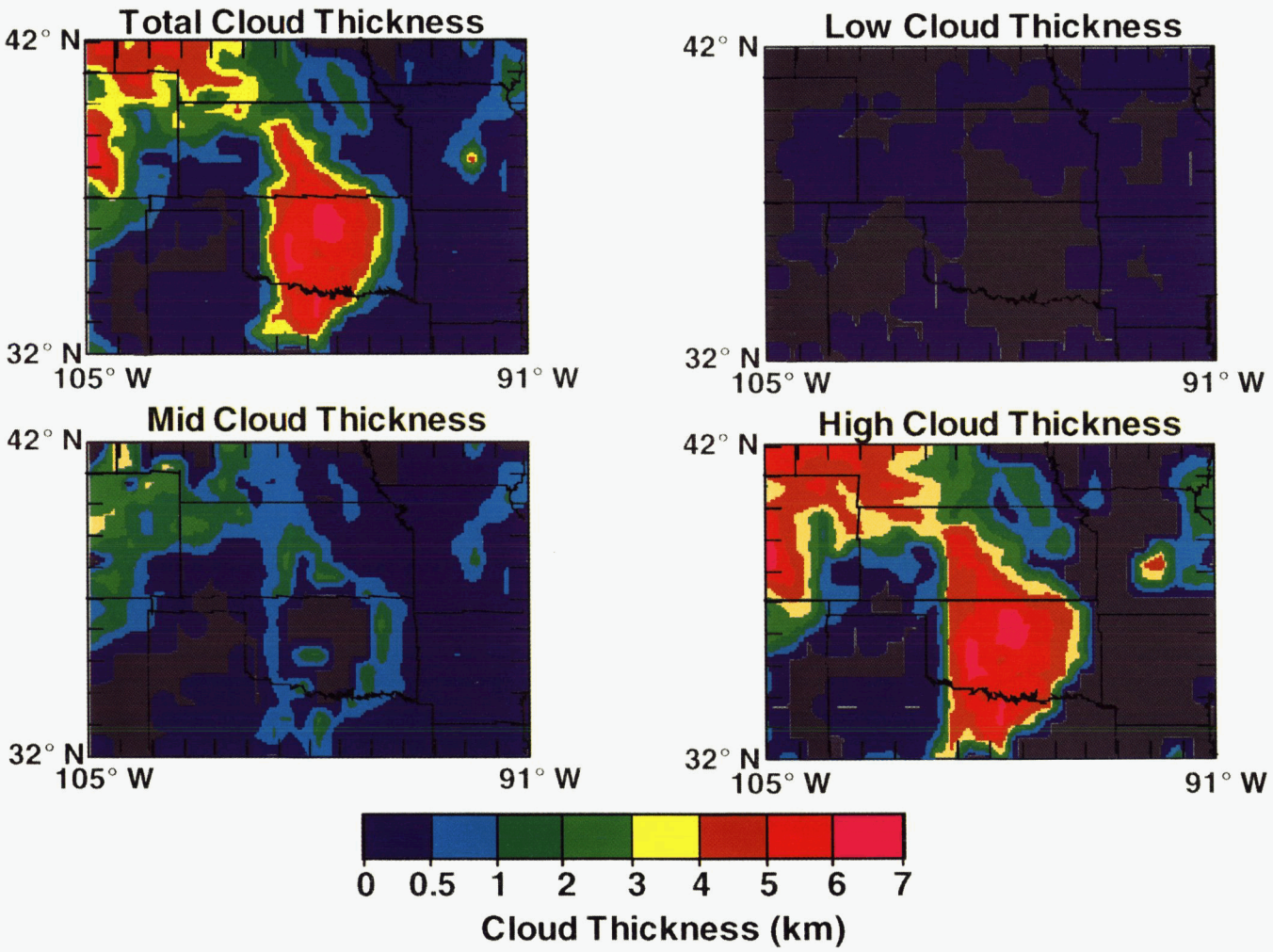

Figure 13. Cloud thickness for 1800 UTC, April 25, 1994.

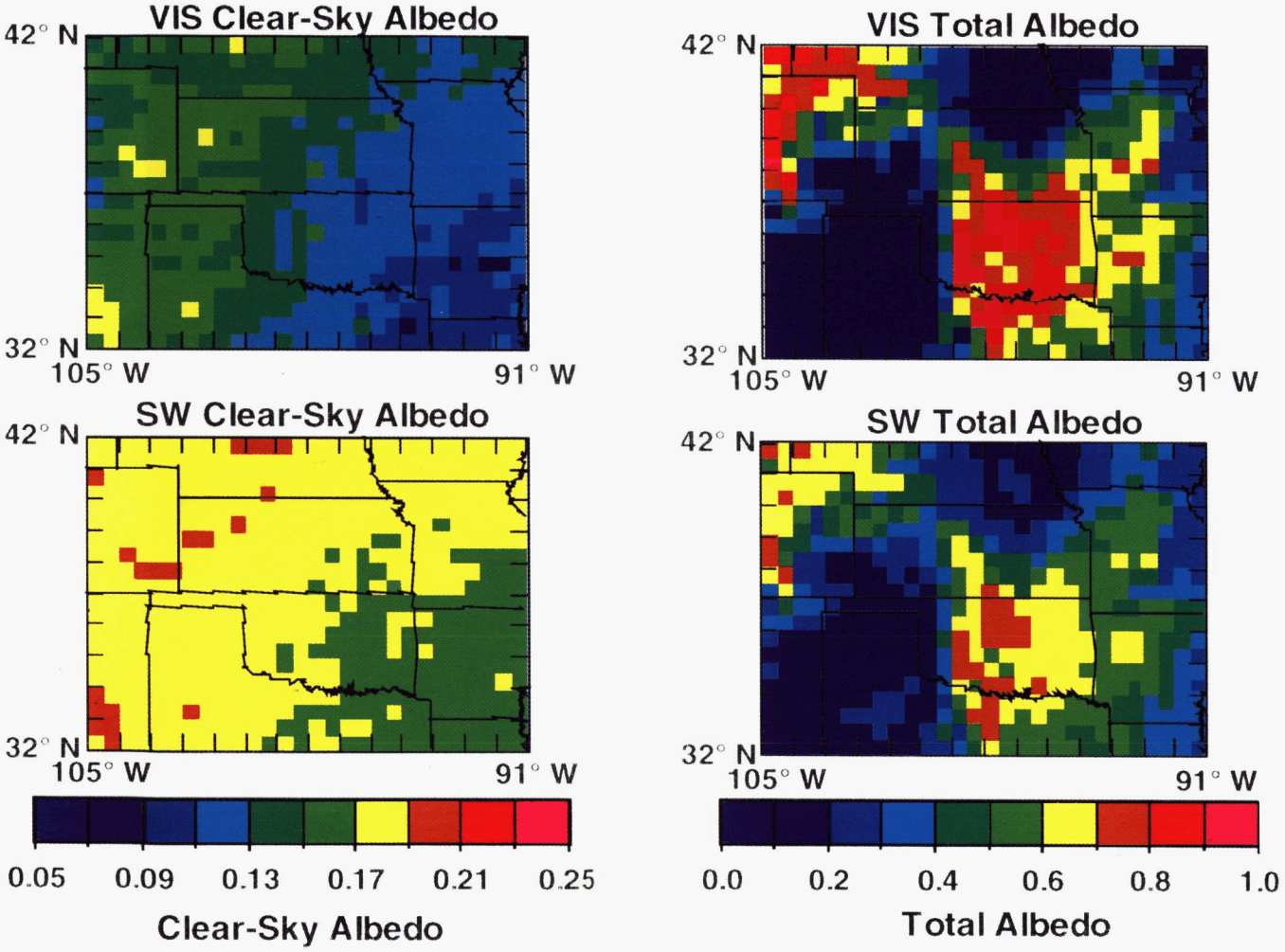

Figure 14. VIS and SW albedos for 1800 UTC, April 25, 1994.

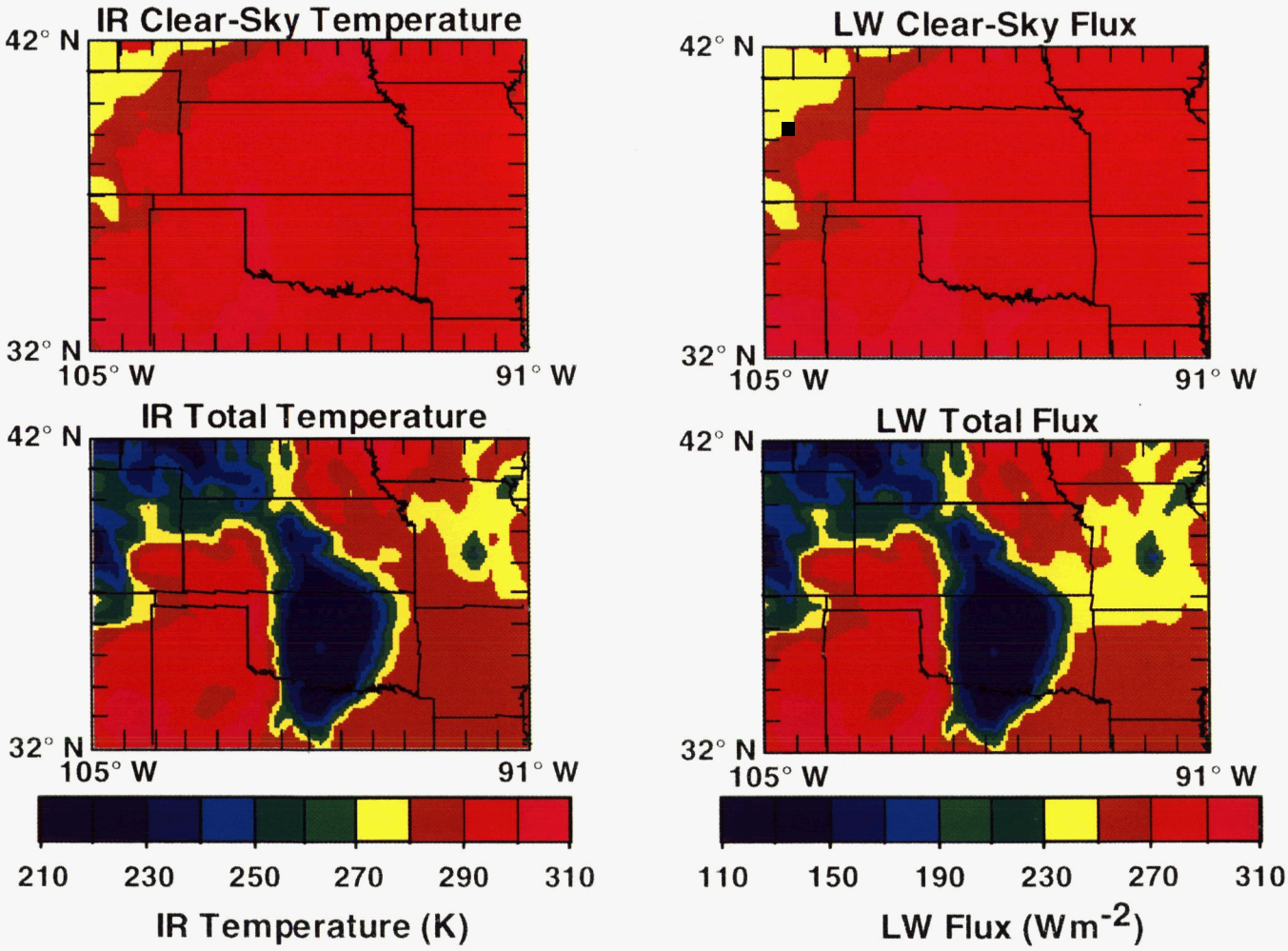

Figure 15. IR temperatures and LW fluxes for 1800 UTC, April 25, 1994.

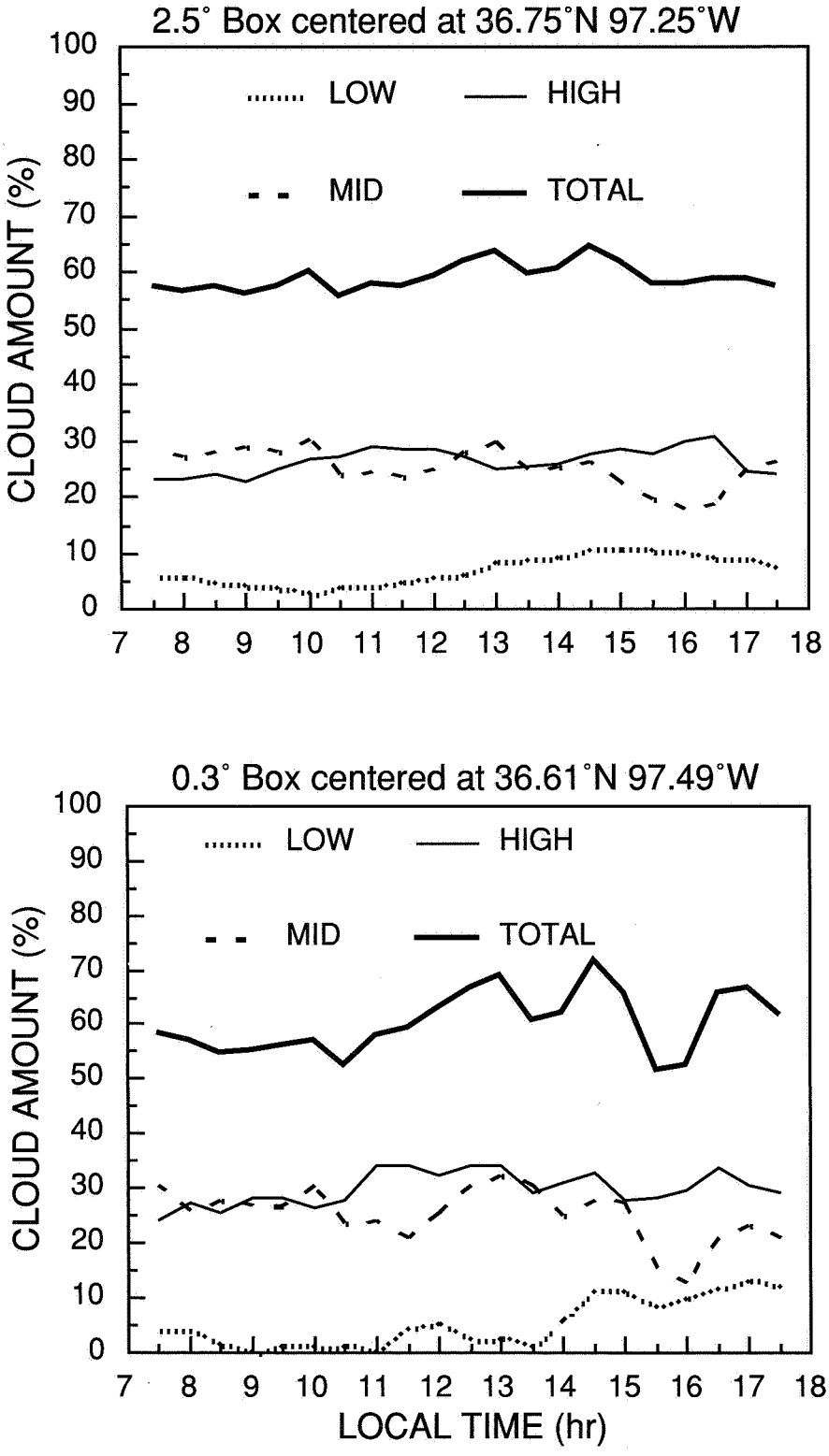

Figure 16. Mean hourly cloud amounts for 0.3° and 2.5° (average of 0.5°) regions centered on SCF for April 5 to May 1, 1994.

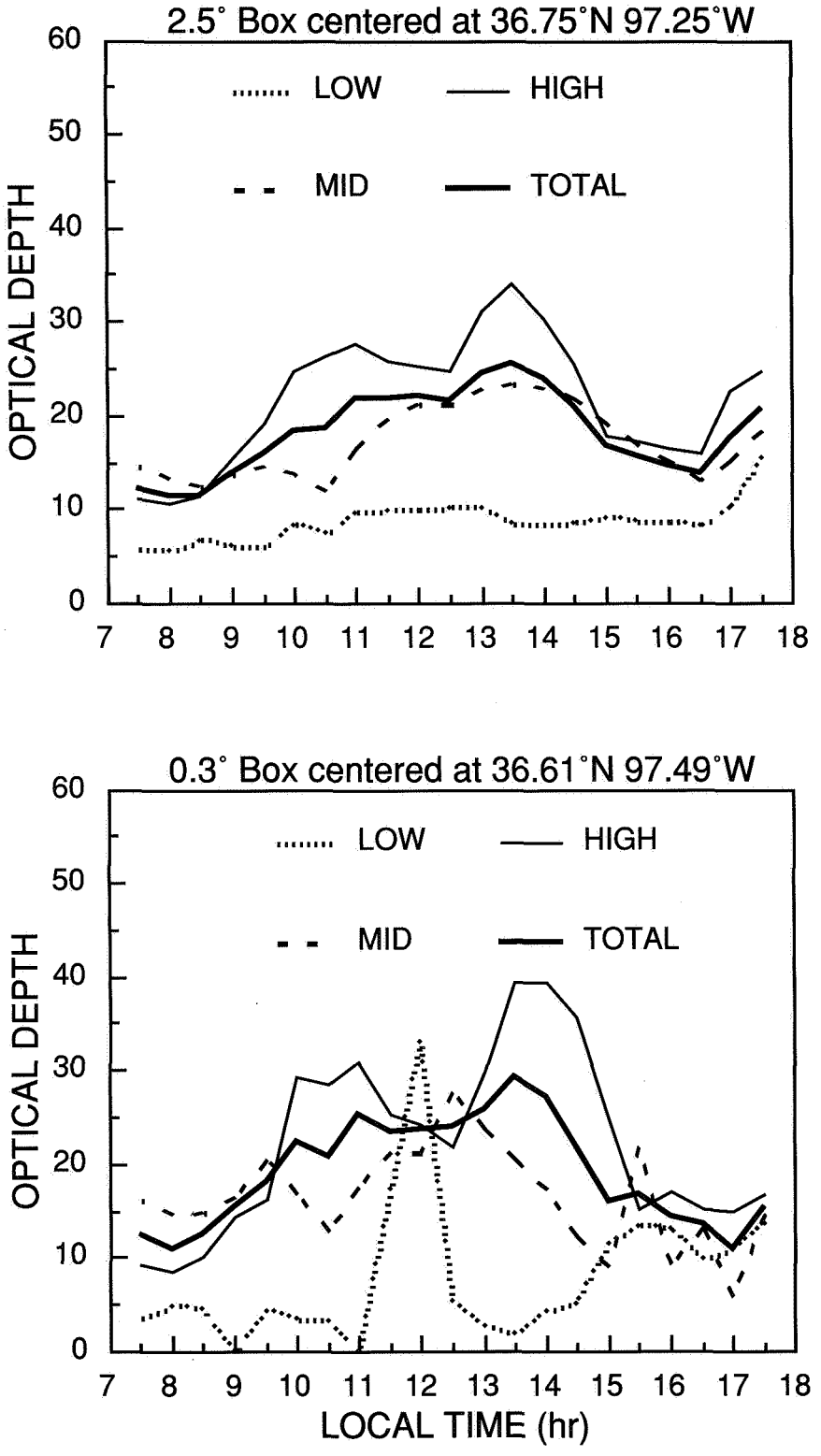

Figure 17. Optical depths for 0.3° and 2.5° (average of 0.5°) regions centered on SCF for April 5 to May 1, 1994.

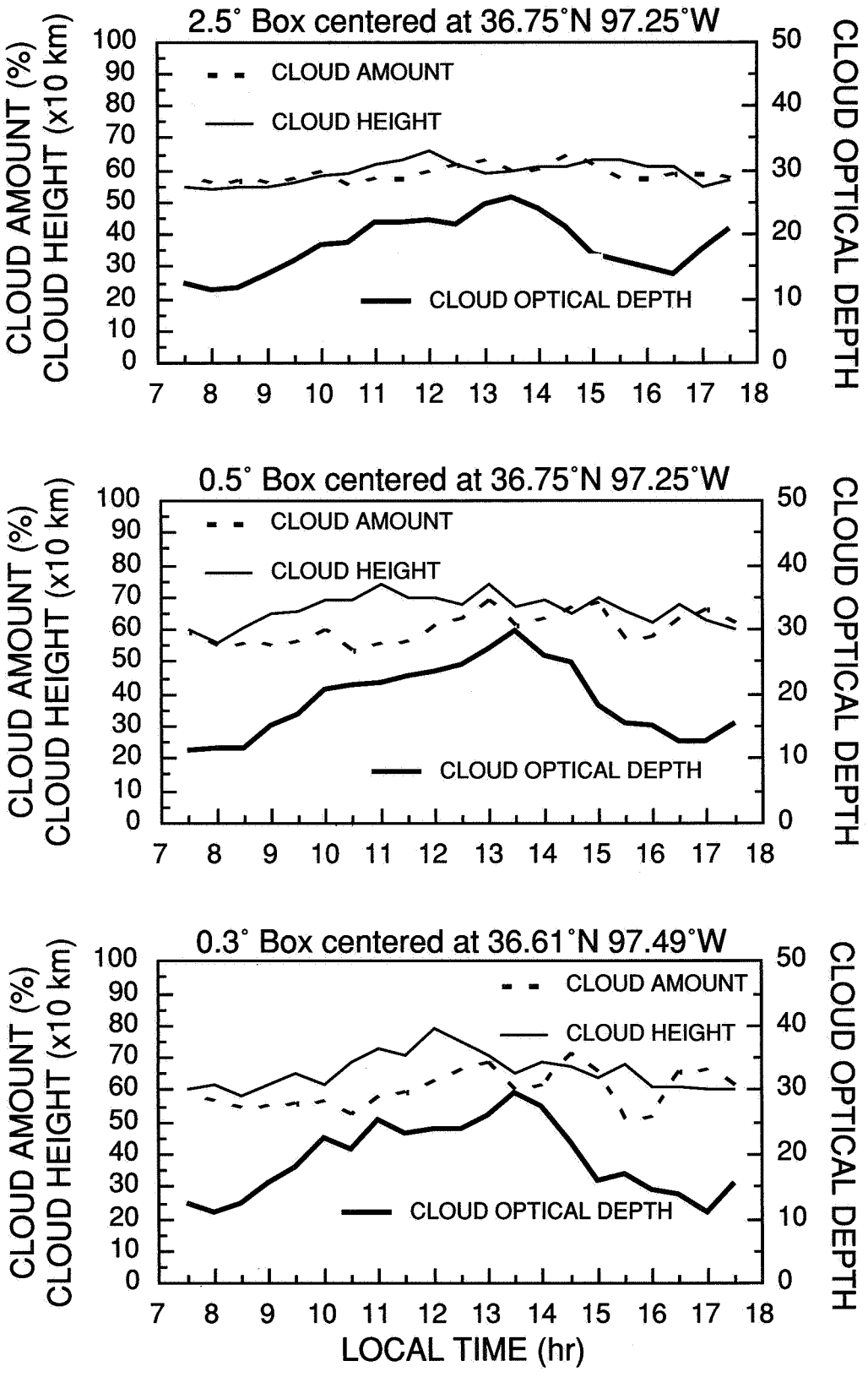

Figure 18. Mean half-hourly cloud amounts, optical depths, and heights for 0.3°, 0.5°, and 2.5° regions centered on SCF for April 5 to May 1, 1994.

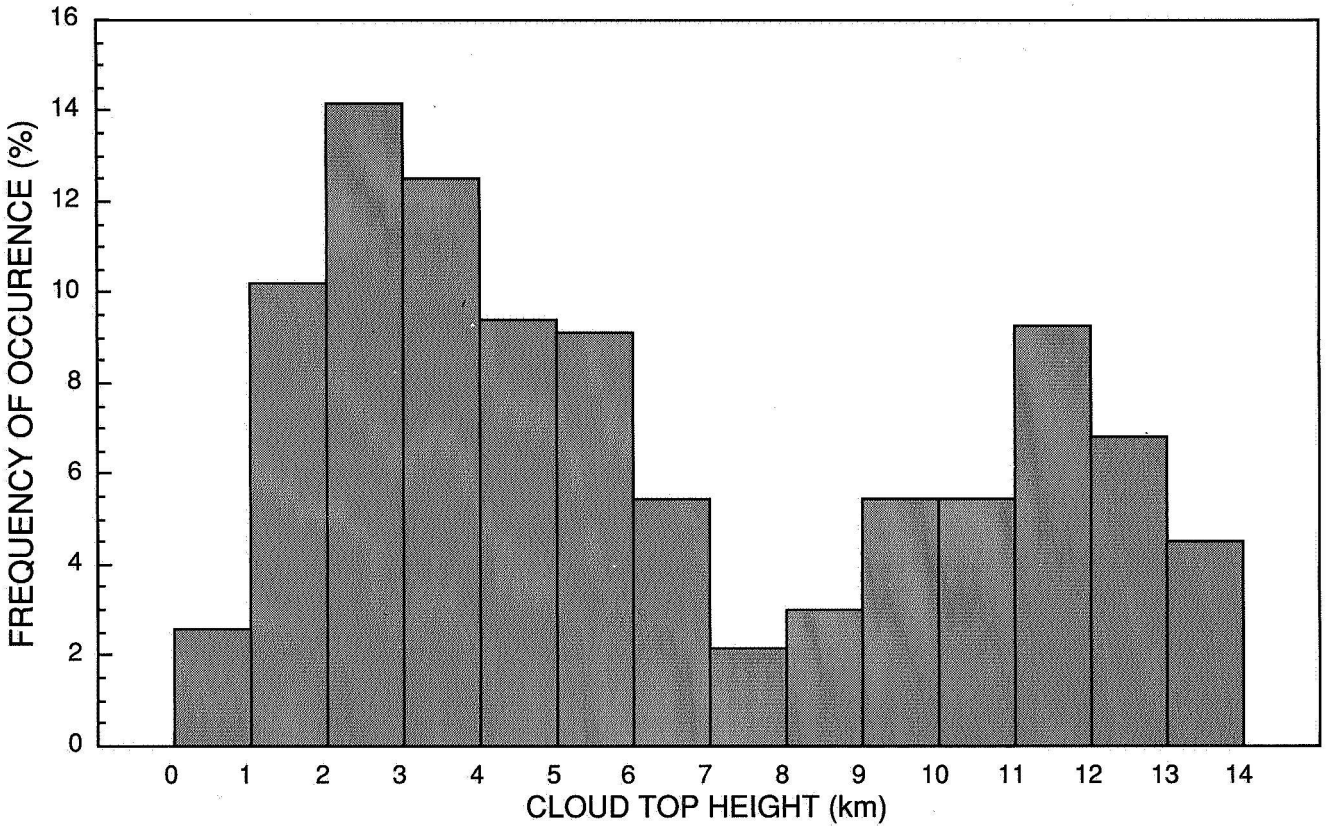

Figure 19. Frequency of cloud-top height occurrences for 0.5° region (36.75°N, 97.25°W) that includes SGP Central Facility.

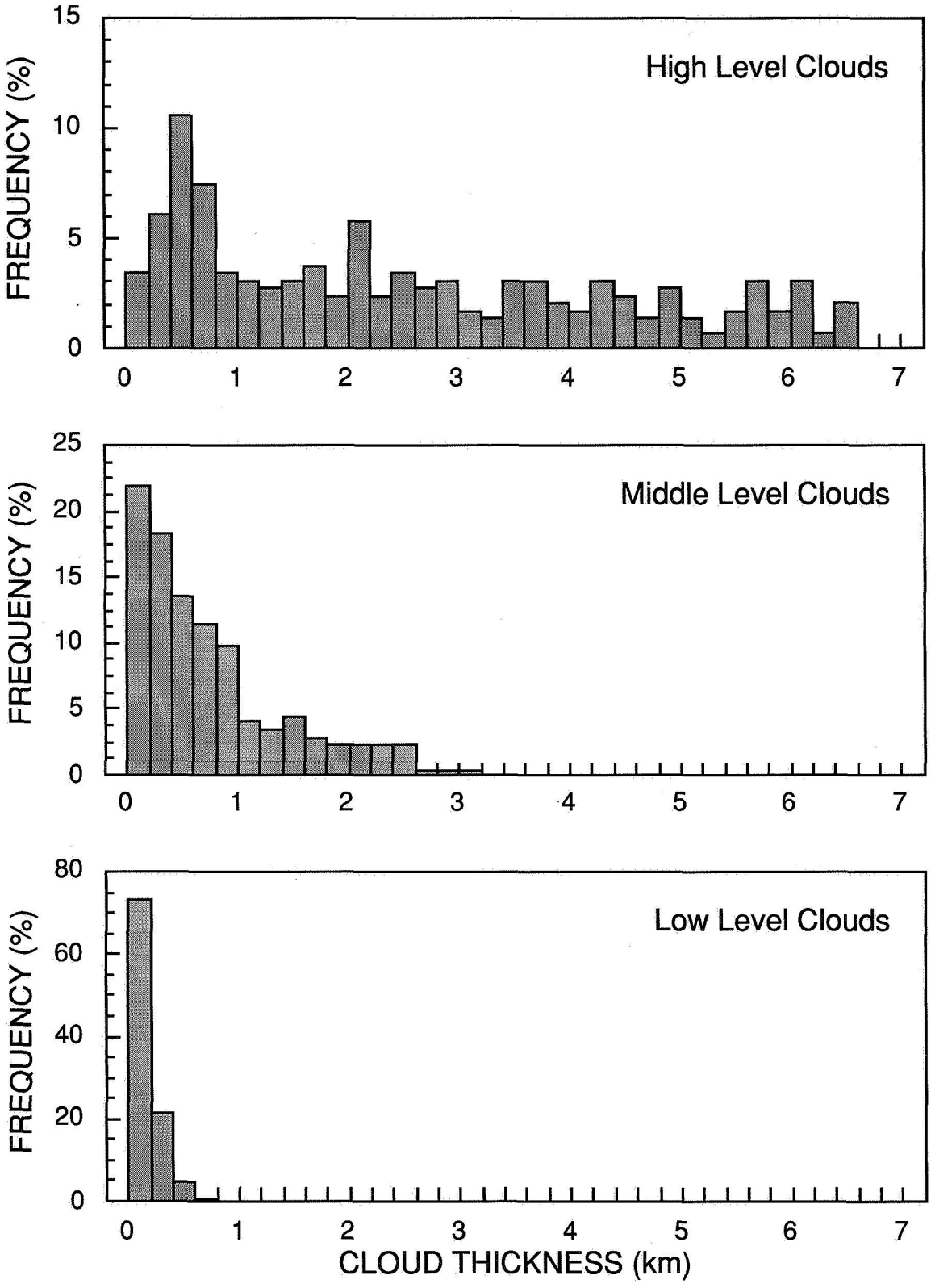

Figure 20. Layer cloud thickness for 0.5° region (36.75°N, 97.25°W) that included SGP Central Facility.

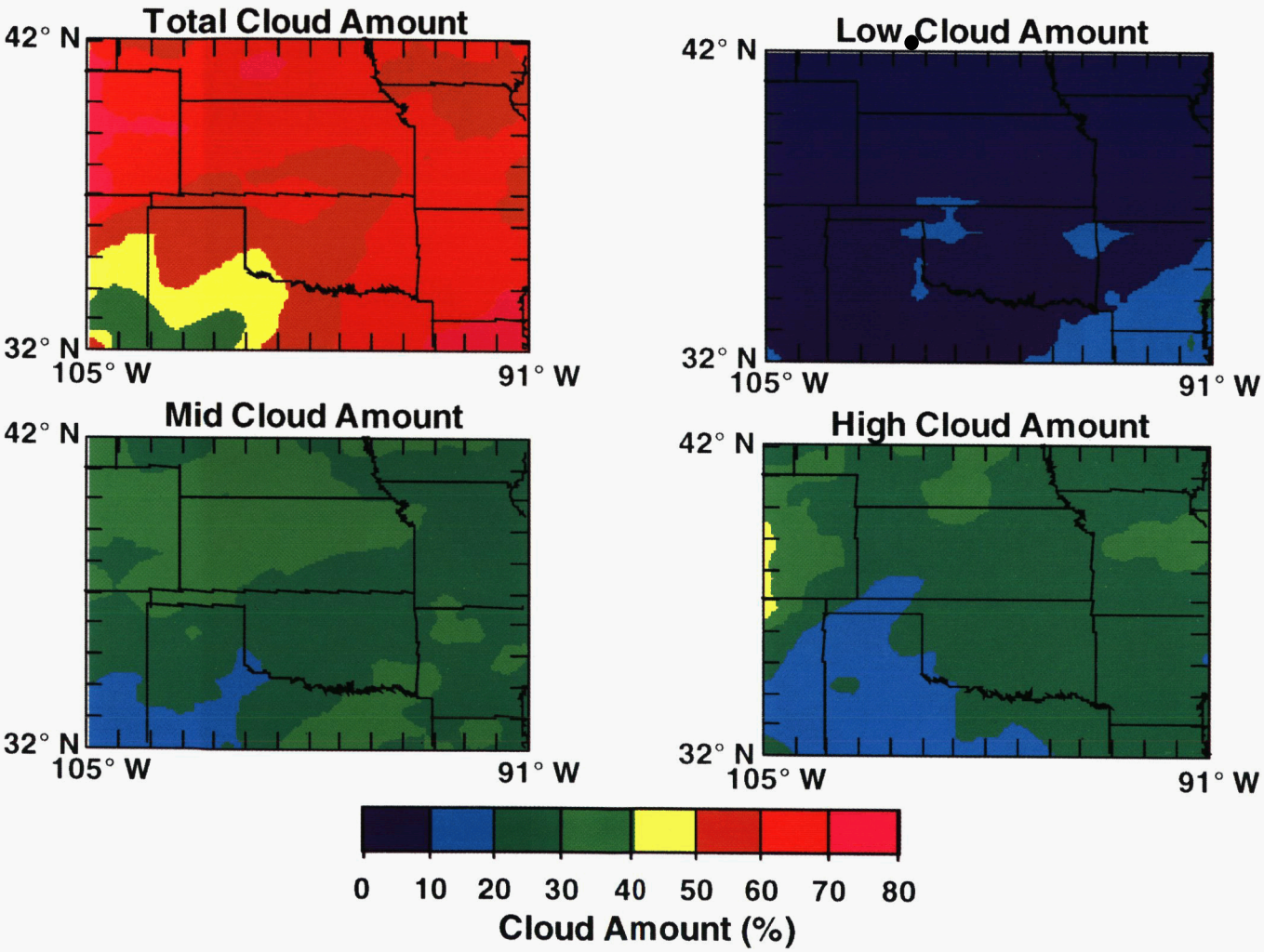

Figure 21. Mean cloud amount for 1330 to 2330 UTC for April 5 to May 1, 1994.

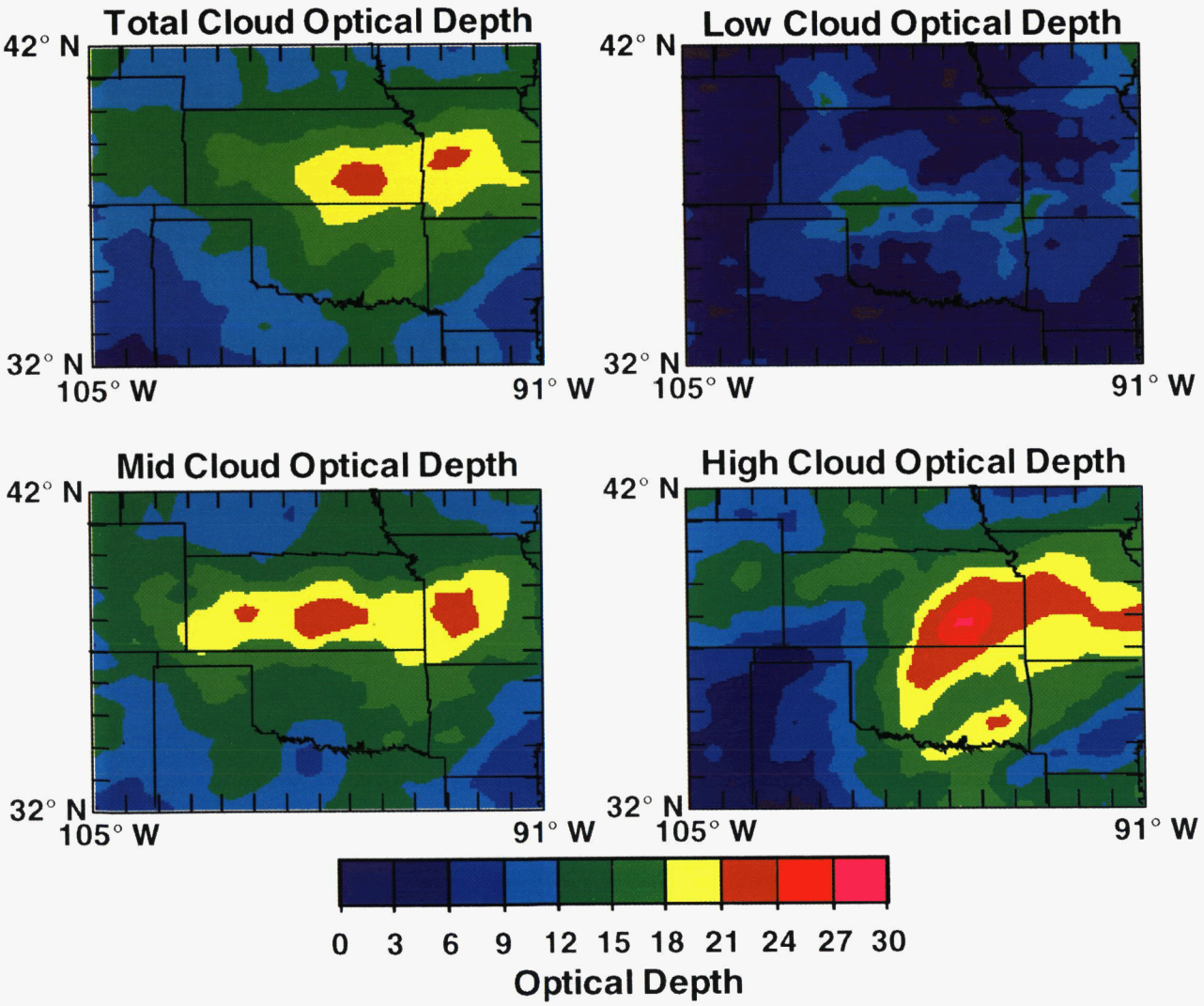

Figure 22. Mean cloud optical depths for 1330 to 2330 UTC for April 5 to May 1, 1994.

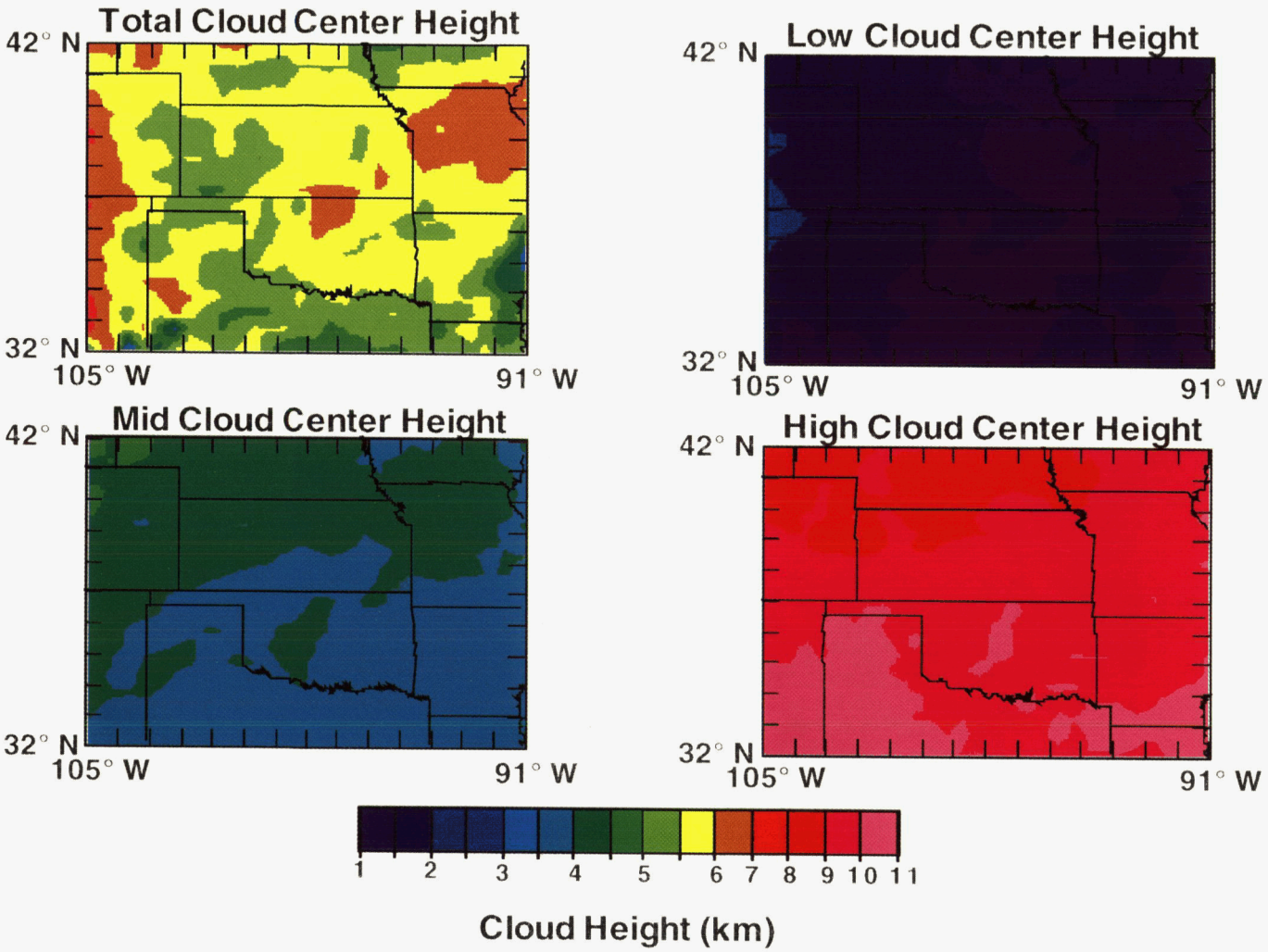

Figure 23. Mean cloud-center heights for 1330 to 2330 UTC for April 5 to May 1, 1994.

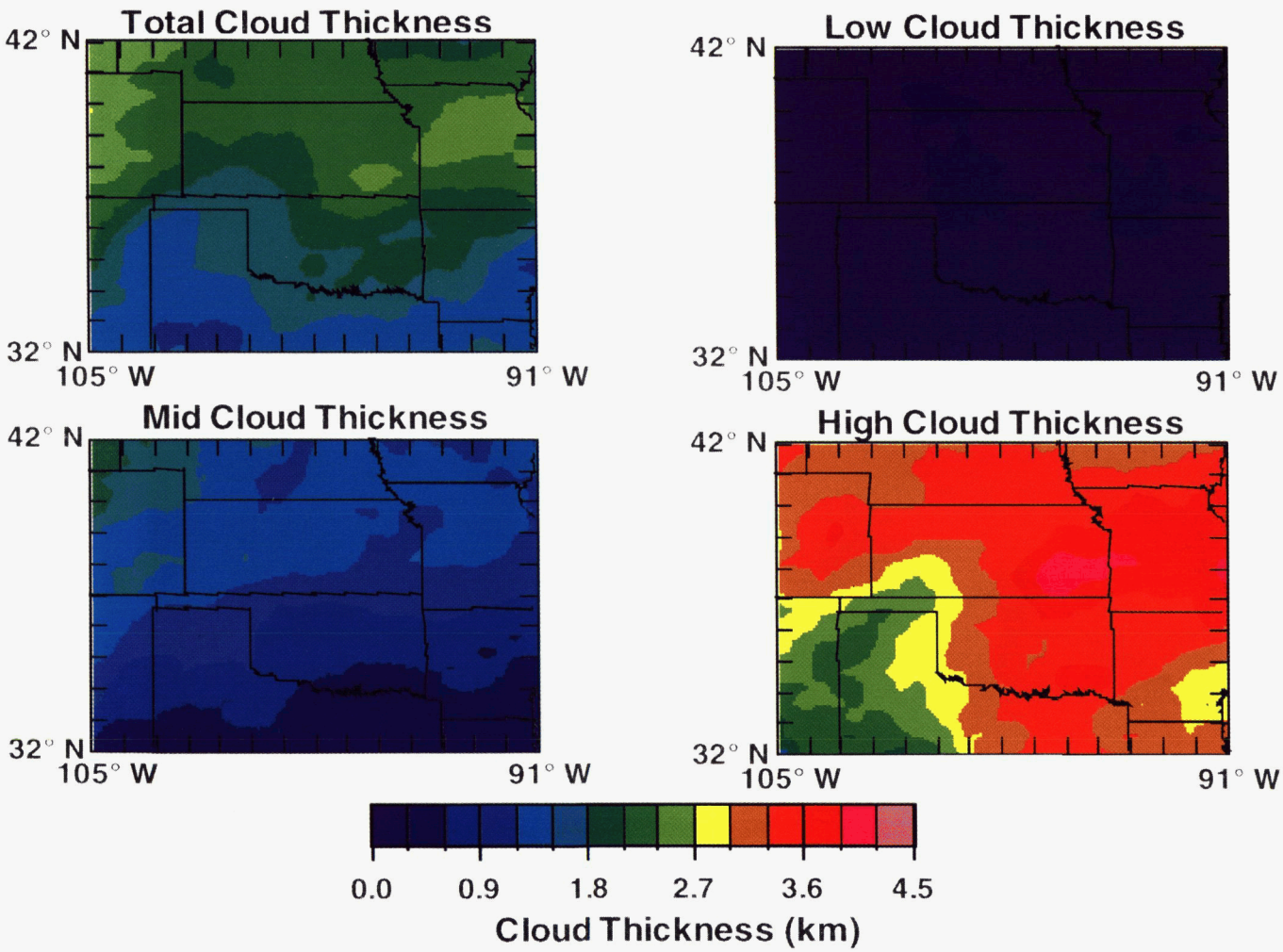

Figure 24. Mean cloud thickness for 1330 to 2330 UTC for April 5 to May 1, 1994.

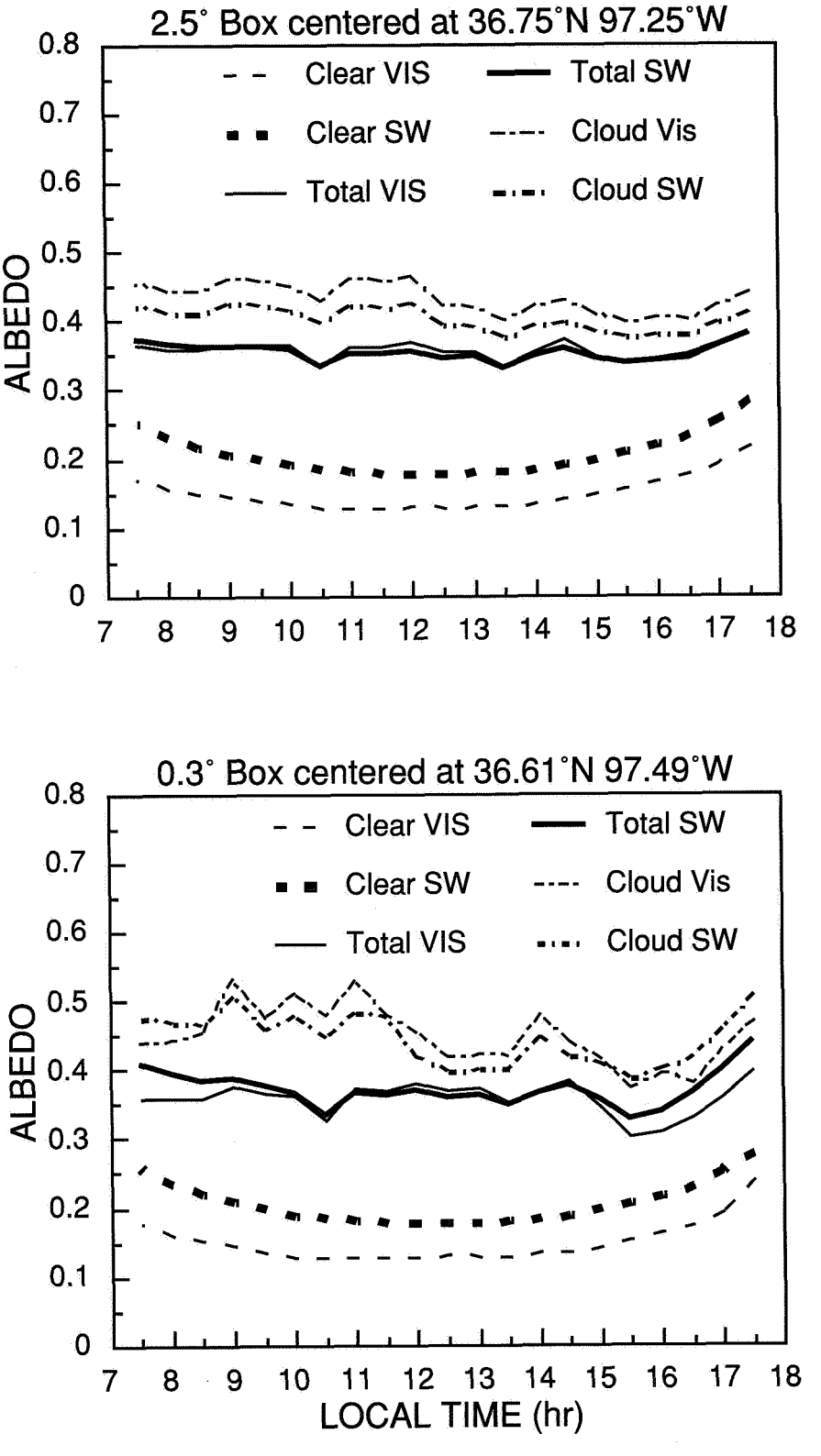

Figure 25. Mean VIS and SW albedos for 0.3° and 2.5° (average of 0.5°) regions centered on SCF for April 5 to May 1, 1994.

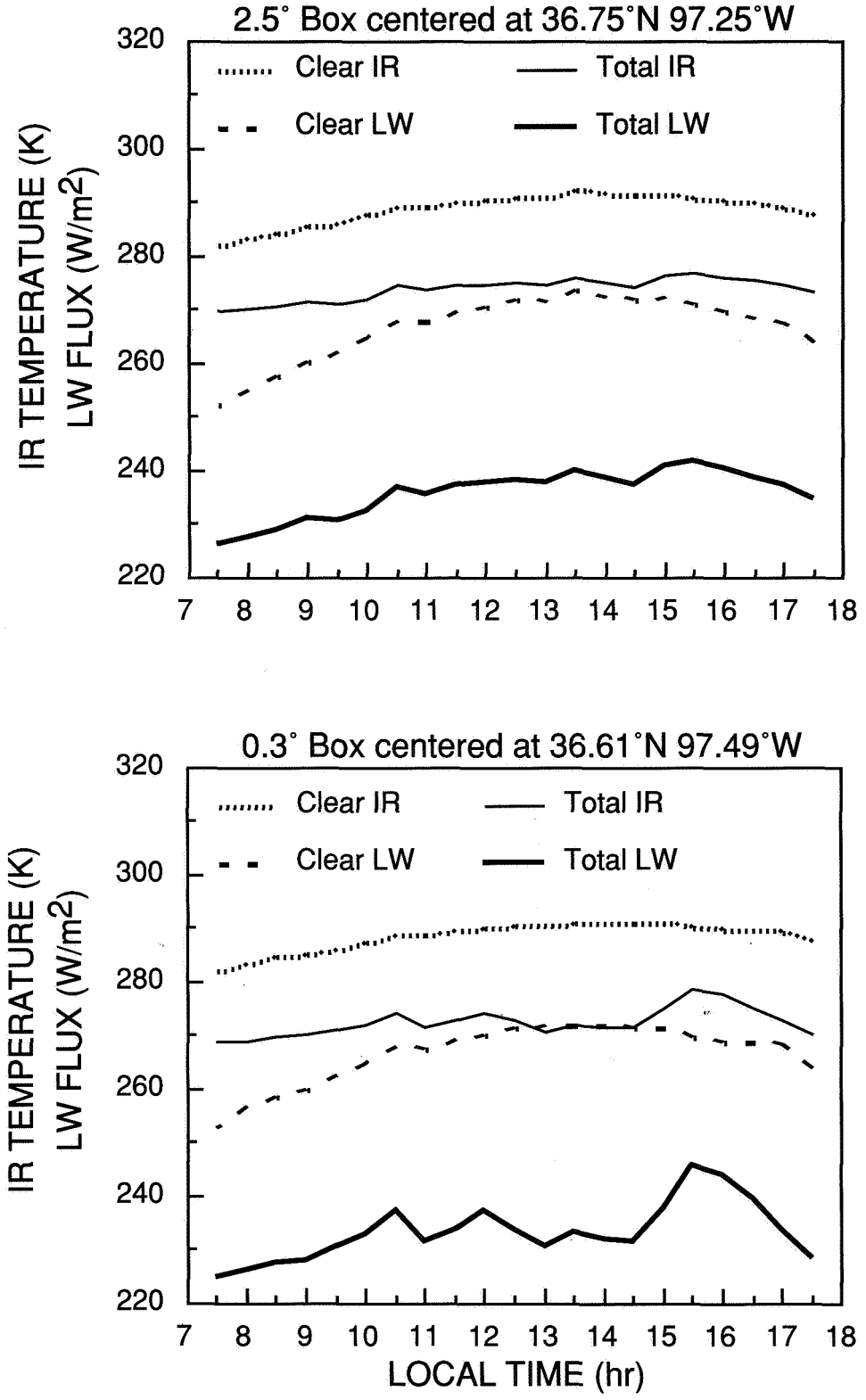

Figure 26. Mean IR temperatures and LW fluxes for 0.3° and 2.5° (average of 0.5°) regions centered on SCF for April 5 to May 1, 1994.

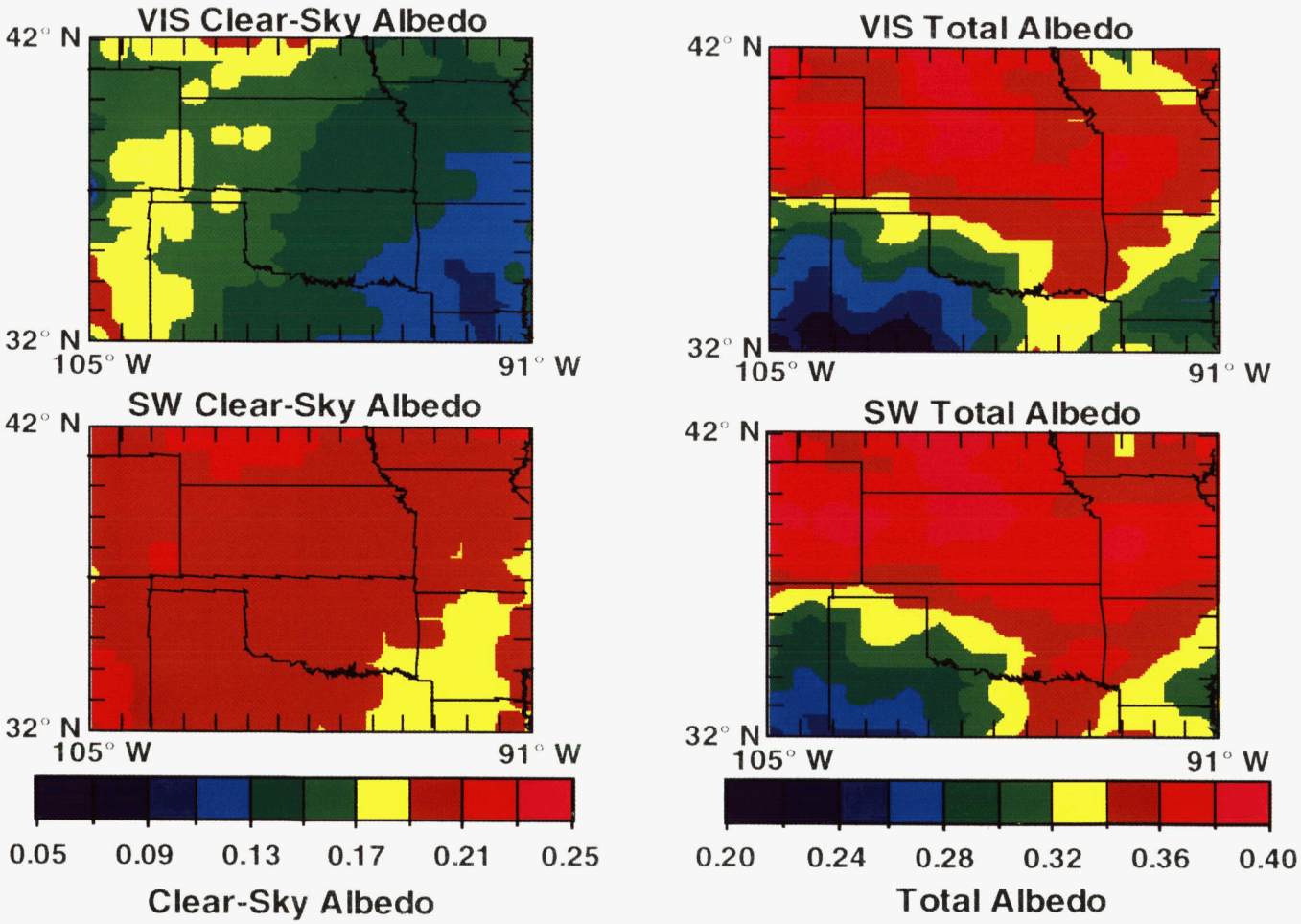

Figure 27. Mean VIS and SW albedos for 1330 and 2330 UTC for April 5 to May 1, 1994.

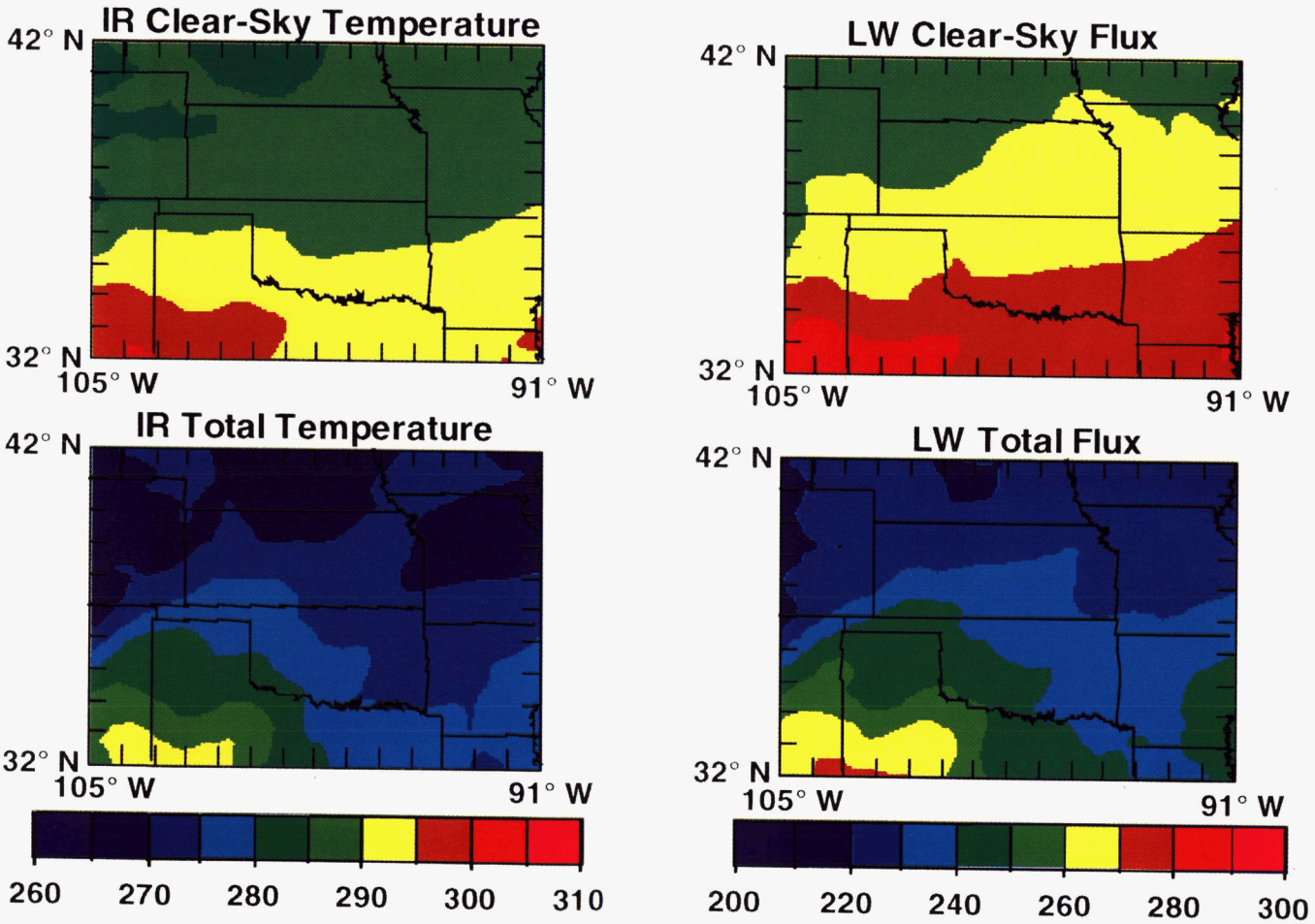

Figure 28. Mean IR temperatures and LW fluxes for 1330 to 2330 UTC for April 5 to May 1, 1994.

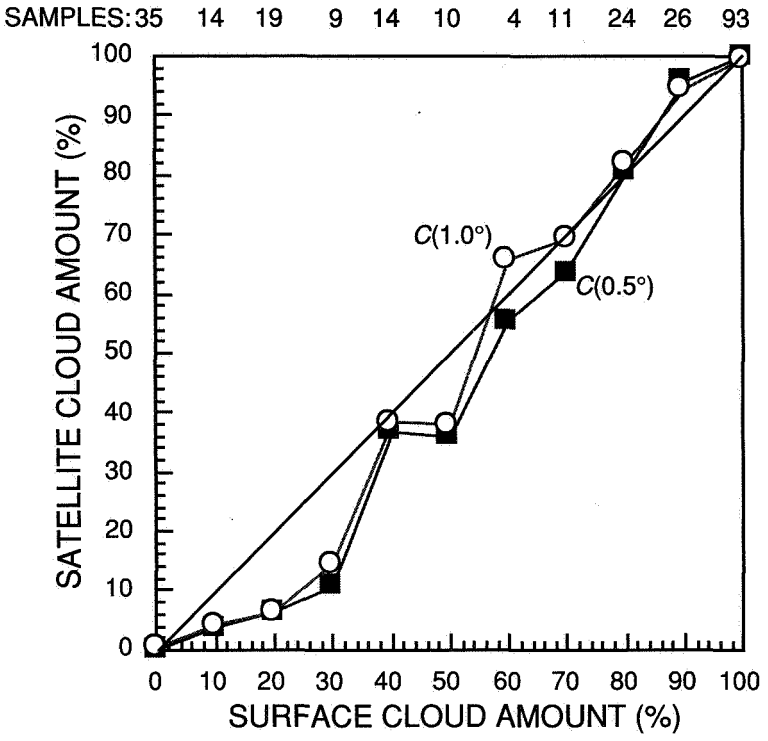

(a) 0.5° centered on WAFB at 38.75°N, 93.75°W; 1.0° centered on WAFB at 38.73°N, 93.55°W.

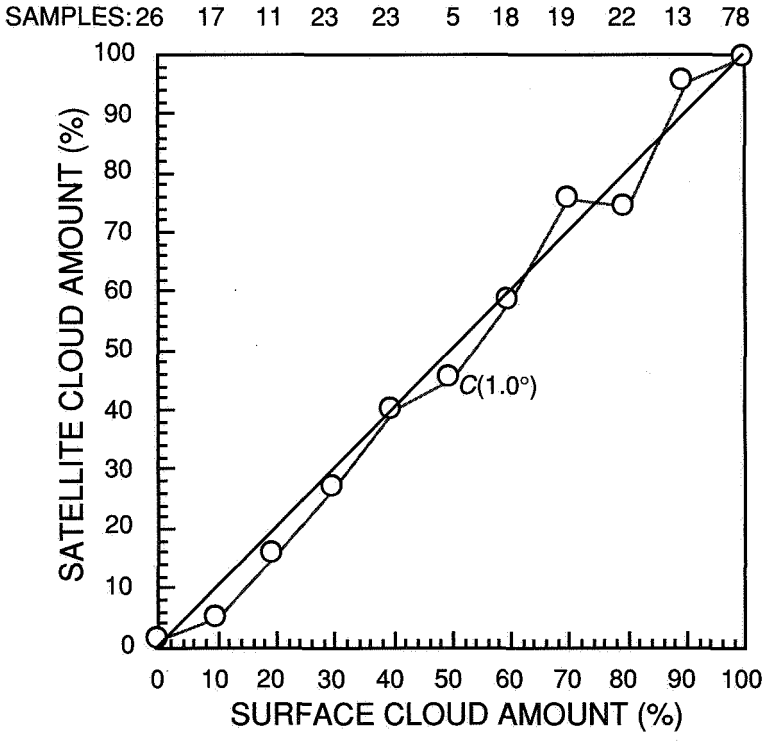

(b) 1.0° centered on TAFB at 35.42°N, 97.38°W.

Figure 29. Mean LBTM cloud amounts for each tenth of ground observed sky cover for April 5 to May 1, 1994; missing values filled by using linear interpolation for the satellite analysis regions.

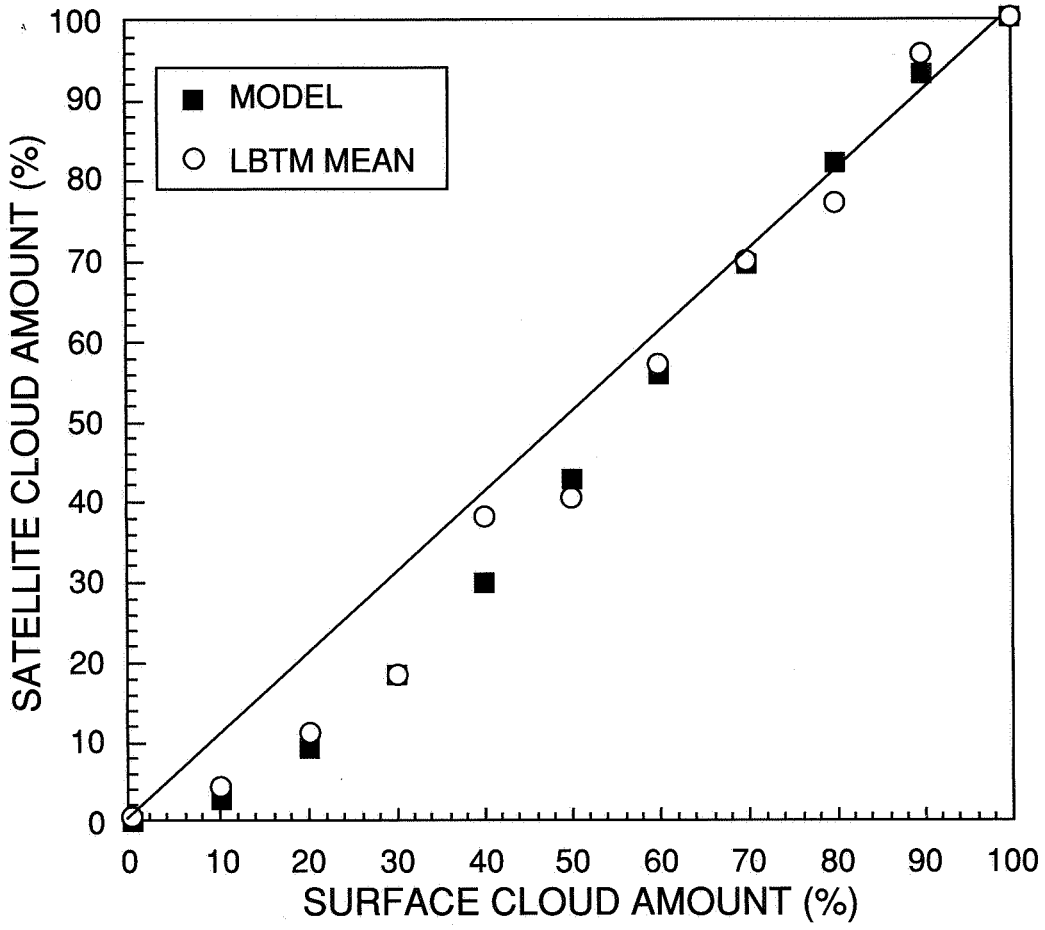

Figure 30. Mean satellite-observed cloudiness from WAFB and TAFB for each decile of surface-observed cloud fraction with an empirical model (eq. 24) based on whole-sky camera observations.

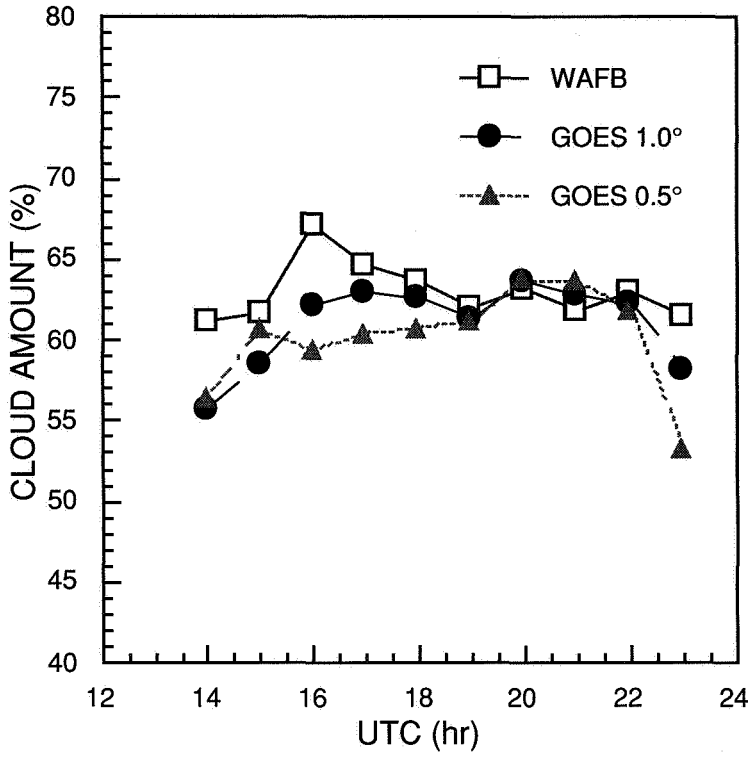

(a) 0.5° centered on WAFB at 38.75°N, 93.75°W; 1.0° centered on WAFB at 38.73°N, 93.55°W.

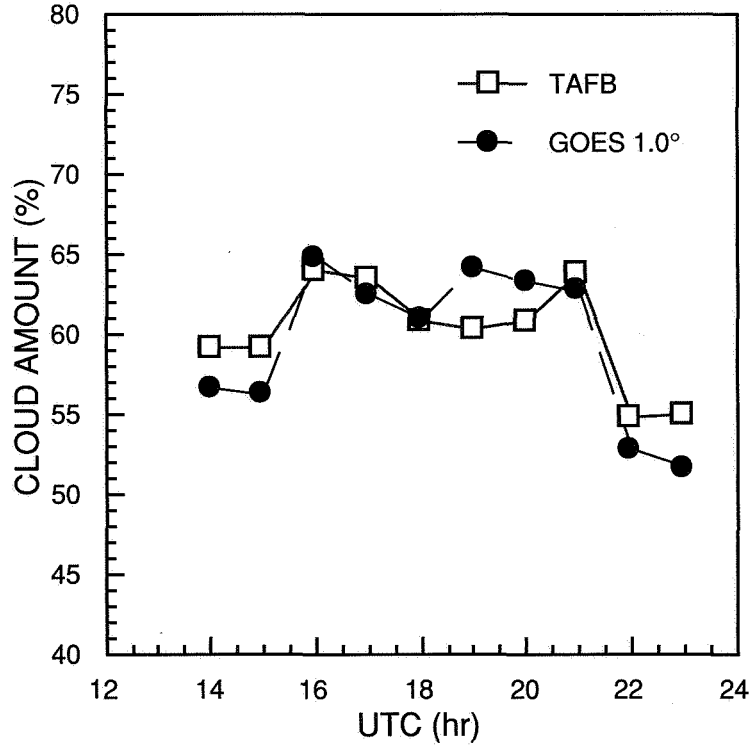

(b) 1.0° centered on TAFB at 35.42°N, 97.38°W.

Figure 31. Mean hourly matched cloud amounts from surface and from satellite for April 5 to May 1, 1994.

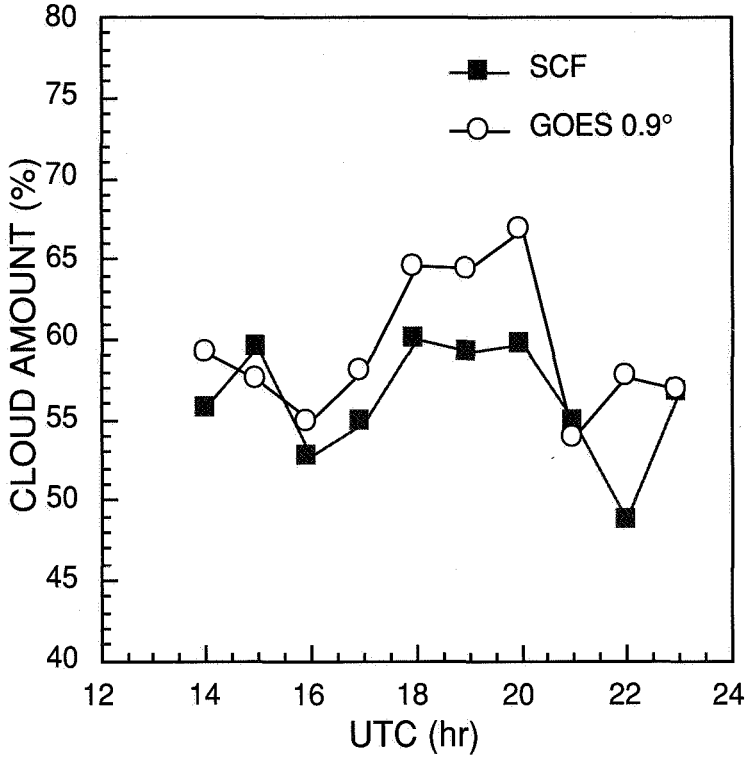

(a) ARM SGP Central Facility.

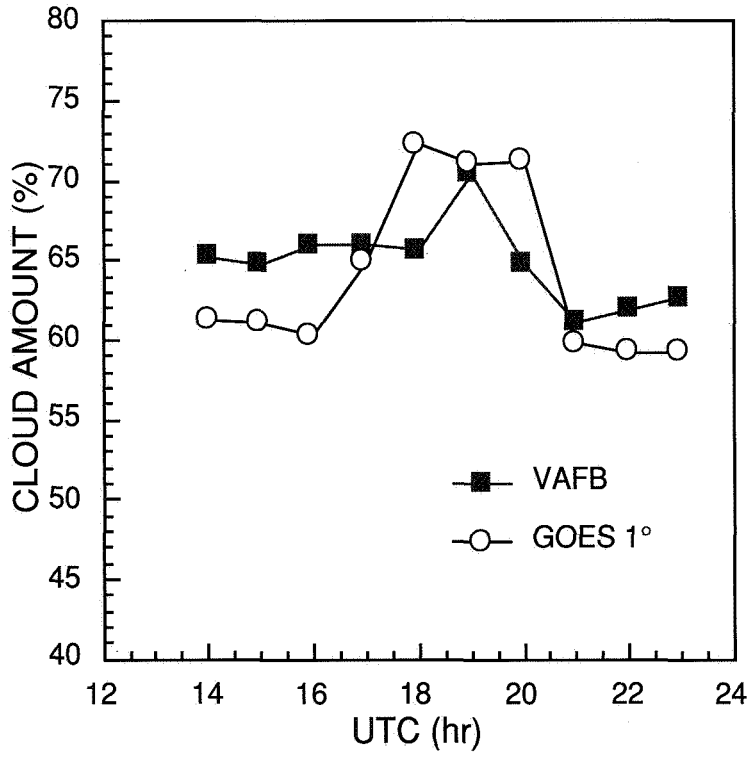

(b) Vance Air Force Base at 36.33°N, 97.92°W.

Figure 32. Mean hourly matched cloud amounts from surface and satellite for April 5 to May 1, 1994.

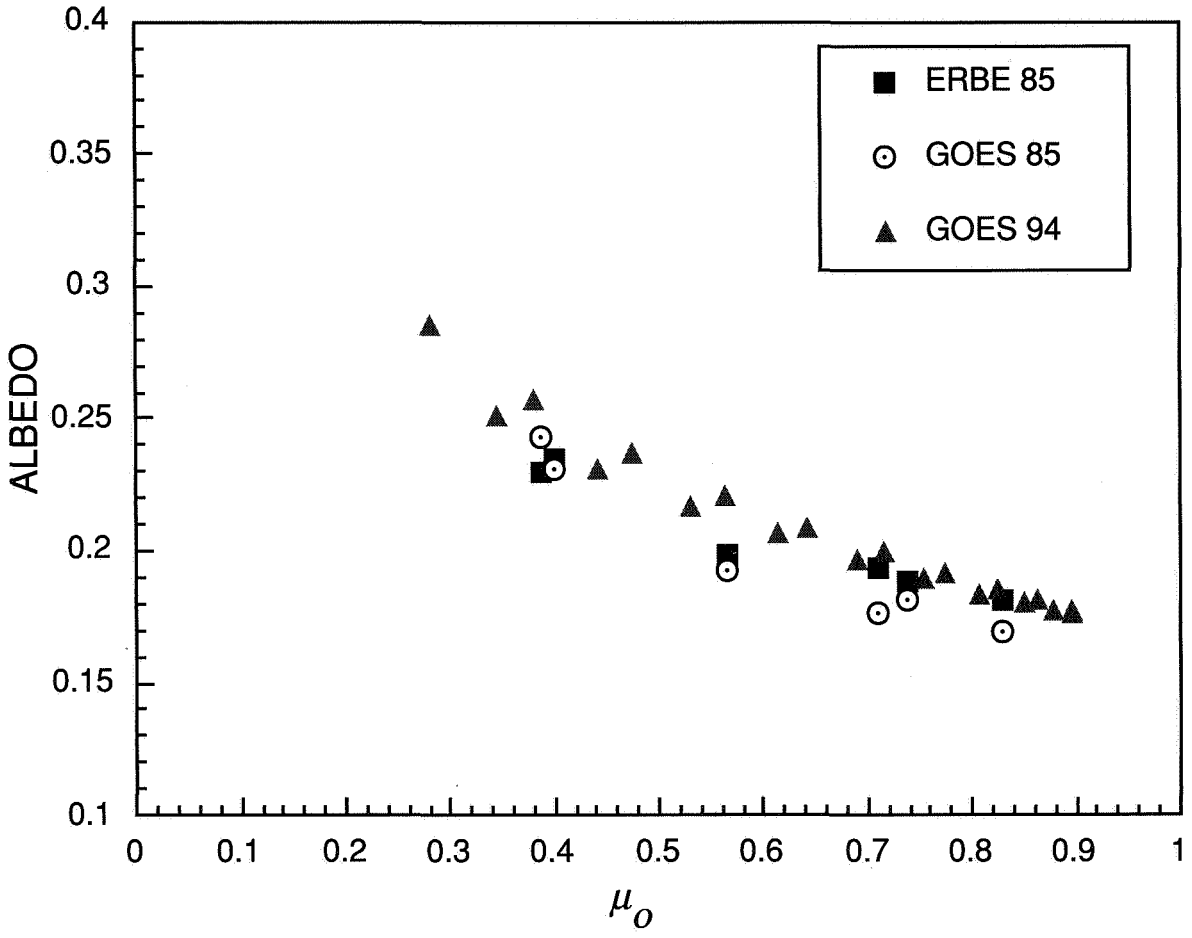

Figure 33. ERBS clear-sky SW albedos observed during April 1985 and mean April 1994, GOES-derived clear-sky SW albedos for area between 35.0°N and 37.5°N and between 95.0°W and 100.0°W.

REPORT DOCUMENTATION PAGE

Form Approved
OMB No. 0704-0188

1. AGENCY USE ONLY *(Leave blank)*	2. REPORT DATE	3. REPORT TYPE AND DATES COVERED
	August 1995	Reference Publication

4. TITLE AND SUBTITLE
Cloud Properties Derived From GOES-7 for Spring 1994 ARM Intensive Observing Period Using Version 1.0.0 of ARM Satellite Data Analysis Program

5. FUNDING NUMBERS
WU 146-90-04-49

6. AUTHOR(S)
Patrick Minnis, William L. Smith, Jr., Donald P. Garber, J. Kirk Ayers, and David R. Doelling

7. PERFORMING ORGANIZATION NAME(S) AND ADDRESS(ES)
NASA Langley Research Center
Hampton, VA 23681-0001

8. PERFORMING ORGANIZATION REPORT NUMBER
L-17491

9. SPONSORING/MONITORING AGENCY NAME(S) AND ADDRESS(ES)
National Aeronautics and Space Administration
Washington, DC 20546-0001

10. SPONSORING/MONITORING AGENCY REPORT NUMBER
NASA RP-1366

11. SUPPLEMENTARY NOTES
Minnis: Langley Research Center, Hampton, VA; Smith, Garber, Ayers, and Doelling: Lockheed Engineering & Sciences Company, Hampton, VA.
Research supported by Department of Energy ITF#214216AQ1.

12a. DISTRIBUTION/AVAILABILITY STATEMENT
Unclassified–Unlimited
Subject Category 47
Availability: NASA CASI (301) 621-0390

12b. DISTRIBUTION CODE

13. ABSTRACT *(Maximum 200 words)*
This document describes the initial formulation (Version 1.0.0) of the Atmospheric Radiation Measurement (ARM) program satellite data analysis procedures. Techniques are presented for calibrating geostationary satellite data with Sun synchronous satellite radiances and for converting narrowband radiances to top-of-the-atmosphere fluxes and albedos. A methodology is documented for combining geostationary visible and infrared radiances with surface-based temperature observations to derive cloud amount, optical depth, height, thickness, temperature, and albedo. The analysis is limited to two grids centered over the ARM Southern Great Plains central facility in north-central Oklahoma. Daytime data taken during April 5 to May 1, 1994, were analyzed on the 0.3° and 0.5° latitude-longitude grids that cover areas of 0.9° × 0.9° and 10° × 14°, respectively. Conditions ranging from scattered low cumulus to thin cirrus and thick cumulonimbus occurred during the study period. Detailed comparisons with hourly surface observations indicate that the mean cloudiness is within a few percent of the surface-derived sky cover. Formats of the results are also provided. The data can be accessed through the World Wide Web computer network.

14. SUBJECT TERMS
ARM program cloud properties; Earth Radiation Budget; Albedo

15. NUMBER OF PAGES
59

16. PRICE CODE
A04

17. SECURITY CLASSIFICATION OF REPORT	18. SECURITY CLASSIFICATION OF THIS PAGE	19. SECURITY CLASSIFICATION OF ABSTRACT	20. LIMITATION OF ABSTRACT
Unclassified	Unclassified	Unclassified	